

University of Southampton Research Repository ePrints Soton

Copyright © and Moral Rights for this thesis are retained by the author and/or other copyright owners. A copy can be downloaded for personal non-commercial research or study, without prior permission or charge. This thesis cannot be reproduced or quoted extensively from without first obtaining permission in writing from the copyright holder/s. The content must not be changed in any way or sold commercially in any format or medium without the formal permission of the copyright holders.

When referring to this work, full bibliographic details including the author, title, awarding institution and date of the thesis must be given e.g.

AUTHOR (year of submission) "Full thesis title", University of Southampton, name of the University School or Department, PhD Thesis, pagination

UNIVERSITY OF SOUTHAMPTON

**FACULTY OF ENGINEERING, SCIENCE,
AND MATHEMATICS**

School of Engineering Sciences

**Master-Mode Set of Turbulent 3D Channel
Flow**

By

MAKSYM BONDARENKO

Thesis for the degree of Doctor of Philosophy

April, 2008

Abstract

UNIVERSITY OF SOUTHAMPTON

FACULTY OF ENGINEERING, SCIENCE, AND MATHEMATICS

SCHOOL OF ENGINEERING SCIENCES

Doctor of Philosophy

MASTER-MODE SET OF TURBULENT 3D CHANNEL FLOW

by

Maksym Bondarenko

Turbulent flow fields can be expanded into a series in a set of basic functions. The terms of such series are often called modes. A master-mode-set is a subset of these modes, the time-history of which uniquely determines the time history of the entire turbulent flow provided that this flow is developed. In the present work the existence of the master-mode-set is demonstrated numerically for turbulent channel flow. The minimal size of a master-mode set and the rate of the process of the recovery of the entire flow from the master-mode set history are estimated. The velocity field corresponding to the minimal master-mode set is found to be a good approximation for mean velocity in the entire flow field. Mean characteristics involving velocity derivatives deviate in a very close vicinity to the wall, while master-mode two-point correlations exhibit unrealistic oscillations. This can be improved by using a larger than minimal master-mode set. The near-wall streaks are found to be contained in the velocity field corresponding to the minimal master-mode set, and the same is true at least for the large-scale part of the longitudinal vorticity structure. A database containing the time history of a master-mode set is demonstrated to be an efficient tool for investigating rare events in turbulent flows. In particu-

lar, a travelling-wave-like object was identified on the basis of the analysis of the database. Two master-mode-set databases of the time history of a turbulent channel flow are made available online at <http://www.dnsdata.afm.ses.soton.ac.uk/>. The services provided include the facility for the code uploaded by a user to be run on the server with an access to the data.

List of Contents

Abstract	iii
List of Contents	v
List of Figures	viii
List of Tables	xvii
Declaration of Authorship	xviii
Acknowledgements	xix
Nomenclature	xx
1 Introduction	1
1.1 Outline of the research	1
1.2 Genesis of the Problem	3
1.3 Overview of Relevant Literature	5
1.4 Outline of the thesis	16
2 Master Modes	18
2.1 Attractor	18
2.2 Determining modes.	19
2.3 Master modes	20
3 Direct Numerical Simulation of turbulent flow	22
3.1 Numerical model	22
3.2 Problem formulation	23
3.3 Spatial Derivatives	24

3.4	Implementation on Parallel Computers	26
3.5	Test calculations	28
4	Calculation of the master modes	39
4.1	Master-mode set of a numerical solution	39
4.2	Master code and slave code	41
4.3	Code verification.	41
4.3.1	Verification of the basic code.	41
4.3.2	Verification of the master-slave code	44
4.4	Mode ordering	47
5	Properties of master-mode set	50
5.1	Master-mode set size	50
5.1.1	Size of the master-mode set for $Re_\tau = 85$ and the dimension of the attractor	50
5.1.2	Size of the master-mode set for $Re_\tau = 360$	53
5.2	Convergence rate	55
5.3	Other properties of the master-mode set for $Re_\tau = 360$	58
5.3.1	Mean profiles	59
5.3.2	Two-point velocity correlations	64
5.3.3	Reynolds-stress budgets.	71
5.3.4	Visualization of the flow	78
6	Master-mode database	86
6.1	Finding a traveling wave in a DNS solution.	88
6.2	Results	90
6.3	Summary	95
7	Conclusion.	96
8	Suggestions for future work	98

A The DNS Database Web Server and Master-Mode Database User Manual	100
Bibliography	110

List of Figures

1.1	Evolution of $\ u_1 - u_2\ $ with different λ for continuous data assimilation on N Fourier modes, obtained by Olson & Titi [1].	10
1.2	Two-dimensional Navier-Stokes solutions obtained by Henshaw, Kreiss & Ystrom [2]: the relative errors in the high modes for the play-back solutions as a function of time and a function of the cut-off wave number k_c	13
1.3	Two-dimensional Navier-Stokes solutions obtained by Henshaw, Kreiss & Ystrom [2]: contours of the vorticity at the starting time for the play-back computation. Left: play-back solution, right: reference solution. The initial conditions for the play-back solution were set equal to the lowest $k_c = 16$ modes of the reference solution at $t = 50$	14
1.4	Two-dimensional Navier-Stokes solutions obtained by Henshaw, Kreiss & Ystrom [2]: solutions at time $t = 200$. Left: play-back solution, right: reference solution.	14
1.5	Evolution of $\Delta(t)$, the energy of the difference field $\mathbf{u}^{(2)} - \mathbf{u}^{(1)}$, for various k_a , obtained by Yoshida, Yamaguchi & Kaneda [3]. η is the Kolmogorov length scale.	16
3.1	Sketch of the fluid flow domain.	23
3.2	Decomposition of the domain.	27
3.3	Mean velocity profile in global coordinates. Present (triangles), Hu & Sandham (solid line) for $Re_\tau = 360$ and present (circles), MKM (diamonds) for $Re_\tau = 395$	29

3.4	Mean velocity profile in wall coordinates. Present (triangles), Hu & Sandham (solid line) for $Re_\tau = 360$ and present (circles), KMM (diamonds) for $Re_\tau = 395$; $u^+ = 2.5 \log z^+ + 5.5$ (long dash); $u^+ = z^+$ (dash dot).	29
3.5	a) Two-point velocity correlation R_{uu} (circle), R_{vv} (triangles) and R_{ww} (gradient) at $z^+ = 10$, $Re_\tau = 360$. The solid lines represent the values of R_{uu} , R_{vv} , R_{ww} from HS; b) Two-point velocity correlation R_{uu} (circle), R_{vv} (triangles) and R_{ww} (gradient) at $z^+ = 10$, $Re_\tau = 395$. The solid lines represent the values of R_{uu} , R_{vv} , R_{ww} from MKM; . . .	32
3.6	a) Two-point velocity correlation R_{uu} (circles), R_{vv} (triangles) and R_{ww} (gradients) at $z^+ = 10$, $Re_\tau = 360$. The solid lines represent the values of R_{uu} , R_{vv} , R_{ww} from HS; b) Two-point velocity correlation R_{uu} (circles), R_{vv} (triangles) and R_{ww} (gradients) at $z^+ = 10$, $Re_\tau = 395$. The solid lines represent the values of R_{uu} , R_{vv} , R_{ww} from MKM;	33
3.7	Terms in the budgets of turbulent kinetic energy, P (solid line), T (dashed line), D (dash-dotted line), Π (dotted line), ε (long dash-line), Σ (dash-dotted-dotted line). The line with a circles represent the values of the budgets of TKE from HS, $Re_\tau = 360$	34
3.8	Terms in the budgets of turbulent kinetic energy, P (solid line), T (dashed line), D (dash-dotted line), Π (dotted line), ε (long dash-line), Σ (dash-dotted-dotted line). The line with a circles represent the values of the budgets of TKE from MKM, $Re_\tau = 395$	34
3.9	Turbulent intensity u_{rms} (solid line), v_{rms} (dashed line) and w_{rms} (dash-dotted line); $Re_\tau = 360$. The line with a circles, deltas and diamonds represent the values of u_{rms} , v_{rms} and w_{rms} from HS $Re_\tau = 360$	35

3.10	Turbulent intensity u_{rms} (solid line), v_{rms} (dashed line) and w_{rms} (dash-dotted line); $Re_\tau = 395$. The line with a circles, deltas and diamonds represent the values of u_{rms} , v_{rms} and w_{rms} from MKM $Re_\tau = 395$	35
3.11	Reynolds stress distributions across the channel: Present (solid line), HS (delta) for $Re_\tau = 360$ and present (circle), MKM (diamond) for $Re_\tau = 395$	36
3.12	Energy spectra $E(k_x)$ integrated over wall-normal direction, $Re_\tau = 360$	36
3.13	Energy spectra $E(k_y)$ integrated over wall-normal direction, $Re_\tau = 360$	37
3.14	Contours of vorticity ω_x	37
3.15	Contour of streamwise velocity in wall parallel plane for a wall distance of $z^+ = 5.6$ from the top of the channel. Low-speed streaks (black).	38
3.16	Contour of streamwise velocity in wall parallel plane for a wall distance of $z^+ = 5.6$ from the bottom of the channel. Low-speed streaks (black).	38
4.1	The mean flow $U(z)$	43
4.2	Comparison of u and w -velocity error between the analytical and numerical solutions	44
4.3	Comparison of v -velocity errors for grid size $16 \times 16 \times 16$ (dashed line) and $32 \times 32 \times 32$ (solid line).	44
4.4	Streamwise velocity component u_A (solid line) and $u_{A-master}$ (circles) at a point on the central plane of the channel.	45
4.5	Streamwise velocity component u_B (solid line) and $u_{B-master}$ (circles) at a point on the central plane of the channel.	45
4.6	The evolution of $\ u_{mc} - u_{sc}\ _{L_2}$, the modes were ordered by the sum of their wave-numbers, $Re_\tau = 180$	48

4.7	The evolution of $\ u_{mc} - u_{sc}\ _{L_2}$, the modes were ordered by the energy-based method, $Re_\tau = 180$	49
4.8	The evolution of $\ u_{mc} - u_{sc}\ _{L_2}$, the modes were ordered by the enstrophy-based method, $Re_\tau = 180$	49
5.1	Mean velocity profile in wall coordinates $Re_\tau = 85$ (dashed line), $u^+ = z^+$ (dash-dotted line) and $u^+ = 2.5 \log y^+ + 5.5$ (solid line) . . .	51
5.2	Turbulent intensity u_{rms} (solid line), v_{rms} (dashed line) and w_{rms} (dash-dotted line); $Re_\tau = 85$	51
5.3	The evolution of $\ u_{mc} - u_{sc}\ _{L_2}$, $Re_\tau = 85$	52
5.4	The evolution of $\ u_{mc} - u_{sc}\ _{L_2}$, energy-based method of ordering the modes, $Re_\tau = 360$	54
5.5	The evolution of $\ u_{mc} - u_{sc}\ _{L_2}$, enstrophy-based method of ordering the modes, $Re_\tau = 360$	55
5.6	Convergence rate, $L_z = 2$: $Re_\tau = 85$, $L_x \times L_y = 5 \times 5$, \circ ; $Re_\tau = 180$, $L_x \times L_y = 4 \times 3$, \square ; $Re_\tau = 360$, $L_x \times L_y = 6 \times 3$, \triangle ; $Re_\tau = 360$, $L_x \times L_y = 14 \times 9$, \diamond	56
5.7	The dash-dotted line is an approximation of the Yoshida <i>et al.</i> [3] results. Other lines and symbols are the same as in figure 5.6	58
5.8	Mean velocity profile in wall coordinates, $Re_\tau = 360$, $L_x \times L_y \times L_z = 6 \times 3 \times 2$, $N_x = 128$, $N_y = 128$ and $N_z = 160$, full flow (solid curve); minimal master-mode set ($N_{mm}=29716$) ordered by $\langle \hat{\mathbf{u}} \rangle \triangle$; a minimal master-mode set ($N_{mm}=42537$) ordered by $\langle \hat{\Omega} \rangle \circ$	59

- 5.9 Mean square fluctuation velocity: a) Comparison of turbulent intensity between full flow and flow calculated from the master-mode set, full flow (solid curve), a minimal master-mode set ($N_{mm}=29716$) ordered by $\langle |\hat{\mathbf{u}}| \rangle$ (dotted line) and ($N_{mm}=42537$) $\langle |\hat{\Omega}| \rangle$ (dashed line); b) calculated from slave modes only ordered by $\langle |\hat{\mathbf{u}}| \rangle$ u_{rms} (solid line), v_{rms} (dashed line) and w_{rms} (dash-dotted line), by $\langle |\hat{\Omega}| \rangle$ u_{rms} (solid line with circles), v_{rms} (dashed line with circles) and w_{rms} (dash-dotted line with circles), computational box size is $6 \times 2 \times 3$, $Re_\tau = 360$. 60
- 5.10 (a) turbulent kinetic energy: full flow (solid line), a minimal master-mode set ($N_{mm}=42537$) ordered by $\langle |\hat{\Omega}| \rangle$ (dashed line) and a minimal master-mode set ($N_{mm}=29716$) ordered by $\langle |\hat{\mathbf{u}}| \rangle$ (dash-dotted line). (b) Stress distributions across the channel, full flow (dash-dotted), $\langle |\hat{\Omega}| \rangle \Delta$, $\langle |\hat{\mathbf{u}}| \rangle \circ$, computational box size is $6 \times 2 \times 3$, $Re_\tau = 360$ 62
- 5.11 The derivatives of wall normal velocity: (a) full flow (solid line), $\langle |\hat{\mathbf{u}}| \rangle$ (circle) and $\langle |\hat{\Omega}| \rangle$ (delta). (b) full flow (solid line), $\langle |\hat{\mathbf{u}}| \rangle$ (dash-dotted line) and $\langle |\hat{\Omega}| \rangle$ (dashed line). Computational box size is $6 \times 2 \times 3$, $Re_\tau = 360$, $N_{mm} = 42537$ for $\langle |\hat{\Omega}| \rangle$ and $N_{mm} = 29716$ for $\langle |\hat{\mathbf{u}}| \rangle$. 63
- 5.12 Streamwise energy spectrum. Full flow, the curve; master-mode-set, dashed line, for $Re_\tau = 360$, $z^+ = 5.6$, $L_x \times L_y = 6 \times 3$, and the minimal master-mode set ($N_{mm} = 29716$). 65
- 5.13 Two-point velocity cross-correlations between master-mode set and slave-mode set, R_{uu} (solid line), R_{vv} (dashed line) and R_{ww} (dash-dotted line), at $z^+ = 1.7$. a) streamwise direction $\langle |\hat{\mathbf{u}}| \rangle$, c) streamwise direction $\langle |\hat{\Omega}| \rangle$, b) spanwise direction $\langle |\hat{\mathbf{u}}| \rangle$ and d) spanwise direction $\langle |\hat{\Omega}| \rangle$. $N_{mm} = 42537$ for $\langle |\hat{\Omega}| \rangle$ and $N_{mm} = 29716$ for $\langle |\hat{\mathbf{u}}| \rangle$ 67

- 5.14 Two-point velocity correlations, R_{uu} (solid line), R_{vv} (dashed line) and R_{ww} (dash-dotted line), at $z^+ = 5.6$. Full flow (a) streamwise direction, (b) spanwise direction; Two-point velocity auto-correlations of the master-mode set (c) $\langle |\hat{\mathbf{u}}| \rangle$ streamwise direction, (d) $\langle |\hat{\mathbf{u}}| \rangle$ spanwise direction, (e) $\langle |\hat{\Omega}| \rangle$ streamwise direction, (f) $\langle |\hat{\Omega}| \rangle$ spanwise direction. $N_{mm} = 42537$ for $\langle |\hat{\Omega}| \rangle$ and $N_{mm} = 29716$ for $\langle |\hat{\mathbf{u}}| \rangle$. 68
- 5.15 Two-point velocity cross-correlations between master-mode set and slave-mode set, R_{uu} (solid line), R_{vv} (dashed line) and R_{ww} (dash-dotted line), at $z^+ = 5.6$: (a) $\langle |\hat{\mathbf{u}}| \rangle$ streamwise direction, (b) $\langle |\hat{\mathbf{u}}| \rangle$ spanwise direction, (c) $\langle |\hat{\Omega}| \rangle$ streamwise direction and (d) $\langle |\hat{\Omega}| \rangle$ spanwise direction. $N_{mm} = 42537$ for $\langle |\hat{\Omega}| \rangle$ and $N_{mm} = 29716$ for $\langle |\hat{\mathbf{u}}| \rangle$. . . 69
- 5.16 Two-point velocity auto-correlations of the slave-mode set, R_{uu} (solid line), R_{vv} (dashed line) and R_{ww} (dash-dotted line), at $z^+ = 5.6$: (a) $\langle |\hat{\mathbf{u}}| \rangle$ streamwise direction, (b) $\langle |\hat{\mathbf{u}}| \rangle$ spanwise direction, (c) $\langle |\hat{\Omega}| \rangle$ streamwise direction and (d) $\langle |\hat{\Omega}| \rangle$ spanwise direction. $N_{mm} = 42537$ for $\langle |\hat{\Omega}| \rangle$ and $N_{mm} = 29716$ for $\langle |\hat{\mathbf{u}}| \rangle$ 70
- 5.17 Two-point velocity auto-correlations of the master-mode sets ordered by $\langle |\hat{\mathbf{u}}| \rangle$ R_{uu} (solid line), R_{vv} (dashed line) and R_{ww} (dash-dotted line) at $z^+ = 5.6$, $N_{mm} = 41069$: (a) streamwise direction, (b) spanwise direction. 71
- 5.18 Terms in the budget of the turbulence kinetic energy for full flow and master-mode set. Curves with square symbols represent the turbulence kinetic energy calculated from master-mode set only ordered by $\langle |\hat{\mathbf{u}}| \rangle$ and with circle symbols calculated from master-mode set only ordered by $\langle |\hat{\Omega}| \rangle$ 72

- 5.19 Terms in the budgets of turbulent kinetic energy: (a) full flow, (b) master-mode set only ordered by $\langle |\hat{\mathbf{u}}| \rangle$ and (c) master-mode set only ordered by $\langle |\hat{\Omega}| \rangle$. P (solid line), T (dashed line), D (dash-dotted line), Π (dotted line), ε (long dash-line), Σ (dash-dotted-dotted line). Right-hand figures show the same data with logarithmic region. 73
- 5.20 $\overline{u'u'}$: (a) full flow, (b) master-mode set only ordered by $\langle |\hat{\mathbf{u}}| \rangle$ and (c) master-mode set only ordered by $\langle |\hat{\Omega}| \rangle$. P (solid line), T (dashed line), D (dash-dotted line), Π (dotted line), ε (long dash-line), Σ (dash-dotted-dotted line). Right hand figures show the same data with logarithmic region. 74
- 5.21 $\overline{u'w'}$: (a) full flow, (b) master-mode set only ordered by $\langle |\hat{\mathbf{u}}| \rangle$ and (c) master-mode set only ordered by $\langle |\hat{\Omega}| \rangle$. P (solid line), T (dashed line), D (dash-dotted line), Π (dotted line), ε (long dash-line), Σ (dash-dotted-dotted line). Right hand figures show the same data with logarithmic region. 75
- 5.22 $\overline{v'v'}$: (a) full flow, (b) master-mode set only ordered by $\langle |\hat{\mathbf{u}}| \rangle$ and (c) master-mode set only ordered by $\langle |\hat{\Omega}| \rangle$. P (solid line), T (dashed line), D (dash-dotted line), Π (dotted line), ε (long dash-line), Σ (dash-dotted-dotted line). Right hand figures show the same data with logarithmic region. 76
- 5.23 $\overline{w'w'}$: (a) full flow, (b) master-mode set only ordered by $\langle |\hat{\mathbf{u}}| \rangle$ and (c) master-mode set only ordered by $\langle |\hat{\Omega}| \rangle$. P (solid line), T (dashed line), D (dash-dotted line), Π (dotted line), ε (long dash-line), Σ (dash-dotted-dotted line). Right hand figures show the same data with logarithmic region. 77
- 5.24 Contours of streamwise velocity fluctuation in $x - z$ plane. a) full flow; b) master modes $N_{mm} = 29716$ c) slave modes. $Re_\tau = 360$. . . 79

5.25	Contours of streamwise vorticity in $x - z$ plane: a) full flow; b) master-mode set, $N_{mm} = 29716$; c) slave-mode set. $Re_\tau = 360$	81
5.26	Contours of streaks in near-wall turbulence flow at $z^+ = 5.6$ in $x - y$ plane: a) full flow; b) master-mode set, $N_{mm} = 29716$; c) slave-mode set. $Re_\tau = 360$	82
5.27	Iso-surface of vorticity in the x-direction: a) full flow; b) master-mode set, $N_{mm} = 29716$; c) slave-mode set, $Re_\tau = 360$	83
5.28	Contours of vorticity: a) for full flow; b) the flow calculated from master-mode set only, $N_{mm} = 29716$. $Re_\tau = 360$, $t = 0$	84
5.29	Contours of vorticity: a) for full flow; b) the flow calculated from master-mode set only, $N_{mm} = 29716$. $Re_\tau = 360$, $t = 0.0025$	84
5.30	Contours of vorticity: a) for full flow; b) the flow calculated from master-mode set only, $N_{mm} = 29716$. $Re_\tau = 360$, $t = 0.01$	85
6.1	Spanwise ($\Delta x = 0$) two-point correlations: curves, full flow as calculated by Hu <i>et al.</i> [4], $L_x \times L_y = 12 \times 6$; symbols, master-mode-set database with $N_{mm} = 2170044$ and $L_x \times L_y = 14 \times 9$; longitudinal velocity correlation, R_{uu} , ■; spanwise velocity correlation, R_{vv} , ▲; wall-normal velocity correlation, R_{ww} , ●. For $Re_\tau = 360$ and $z^+ = 10$	87
6.2	Snapshot of travelling waves at $t = 600$ obtained by Itano & Toh [5]. (a) longitudinal vorticity $\omega_x(y, z)$ at $z^+ = 398$; (b) $u_x(x, z)$ at $y^+ = 71$. Shade indicates $u_x < 0.65$ or $\omega_x < -0.05$. Arrows indicate the positions of the section. Thick solid lines are for $u_x = 0.4$ and 0.6.	89
6.3	Decomposition of the domain.	90
6.4	Time-evolution of C_V (a) , f_V (b) for case A1.	92
6.5	Snapshot of TW at a) $t=13.625$, b)=13.7, c) $t=13.75$, d) $t=13.825$, e) $t=13.875$, f) $t=13.95$; Case A1, longitudinal velocity fluctuation in the plane $z^+ = 6.9$ is visualised.	93

6.6	Snapshot of TWS and iso-surface of vorticity in the x-direction. . .	94
A.1	DNS Database Web Server.	101
A.2	Registration form.	105
A.3	Navigating the site.	106
A.4	DNS Database Web Server.	107
A.5	DNS Database Web Server.	108
A.6	Example.	109

List of Tables

3.1	Simulation parameters for the two channel direct numerical simulations.	28
6.1	Run parametters.	91

Declaration of Authorship

I, **Bondarenko Maksym**, declare that the thesis entitled

Master-mode set of turbulent 3D channel flow

and the work presented in it are my own. I confirm that

- this work was done wholly or mainly while in candidature for a research degree at this University;
- where any part of this thesis has previously been submitted for a degree or any other qualification at this University or any other institution, this has been clearly stated;
- where I have consulted the published work of others, this is always clearly attributed;
- where I have quoted from the work of others, the source is always given. With the exception of such quotations, this thesis is entirely my own work;
- I have acknowledged all main sources of help;
- where the thesis is based on work done by myself jointly with others, I have made clear exactly what was done by others and what I have contributed myself;
- none of this work has been published before submission. or [delete as appropriate] parts of this work have been published as: [please list references]

Signed:

Date:

Acknowledgements

This work has benefited from collaboration with and consultation of a number of helpful people. Primary thanks go to Prof. Sergei Chernyshenko for bringing me over, keeping me moving forward, and being flexible, supportive, and a friend. Additional thanks to Dr. Gary Coleman, Dr. Fedorov , Dr. R. D. Sandberg.

I am deeply indebted to my parents, Bondarenko Evgeny and Olga Vladimirovna for their infinite patience, support and love throughout all the years of work. I could not, and would not have, done it without them. I would also like to acknowledge my brother, Anatoli, for his humor and love, and his own achievements have been a source of inspiration to me.

I'd like to thank my colleague, and friend, Mr. Molodchenko from University of Greenwich.

Personal thanks go to colleagues Dr. C.P. Yorke, Dr. M. Baig, Mr. P. Archer, Mr. A. Bouferrouk, and others in 13/5073 for knowledge, humour, and compassion.

Nomenclature

Symbol	Description
c	wave speed
D_λ	fractal dimension
$E(k)$	Energy spectrum as function of wavenumber
Gr	Grashof number
i	Imaginary number, $i = \sqrt{-1}$
K	turbulent kinetic energy
k_x, k_y, k_z	wavenumbers
N_{mm}	minimal number of modes
p	kinematic pressure
q	$p + uu/2$, modified pressure
t	time
T	Chebyshev polynomial
Re	Reynolds number
Re_τ	$u_\tau^* h^* / \nu$, Wall-friction Reynolds number
Re_λ	Taylor microscale Reynolds number
R_{ij}	Two-point autocorrelation
$\bar{u}, \bar{v}, \bar{w}$	mean velocity components
u', v', w'	components of fluctuation velocity
\mathbf{u}	non-dimensional velocity vector

$\hat{\mathbf{u}}$ complex-valued amplitudes of the modes

x^+ xu_τ/ν

z^+ Wall-normal location in inner coordinates

Greek Symbols

Symbol	Description
ω	non-dimensional vorticity vector
τ	$\langle v'w' \rangle$, Reynolds shear stress
u_τ^*	$\sqrt{\tau_w^*/\rho^*}$ dimensional wall-friction velocity
τ_w^*	wall shear stress
ρ^*	dimensional density
ν	kinematic viscosity
η	Kolmogorov length scale
λ	Taylor microscale

Abbreviations

Symbol	Description
CPU	Computer processing unit
DNS	Direct numerical simulation
MPI	Message passing interace
r.m.s	Root mean square
GB	Giga-byte
FFT	Fast Fourier transform

Symbol	Description
TW	Travelling wave
TWS	Travelling wave solution
Tb	Tera-byte

Symbols

Symbol	Description
∇	Gradient operator
$\nabla \cdot$	Divergence operator
∇^2	Laplacian operator
\times	Vector cross product
Δt	Time step
$\langle \hat{\mathbf{u}} \rangle$	$\langle \hat{\mathbf{u}}_{k_x, k_y, k_z} ^2 \rangle$, method of ordering the modes
$\langle \hat{\Omega} \rangle$	$\langle \hat{\omega}_{k_x, k_y, k_z} ^2 \rangle$, method of ordering the modes

1 Introduction

This chapter explains the motivation for the work, the core objectives of this study and gives a detailed summary of related literature.

1.1 Outline of the research

It has long been understood that the actual number of degrees of freedom of a turbulent flow should be significantly less than that required for resolving turbulent flow in a numerical simulation. The present study explores this idea, clarifies and exploits it. Greater clarity on this issue can, in particular, be exploited in the area of creating databases of turbulent flows for fundamental research purposes. The main tool of the present investigation is the set of so-called master-modes, which contain, in a certain precisely defined sense, the full information about a developed turbulent flow.

The most important aim of our study was to verify the existence of master-mode sets in wall-bounded 3D turbulence flows. Achieving this aim with a rigorous analytic approach is quite difficult, and an addition of simplifying assumptions would make the study inconclusive. For this reason the main approach of the present research involved solving numerically the Navier-Stokes equations. The Direct Numerical Simulation (DNS) code for incompressible turbulent channel geometry [6] available within the AFM research group was modified to suit our purpose.

The number of master modes in a 3D turbulent flow in a channel was estimated at several values of the Reynolds number and compared with the dimension of the Navier-Stokes attractor in one case ($Re_\tau = 80$) for which the attractor dimension has previously been calculated (see [7]).

Once a master-mode set is found, the natural goal is to explore its properties: Reynolds stress budgets, two point correlations and to compare them with the full

flow parameters. Then the master-mode set was used to explore the existence of a hierarchy of organized structures. The aim was to determine which structures, if any, are primary and which are secondary. Finally a database containing the time history of the amplitude of master modes of a channel flow was created and the advantages of having such a database were demonstrated on a problem of searching for traveling waves in turbulent flow.

The research described in this thesis gave the following results:

1. It was shown by numerical experiment that a master mode sets exist in 3D turbulent flows.
2. For turbulent channel flow in a box $L_x \times L_y \times L_z = 6 \times 3 \times 2$ at $Re_\tau = 360$ the minimal size of the master-mode set is about 29716. For box size $L_x \times L_y \times L_z = 14 \times 9 \times 2$ at $Re_\tau = 360$ the size of the master-mode set is about 225900.
3. For channel flow the rate of convergence at which the L_2 norm of the difference between the master solution and the slave solution tends to zero can be estimated as $30(N/V)^{2/3}/Re_\tau$ for large N , where N is the master-mode set size (that is half of the number of independent real-valued parameters needed to identify all the mode amplitudes in the master-mode set), V is the volume of the computational domain, and Re_τ is the Reynolds number based on the friction velocity and the channel half-width.
4. The velocity field corresponding to the minimal master-mode set is a good approximation for mean velocity and some other mean characteristics. However, the minimal master-mode set based on Chebyshev polynomials in the wall-normal direction produces large deviations of turbulence kinetic energy budget components from their exact values in the close vicinity of the wall where Chebyshev polynomials over-resolve the flow. Also, there are significant deviations for some of the two-point correlations. Therefore, it is reasonable to store in a database a master-mode set of a somewhat greater size

than minimal.

5. When the flow field is represented as a sum of a master-mode set and the rest of the modes, the near-wall streaks turn out to be contained in the master-mode part. The results for the distribution of the longitudinal vorticity are less certain, with some small-scale structures sometimes observed in the rest of the modes.
6. Two databases containing the time history of a master-mode set, for $Re_\tau = 360$, box size $L_x \times L_y \times L_z = 6 \times 3 \times 2$, time length $T = 40$ and for $Re_\tau = 360$, box size $L_x \times L_y \times L_z = 14 \times 9 \times 2$, time length $T = 15$ were created. For the second case 2200000 master-modes were stored for faster convergence.
7. A database containing the time history of a master-mode set is found to be an efficient tool for investigating rare events. In particular, a travelling-wave-like object was identified on the basis of the analysis of the database.
8. Two master-mode-set databases of the time history of a turbulent channel flow are available online at <http://www.dnsdata.afm.ses.soton.ac.uk/>. The code uploaded by a user can be run on the server with an access to the data.

1.2 Genesis of the Problem

Using computers and numerical techniques to simulate turbulent fluid flow is a non-trivial problem. One major challenge is that in order to resolve all the significant eddies in turbulent flows a very fine grid is needed. Let L be a typical macroscopic length scale for the flow, for example the size of a body in the simulation, l be a microscopic length scale and U be a typical flow velocity. If ν is the kinematic viscosity of the fluid, the Reynolds number, Re is defined as

$$Re = \frac{UL}{\nu}.$$

This non-dimensional number characterizes the flow in simple geometries. Its value allows some rough conclusions to be drawn about the flow characteristics, such as whether the flow is laminar or turbulent.

In [8] a rough estimate for the number of grid points required to resolve the smallest eddies of dynamical significance is given. In each spatial direction, we need roughly $N \sim Re^{3/4}$ grid points. This estimate is based on the Kolmogorov scale, the ratio between the largest and smallest length, $L/l \sim Re^{3/4}$.

This means that in three dimensions we need approximately $N^3 \approx Re^{9/4}$ grid points. The Reynolds number for an airplane with a wing chord of 5m, flying at sea level at 100m/s is $Re \approx 3.3 \times 10^7$, which implies $N^3 \approx 8.25 \times 10^{16}$. Direct Numerical Simulation (DNS) of such a flow is simply impossible with today's computers. Even for moderate Reynolds numbers and simple geometries the computational effort required for DNS is very high. For example, in [9] the DNS of a plane channel flow for $Re_\tau = 2003$ (Re_τ is the Reynolds number based on friction velocity) required about 6×10^6 processor-hours. The analysis of the solution can be performed simultaneously with the calculation, but if a new analysis is needed the calculation may need to be repeated. Very few research groups have access to computational resources of that scale but even for them repeating a major DNS calculation is not always possible. It is natural, therefore, to store the data for future analysis, and indeed, turbulent flow DNS databases are becoming more common. Using turbulent flow databases gives a considerable advantage, as the data can be quickly accessed at a moderate cost. However, a database of the full time history of a turbulent flow produced by a major DNS calculation would be very large. For example, the above-mentioned DNS gave about 25TB of raw data. Opening access (say, via Internet) to such a large volume is not yet feasible. For this reason the existing open-access DNS databases contain only a limited number of samples of the instantaneous flow field complemented with various averaged data. Because of this the majority of researchers working on turbulence have only a limited access to DNS results.

DNS calculations are usually performed for flows in bounded domains (say, a pipe flow periodic in the axial direction). In this case as time advances the state of the flow approaches a finite-dimensional attractor. While the dimension of this attractor is believed to be high for high Reynolds numbers, it can be expected to be much smaller than the number of modes required for a fully resolved DNS. Therefore, at least for developed turbulent flows it should be possible in principle to store only part of the modes used in the DNS and still have a complete representation of the flow. This could resolve the problem of an efficient use of DNS results by a wide research community. At the same time a study in this direction can give the answer to a deep fundamental question concerning the nature of turbulence, namely, the question of the level of redundancy in turbulence data.

Determining the dimension of the attractor and storing the amplitudes, with the number of modes slightly larger than this dimension, does not actually solve the problem. Indeed, since the attractor itself is unknown, even if the stored modes determine the state of the dynamical system on the attractor uniquely, there is no way to determine the amplitudes of the remaining modes. It is also not clear of which mode amplitudes should be stored.

In the present study the ideas of the so-called determining or master modes are used as a tool for resolving this difficulty.

1.3 Overview of Relevant Literature

It is generally agreed that turbulent flow has an energy cascade (due to the inertial (nonlinear) term in the Navier-Stokes equations) of large eddies breaking up progressively into ever smaller sized eddies (fine scale components). The empirical theories predict a wave number k whose reciprocal $1/k$ represents a minimal spatial scale below which the viscosity forces dominate and break down the fine scale components (represented by wave numbers above k) so fast that these fine scales become of no dynamical consequence. Then the essential dynamics of the flow can be char-

acterized by the behavior of the wave numbers below k . The natural consequence of this view of turbulence is that the behavior of the solutions of the Navier-Stokes equations (NSE) can often be adequately represented within a finite-dimensional space.

There are three main approaches toward characterizing the finite-dimensional nature of solutions of the NSE: (1) estimating the dimension of the attractor, (2) making connections with the empirical theories of turbulence due to Kolmogorov [10], and (3) obtaining an estimate on the number of ‘determining modes’. Following this latter approach Foias and Prodi [11] gave an upper estimate on the number of determining modes for the 2D Navier-Stokes equations; see [12] and the references contained therein for further improvement to these results. Foias and Temam [13] first demonstrated that the 2D Navier-Stokes equations have a finite-dimensional attractor, while Constantin, Foias, and Temam [14] provided the first mathematically rigorous versions of the Kraichnan theories of 2D turbulence [15], which are an analogue of the 3D theories of Kolmogorov. Note that all of these results, and by far most of the mathematical results on turbulence that have followed, are restricted to 2D.

The existence of a global attractor for the 2D Navier-Stokes equations was first proved for bounded domains in the works of O. Ladyzhenskaya [16] and C. Foias and R. Temam [13], with the latter work showing also the finite dimensionality of the attractor in the sense of the Hausdorff dimension (see also [17], [18] and [19]). Also Foias and Temam showed in [20] that a sufficient number of “nodal values” will determine the asymptotic behaviour of a solution of the 2D incompressible Navier Stokes equations. In particular, they showed that if $\mathbf{u}(x, t)$ and $\mathbf{v}(x, t)$ are two solutions of the equation

$$\frac{\partial \mathbf{u}}{\partial t} - \nu \Delta \mathbf{u} + (\mathbf{u} \cdot \nabla) \mathbf{u} + \nabla p = f \quad (1.1)$$

$$\nabla \cdot \mathbf{u} = 0, \quad x \in \Omega \quad (1.2)$$

with periodic boundary conditions, then there exists a distance δ such that for any finite collection of nodes in $\Omega, \{x_1, \dots, x_k\}$ with

$$\min_{1 \leq j \leq k} |x - x_j| \leq \delta \quad \forall x \in \Omega \quad (1.3)$$

and

$$\sup_{1 \leq j \leq k} |\mathbf{u}(x_j, t) - \mathbf{v}(x_j, t)| \rightarrow 0, \quad t \rightarrow \infty \quad (1.4)$$

one has

$$\sup_{1 \leq j \leq k} |\mathbf{u}(x, t) - \mathbf{v}(x, t)| \rightarrow 0, \quad t \rightarrow \infty$$

Since the asymptotic behaviour on this collection of nodes fixes the asymptotic behaviour of the whole solution, they have been termed a set of “determining nodes”. Since then, better estimates of the maximum separation δ which guarantees this result have been obtained by Foias et al. [21], Foias and Titi [22] and Jones and Titi [23], [24] (see also [25] for a more general discussion of “determining functionals”). If the finite collection of points (nodes) in the physical space is replaced with a finite collection of points (modes) in the spectral space then one arrives at the idea of master, or determining modes. It is clear that the number of determining modes or nodes should depend on the forcing, the viscosity and the size of the domain. In [26] Friz and Robinson considered the solutions lying on the global attractor of the two-dimensional Navier Stokes equations with periodic boundary conditions and analytic forcing. They showed that in this case the value of a solution at a finite number of nodes determines elements of the attractor uniquely, proving a conjecture due to Foias and Temam [13].

In the late 1960s satellite observation systems began producing data on the climate that was nearly continuous in time. Charney, Halem, and Jastrow [27] proposed using the equations of the atmosphere themselves for processing this data and

obtaining improved estimates of the current atmospheric state. Their method, called *continuous data assimilation*, is to insert the observational measurements directly into a numerical atmospheric model as the latter is being integrated in time. The data assimilation process can be described as a procedure that uses observational data to improve the prediction made by an mathematical model. For example, consider a computational model where many properties are only expressed approximately. Typically, the assimilation process can be outlined as a two step process (Yang & Cotton [28]). Forecast step: $\mathbf{w}_n^f = F[\mathbf{w}_{n-1}^a]$ and analysis step: $\mathbf{w}_n^a = \mathbf{w}_n^f + d_n$. where \mathbf{w}_n represents model state variable at time step n ; $F[.]$ is the mathematical (forecast) model, superscripts f and a denote forecast and analyzed values respectively, and d_n is the innovation of the observational data. In general terms, data assimilation techniques can be divided into 1) *intermittent data assimilation* where the observations are objectively analyzed along with the output from a numerical model in order to improve the estimates in data-sparse regions or to improve estimates of poorly sampled variables and 2) *continuous data assimilation* where data is ingested into a numerical model during a simulation. In recent years, data assimilation methods have been developed and used in many research areas. The first application of data assimilation techniques were in meteorology [29], and today it is a key component of numerical weather and climate forecasts. Currently all of the major operational weather forecasting centers use data assimilation to improve the accuracy of their forecasts [30, 31, 32].

Continuous data assimilation was used by Browning, Henshaw and Kreiss [33] and Henshaw, Kreiss and Ystrom [2] to study decaying turbulence in the two-dimensional incompressible Navier-Stokes equations. In [1] the connection between continuous data assimilation and the theory of determining modes was made clear. In the mathematical setting, continuous data assimilation was used to construct two solutions to the two-dimensional Navier-Stokes equations that satisfy the hypothesis of the theory of determining modes. Thus, the theory of determining

modes guarantees that the approximate solution obtained by continuous data assimilation converges to the true solution over time provided enough modes are used as observational data.

Olson and Titi (see [1]) studied the number of determining modes necessary for continuous data assimilation in the two-dimensional incompressible Navier-Stokes equations. The focus was on how the spatial structure of the body forcing affects the rate of continuous data assimilation and the number of determining modes. They represented $u_1(t)$ as a physical reality at time t and represented the observational measurements corresponding to $u_1(t)$ at time t by $P_\lambda u_1(t)$, where P_λ is a finite-rank orthogonal projection. Here λ represents a parameter, namely the resolution of the measuring equipment. Let $u_2(t)$ be the approximation to $u_1(t)$ obtained from continuous data assimilation of the observational measurements $P_\lambda u_1(\tau)$ over the time interval $\tau \in [0, t]$. Their goal was to find conditions on λ in terms of the other physical parameters of the system which guarantee that $u_2(t)$ will converge to $u_1(t)$ as $t \rightarrow \infty$. They assumed an idealized situation in which the observational measurements $P_\lambda u_1(t)$ were error free; therefore, there was no need for the additional filtering that would be necessary in applications.

Given a particular forcing function and initial condition u_0 the data assimilation parameter λ for P_λ was then varied to determine its effect on the time evolution of $\|u_1 - u_2\|$. The results are illustrated in figure 1.1. Convergence is not always monotonic but, it is, on average, exponential in time.

Olson and Titi [34] also studied numerically how the number of determining modes in the 2D Navier Stokes equation depends on the Grashof number. The Grashof number is defined as

$$Gr = \frac{L^2 F}{4\pi^2 \nu^2},$$

where

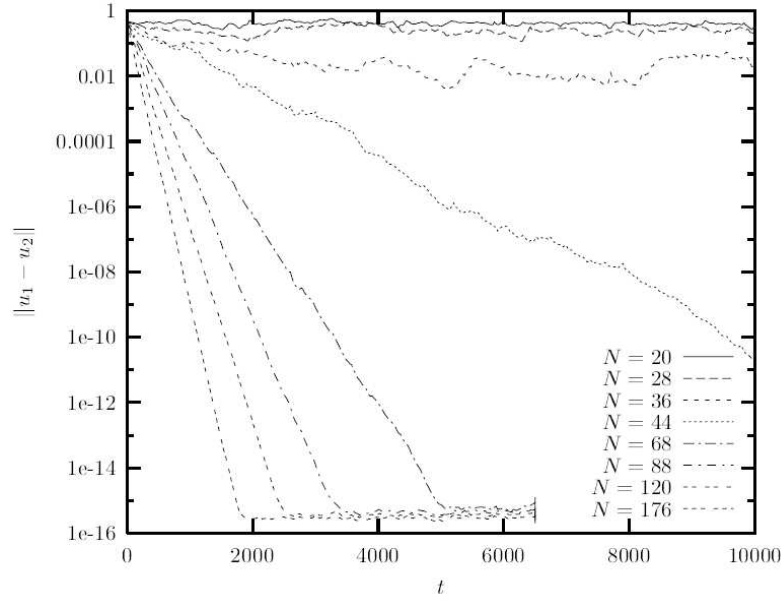


Figure 1.1: Evolution of $\|u_1 - u_2\|$ with different λ for continuous data assimilation on N Fourier modes, obtained by Olson & Titi [1].

$$F = \limsup_{t \rightarrow \infty} |f(t)|.$$

where L -periodic torus $\Omega = [0, L]^2$ and ν -kinematic viscosity. Note that if f is time independent, then Gr is the Grashof number $G = (L^2 |f|)/(4\pi^2 \nu^2)$,

There have been many studies to estimate the number of degrees of freedom of the solutions for the Navier-Stokes equation in terms of the Grashof number (see [35]). The first reasonable rigorous estimate on the number of determining modes in terms of the Grashof number was provided by Foias [21]. In their work Olson and Titi increased the Grashof number and observed through numerical computation that the number of master modes stabilizes at some finite value as the Grashof number increases. Their conclusion was following: “This unexpected result implies that our theoretical understanding of continuous data assimilation is incomplete until an analytic proof which makes use of the non-linear term in the Navier-Stokes equations is found”

Keefe, Kim and Moin (see [7]) performed a coarse grained $16 \times 33 \times 8$ numerical

simulation of a plane channel flow. In their work a lower bound on the Lyapunov dimension, D_λ , of the attractor underlying turbulent, periodic Poiseuille flow at a pressure-gradient Reynolds number of 3200 was calculated to be approximately 352. They obtained this result for a plain channel flow in a box of the size $L_x = L_y = 1.6\pi$ and $Re_\tau = 80$. For the resolution $32 \times 33 \times 32$ simulation, they argue that the actual dimension of the attractor underlying the motion on the given computational domain is approximately 780. Their calculations suggest that this spatially periodic turbulent shear flow is deterministic chaos, and that a strange attractor does underly solutions to the Navier-Stokes equations in such flow.

In [2] Henshaw, Kreiss and Ystrom state the following conjecture:

“The large-scale modes determine the basic structure of the flow and set up the dissipative structures. . . .”

They considered the incompressible Navier-Stokes equations for the velocity \mathbf{u} and kinematic pressure p ,

$$\mathbf{u}_t + (\mathbf{u} \cdot \nabla)\mathbf{u} + \nabla p = \nu \nabla^2 \mathbf{u}, \quad \nu > 0, \quad (1.5)$$

$$\nabla \cdot \mathbf{u} = 0, \quad (1.6)$$

with initial conditions given at time t_0

$$\mathbf{u}(\mathbf{x}, t_0) = \mathbf{u}_0(\mathbf{x}), \quad (1.7)$$

and with periodic boundary conditions on the box with sides of length 2π and volume V . They expanded the solution into a Fourier series

$$\mathbf{u}(\mathbf{x}, t) = \sum_{\mathbf{k}} \hat{\mathbf{u}}(\mathbf{k}, t) e^{i\mathbf{k}\mathbf{x}} \quad (1.8)$$

$$p(\mathbf{x}, t) = \sum_{\mathbf{k}} \hat{p}(\mathbf{k}, t) e^{i\mathbf{k}\mathbf{x}} \quad (1.9)$$

where $\mathbf{k} = (k_1, k_2, k_3)$ is a multi-index with $k = |\mathbf{k}| = \sqrt{k_1^2 + k_2^2 + k_3^2}$. They split the solution into two parts $\mathbf{u} = \mathbf{u}^1 + \mathbf{u}^2$ representing the large-scale and small-

scale motions. They defined the large-scale as the sum of the first k_c Fourier modes in each direction, and the small-scale as the sum of the remaining modes. They expressed and solved the Navier Stokes equations as a system for the large-scale and the small-scale. After solving these equations they generated a solution that they called the *playback* solution. They defined the playback solution $\mathbf{u}_p(\mathbf{x}, t, k_c) = \mathbf{u}_p^1 + \mathbf{u}_p^2$ to be solution of the equations when the first k_c modes are set equal to those from the reference solution for all the time, $\mathbf{u}_p^1(\mathbf{x}, t) = \mathbf{u}^1(\mathbf{x}, t)$, but having zero initial conditions for the small-scale, $\mathbf{u}_p^2(\mathbf{x}, t) = 0$. In practice they solved for all Fourier modes but replaced, at each time step, the large-scale modes with those computed from the reference calculation. They tried to find the smallest value of k_c for which the time evolution of the large-scale sets up the the small-scale. The figure 1.2 shows the two-dimensional results for errors in the playback solution. The figures show the relative errors for different values of the cut-off wave number k_c and different values of ν . The relative error in the playback solution was defined as

$$\epsilon_p(t) = \frac{\|\mathbf{u}_p^2 - \mathbf{u}_r^2\|^2}{\|\mathbf{u}_r^2\|^2}$$

Their results show that a relatively few number of modes are required for the relative error to decrease. The error decreases more rapidly as k_c is increased. As ν was decreased more modes were required to attain the same relative error. Figures 1.3 and 1.4 show a comparison of vorticity contours for the play-back solution and reference solution with $k_c = 16$. In each figure one can see the play-back solution on the left and the reference solution on the right. The initial conditions for the playback solution was taken from the reference solution at time $t = 50$. At the initial time $t = 50$ (figure 1.3) the two solutions are very different. By time $t = 200$, figure 1.4, the play-back solution is almost the same as the reference solution. Many of the fine scale features were recovered. The relative error was 7%. Their results show that the small-scale features can be reconstructed to a surprising degree of accuracy even for a relatively few number of large-scale modes.

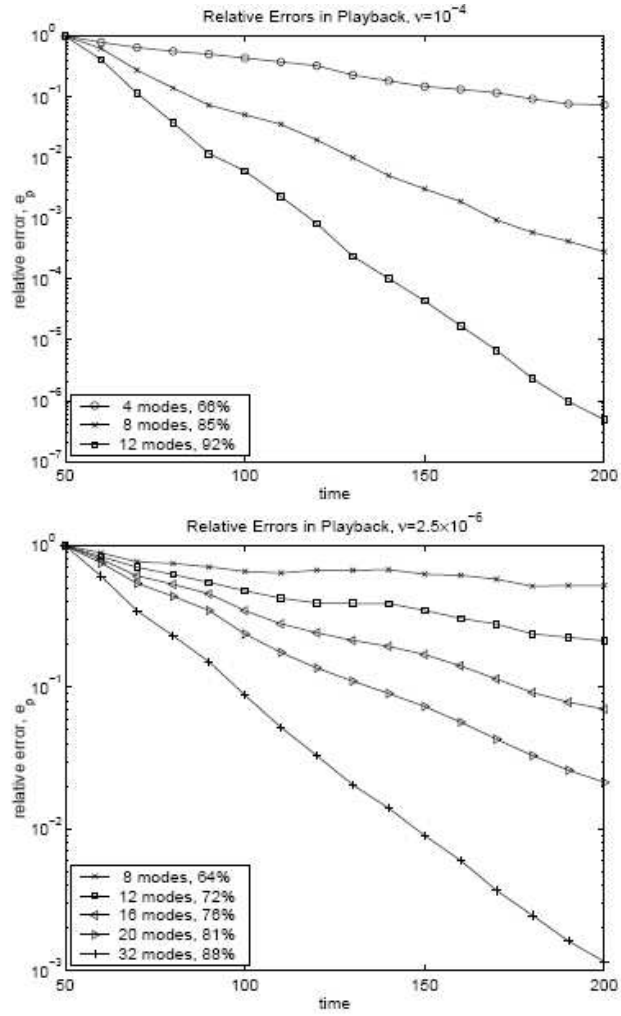


Figure 1.2: Two-dimensional Navier-Stokes solutions obtained by Henshaw, Kreiss & Ystrom [2]: the relative errors in the high modes for the playback solutions as a function of time and a function of the cut-off wave number k_c

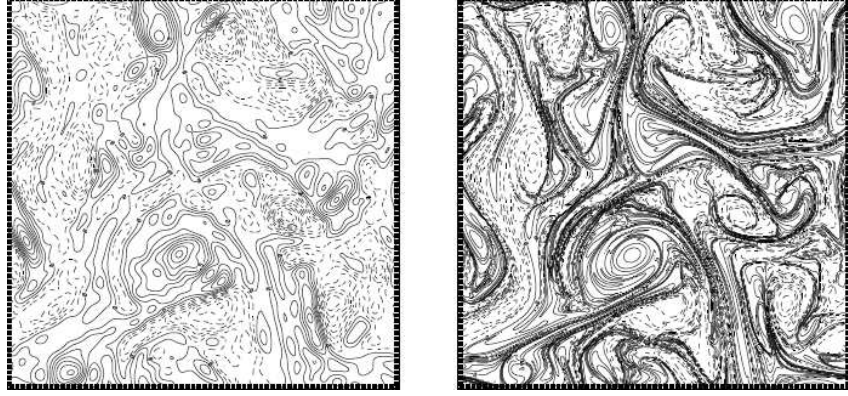


Figure 1.3: Two-dimensional Navier-Stokes solutions obtained by Henshaw, Kreiss & Ystrom [2]: contours of the vorticity at the starting time for the play-back computation. Left: play-back solution, right: reference solution. The initial conditions for the play-back solution were set equal to the lowest $k_c = 16$ modes of the reference solution at $t = 50$.

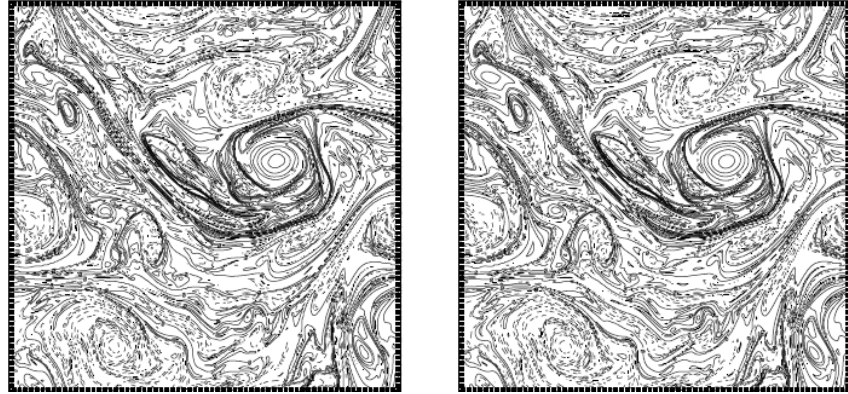


Figure 1.4: Two-dimensional Navier-Stokes solutions obtained by Henshaw, Kreiss & Ystrom [2]: solutions at time $t = 200$. Left: play-back solution, right: reference solution.

In [3] Yoshida, Yamaguchi and Kaneda studied the effect of data assimilation of large-scale eddies on small-scale eddies in turbulence by direct numerical simulations of Navier-Stokes turbulence with Taylor microscale Reynolds numbers up to 179. They defined $\mathbf{u}^{(1)}(\mathbf{x}, t)$ and $\mathbf{u}^{(2)}(\mathbf{x}, t)$ be two three-dimensional incompressible turbulent flow fields obeying the same Navier-Stokes equations, but with different initial conditions. They applied periodic boundary conditions in each of the Cartesian coordinates with period 2π . They represent $\hat{\mathbf{u}}^{(i)}(\mathbf{k}, t)$ ($i = 1, 2$) as the Fourier transform of the velocity field $\mathbf{u}^{(i)}(\mathbf{x}, t)$ with respect to \mathbf{x} . The coarse grained data of $\mathbf{u}^{(1)}$ was assimilated to $\mathbf{u}^{(2)}$ by replacing $\hat{\mathbf{u}}^{(2)}(\mathbf{k}, t)$ by $\hat{\mathbf{u}}^{(1)}(\mathbf{k}, t)$ for low wave number modes satisfying $k \equiv |\mathbf{k}| < k_a$ at every time interval T_a : hence $\hat{\mathbf{u}}^{(2)}(\mathbf{k}, t_0 + nT_a) = \hat{\mathbf{u}}^{(1)}(\mathbf{k}, t_0 + nT_a)$ ($k < k_a, n = 1, 2, \dots$). The velocity field $\mathbf{u}^{(1)}$ is a model of “true field” and $\mathbf{u}^{(2)}$ is a model of “simulated field with the use of coarse grained data of the true field”. Their results are shown in figure 1.5. The figure shows $\Delta(t)$ versus nondimensional time t/τ , for $Re_\lambda = 107$ and some k_a 's. One can see that if k_a is low, $\Delta(t)$ increases with time after some initial transient period. Their results show that even if the data of small-scale eddies are lost at some initial instant, they can be regenerated from the data of large-scale eddies.

The conventional theory of turbulence suggests that turbulent flow has a finite number of degrees of freedom (see [7], [36]). The notions of determining modes or master-modes are rigorous attempts to identify those parameters that control turbulent flows. Since the problem of global existence and uniqueness of strong solutions to the 3D Navier-Stokes equations is still an open question, most of the research on estimating these parameters has been concentrated on the 2D case, as can be seen from the overview given above. Some results were also obtained for 3D space-periodic flows. The research described in the present thesis, is devoted to three-dimensional turbulence in a wall-bounded flow.

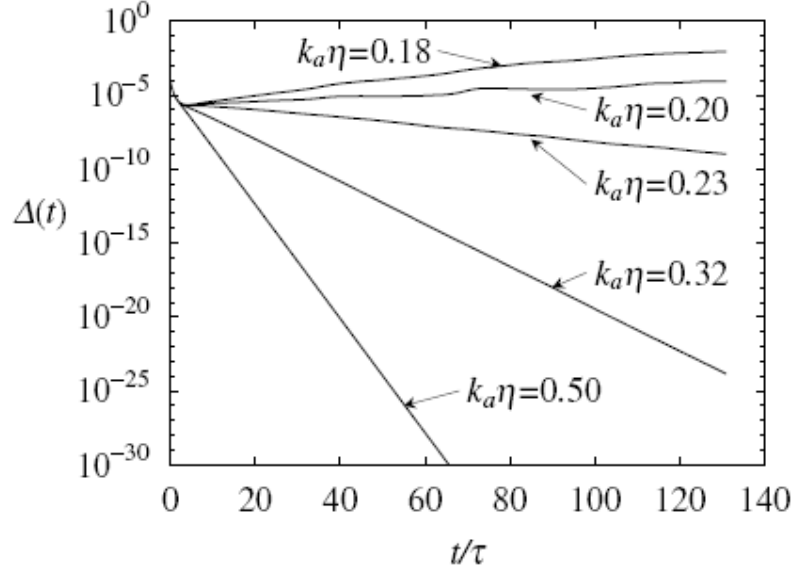


Figure 1.5: Evolution of $\Delta(t)$, the energy of the difference field $\mathbf{u}^{(2)} - \mathbf{u}^{(1)}$, for various k_a , obtained by Yoshida, Yamaguchi & Kaneda [3]. η is the Kolmogorov length scale.

1.4 Outline of the thesis

The chapters are presented in such a sequence that the emphasis is shifted from background aspects needed to conduct this study, starting with an introduction to the numerical implementation of the pseudo-spectral code at the beginning to the physical aspects of finding the minimal number of master modes necessary for continuous data assimilation in 3D turbulence flow. Specifically, in chapter 2, we define master modes and we briefly explain the basic theory of attractors and determining projections.

In chapter 3 we present the mathematical aspects of the tools that have been used in order to achieve the aims of this study. These relate to the specifics of the pseudo-spectral code that has been used to solve the Navier-Stokes equations. At the end of this chapter we analyse the results of the DNS of fully developed turbulent channel flow carried out with $Re_\tau = 360$. The comparisons and visualizations show that the solution corresponds to the fully developed turbulent channel flow and that the pseudo-spectral channel flow DNS code works correctly. The following chapter

describes how the DNS code was modified for the purposes of the present study. It also describes the verification of the modified master-slave code.

Chapter 5 shows results from the master-slave code. We determine the number of master modes using a spatial domain with streamwise and spanwise periods of 1.6π similar to that used by Keefe *et al.* [7]. This initial calculation was performed with 32786 Chebychev-Fourier modes. The results are compared with the results of Keefe, Kim and Moin. Also this chapter shows the minimal number of the master modes for Reynolds number 360 for one particular domain size. We also explore in detail the organised structures of developed turbulent flow calculated from master modes only and from slave modes. In particular, we are interested in what organised structures will appear in the master modes.

Chapter 6 shows an example of using master mode database. The example consists in finding a traveling wave in fully developed turbulence flow.

The final chapter provides a summary of conclusions and a short discussion of future work. Appendix A describe the master-mode database.

2 Master Modes

The purpose of this chapter is to define master modes and briefly explain the basic findings of the theory of attractors and determining nodes. In general, the number of modes that are necessary to fully describe a turbulent flow can be estimated using Kolmogorov's [37] ideas (see also Landau & Lifschitz [38]). It was rigorously shown that the attractors associated with the Navier-Stokes equations have finite dimension (see for instance [39]). Furthermore, physically relevant estimates on the dimension of the attractor were derived that fully agree with the estimates of the complexity of turbulent flows following from the conventional theory of turbulence. The first results in this direction are due to Foias & Prodi [11] and Ladyzenskaya [40]. We shall present two of the main approaches: attractors and determining nodes.

2.1 Attractor

An attractor is a region in the phase space that attracts all orbits starting in its basin of attraction. For the Navier-Stokes equations the phase space is a Hilbert space of infinite dimension H . For typical boundary conditions, H is a subspace of $L^2(\Omega)^n$ made of vector functions u which are divergence free and which satisfy certain boundary conditions. Each point in H is a distribution of velocities in Ω and, for example, a stationary solution is represented by a point of H . The attractor is a compact subset in H to which all orbits starting in its basin of attraction (an open neighbourhood of the attractor) converge. The global attractor consists of all these attractors and certain exceptional orbits. The existence of a global attractor for the 2D Navier-Stokes equations was proved in Foias & Temam [41]. It was shown that the attractors have finite dimension. Hence each orbit of the phase space converges to a finite dimensional set.

There have been various attempts to apply the theory of global attractors to the 3D Navier-Stokes equations. There are two results: Foias & Temam [41] constructed a set, consisting of strong solutions, that attracts all weak solutions in the weak topology of the natural phase space; and Sell [42] analysed the induced single-valued flow on the phase space consisting of all solutions of the equation (an element of this space is a complete trajectory in the original phase space), showing that this has a global attractor.

2.2 Determining modes.

Foias and Prodi [11] introduced the notion of “determining modes” for two solutions of the 2D Navier-Stokes equations: if $P_N u$ denotes the orthogonal projection of u onto the space spanned by the first N (generalized) Fourier modes, they showed that if N is sufficiently large then

$$|P_N u(t) - P_N v(t)| \longrightarrow 0, \quad t \longrightarrow \infty \quad (2.1)$$

implies that

$$|u(t) - v(t)| \longrightarrow 0, \quad t \longrightarrow \infty \quad (2.2)$$

Foias and Temam [20] introduced the concept of “determining nodes”. Their conjecture is:

There exists a finite number of nodes such that the solutions on the global attractor, for the 2D NSE, are determined in a unique fashion by their values at these nodes.

A collection of points x_1, \dots, x_k in the domain Ω is *determining* if

$$\max_{j=1, \dots, k} |u(x_j, t) - v(x_j, t)| \longrightarrow 0, \quad t \longrightarrow \infty \quad (2.3)$$

implies that

$$\sup_{x \in \Omega} |u(x, t) - v(x, t)| \longrightarrow 0, \quad t \longrightarrow \infty \quad (2.4)$$

Foias and Temam showed that there exists a δ such that if for every $x \in \Omega$,

$$|x - x_j| < \delta \text{ for some } j \in \{1, \dots, k\},$$

then the collection of nodes is determining. We note that the theory of determining modes, nodes and also “volume elements” has been developed further in a series of papers by Jones and Titi [23], and set within a general framework by Cockburn et al. [43]. Determining modes/nodes are also called master modes/nodes.

2.3 Master modes

Definition 2.1

Let two solutions u_A and u_B of the Navier-Stokes equations be represented as

$$\begin{aligned}\bar{u}_A &= \sum A_n(t)u_n(x) = \sum \bar{u}_{An} \\ \bar{u}_B &= \sum B_n(t)u_n(x) = \sum \bar{u}_{Bn}\end{aligned}$$

where $u_n(x)$ forms a full basis. Then from the Foias and Prodi theory it follows that

$$\exists N : \forall \bar{u}_A, \bar{u}_B : (\bar{u}_{Ai} = \bar{u}_{Bi} \forall i \leq N) \implies \|\bar{u}_A - \bar{u}_B\| \rightarrow 0, t \rightarrow \infty \quad (2.5)$$

Foias and Prodi proved (1.1) only in 2D. For 3D flow the existence of master modes is an open question.

In this case we can say that a subset X of the set $\{\bar{u}_{Bn}\}$ of all the modes of the solution \bar{u}_B contains all master modes if for any solution \bar{u}_A such that

$$\bar{u}_{Ai} = \bar{u}_{Bi} \quad \forall \bar{u}_{Bi} \in X$$

the following holds

$$\forall \epsilon \geq 0 \quad \exists T : \quad \|\bar{u}_A(t) - \bar{u}_B(t)\| < \epsilon, \quad \forall t > T \quad (1.2)$$

So, if the behavior of the N modes from time $t = -T$ till $t = 0$ is known then it is possible to calculate the whole solution at $t = 0$ with an error that exponentially decays with T . It means that the ultimate behaviour of the system, when T is very

large, is fully determined by these N modes. This is why they are called *master, or determining modes*. Theoretical estimates were obtained for the number of master modes in specific conditions (Foias *et al.*, 1983; Jones and Titi, 1993).

When the solution on the attractor is considered, the existence of the master modes suggests that the velocity field might be represented as a sum $u = u_m + u_s$, where $u_m = u_m(x; t)$ corresponds to the master modes and $u_s = u_s(x; t)$ is the remaining part, related to u_m by a functional relation $u_s = \phi[u_m]$.

3 Direct Numerical Simulation of turbulent flow

The purpose of this chapter is to describe the numerical tools which were made available for this research and to show comparisons of DNS statistics with those from the literature. For our direct numerical simulations we used the pseudo-spectral channel flow code of Sandham and Howard [6]. The chapter is divided into two sections: the first section describes of the numerical method; the second section shows the validation results.

3.1 Numerical model

The direct numerical simulations presented in this thesis have all been performed with the pseudo-spectral algorithm. In a spectral method the solution is approximated by an expansion in smooth functions, e.g. trigonometric functions. The earliest applications of the pseudo-spectral method to partial differential equations were developed by Kreiss & Oliger [44] and Orszag [45]. The term pseudo-spectral refers to calculating the multiplications in the non-linear terms in physical space to avoid the evaluation of convolution sums. The transformation between physical and spectral space can be efficiently done by Fast Fourier Transform (FFT) algorithms, which became generally known in the 1960's, see Cooley & Tukey [46]. Pseudo-spectral methods became widely used for a variety of flows during the 1980's. Early turbulent boundary layer results were presented by Spalart & Leonard [47], who used a parallel approximation of the boundary layer. The first spatial (no parallel approximation) turbulent boundary layer computation was performed by Spalart & Watmuff [48].

The code used for the simulations in this thesis was obtained by modifying the pseudo-spectral channel flow code of Sandham and Howard [6]. It uses Fourier series expansion in the wall parallel directions and Chebyshev series in the nor-

mal direction and pseudo-spectral treatment of the non-linear terms. The time advancement used is a four-step low storage third-order Runge-Kutta method for the non-linear terms and a second-order Crank-Nicolson method for the linear terms. Aliasing errors from the evaluation of the non-linear terms are removed by the 3/2-rule when the horizontal FFTs are calculated.

The numerical code is written in FORTRAN and consists of two major parts; a linear part where the equations are solved in spectral space, and a non-linear part where the non-linear terms in the equations are computed in physical space.

3.2 Problem formulation

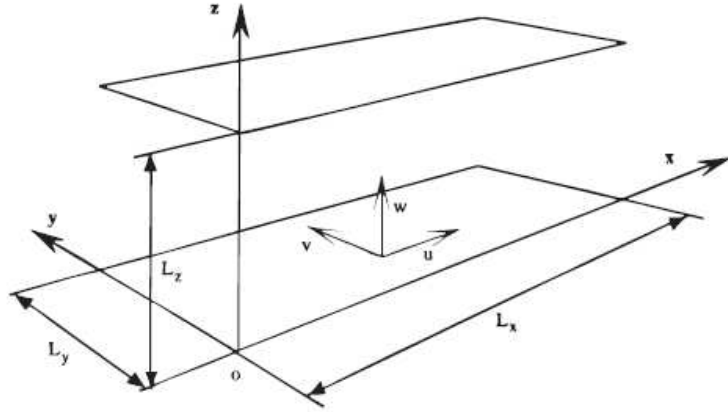


Figure 3.1: Sketch of the fluid flow domain.

Numerical calculations were performed for the flow in a plane channel. The governing equations of incompressible flow, that is the continuity equation and the momentum equations, were made non-dimensional with the channel half-width h^* and the friction velocity $u_\tau^* = \sqrt{\tau_w^*/\rho^*}$, where τ_w^* is the wall shear stress and ρ^* is the density. Here asterisks are used to denote dimensional quantities. The Reynolds number is $Re_\tau = u_\tau^* h^* / \nu^*$. The non-dimensional quantities are then defined as $u_i = u_i^* / u_\tau^*$, $x_i = x_i^* / h^*$, $p = p^* / \rho^* u_\tau^* u_\tau^*$, $t = t^* u_\tau^* / h^*$ and the normalized mean pressure

gradient is $dP/dx = -1$. The continuity equation has the form

$$\nabla \cdot \mathbf{u} = 0,$$

while the governing momentum equations are

$$\frac{\partial \mathbf{u}}{\partial t} + \mathbf{u} \cdot \nabla \mathbf{u} = -\nabla p - \mathbf{e}_l \frac{dP}{dx} + \frac{1}{Re_\tau} \nabla^2 \mathbf{u},$$

where \mathbf{e}_l is the unit vector of x -axis. In the above equations the pressure term has been split into a mean P and fluctuation p components. The bold quantities indicate vectors in all the formulations. The coordinates are set as x in the streamwise direction, y in the spanwise direction and z in the wall-normal direction, with the channel walls at $z = \pm 1$. A no-slip boundary condition is imposed on the wall. Periodicity conditions are used in the directions parallel to the walls: $\mathbf{u}(x + L_x, y, z, t) = \mathbf{u}(x, y, z, t)$, $p(x + L_x, y, z, t) = p(x, y, z, t)$, $\mathbf{u}(x, y + L_y, z, t) = \mathbf{u}(x, y, z, t)$, and $p(x, y, z, t) = p(x, y + L_y, z, t)$, where L_x and L_y are the periods, equal to the dimensions of the computation domain.

3.3 Spatial Derivatives

We use a spectral discretization in all spatial directions (Fourier - Fourier - Chebyshev). It is widely known that Fourier spectral methods impose periodic boundary conditions, while Chebyshev methods can be applied to non-periodic boundary conditions. In the Sandham and Howard spectral code [6], Fourier discretization is used for the horizontal planes while the Chebyshev tau method is used for the wall-normal direction to account for the non-periodicity in that direction. As per the details given in Hu et.al. [15], in the horizontal plane, a two-dimensional Fourier transformation (real to complex) from real to wave space is performed in the streamwise direction, followed by a complex to complex Fourier transformation in the spanwise direction. In the streamwise direction, only half the Fourier modes need to be stored due to conjugate symmetry of positive and negative wavenumber

modes for real variables. A real quantity $q(x, y)$ is transformed to $\hat{q}(k_x, k_y)$ in discrete Fourier space by the successive operations:

$$\tilde{q}(k_{xl}, y_j) = \frac{1}{N_x} \sum_{i=0}^{N_x-1} q(x_i, y_j) e^{-i2\pi li/N_x} \quad (2.3.21)$$

$$\tilde{\tilde{q}}(k_{xl}, k_y m) = \frac{1}{N_y} \sum_{j=0}^{N_y-1} \tilde{q}(k_{xl}, y_j) e^{-i2\pi lj/N_y} \quad (2.3.22)$$

where $i = \sqrt{-1}$; N_x and N_y are the total number of grid points (both even) in the streamwise and spanwise directions. In physical space we have

$$x_i = \frac{L_x i}{N_x}, \quad 0 \leq i \leq N_x \quad (2.3.23)$$

$$y_j = \frac{L_y j}{N_y}, \quad 0 \leq j \leq N_y \quad (2.3.24)$$

The spatial wavenumbers k_{xl} , k_{ym} are given by

$$k_{xl} = \frac{2\pi l}{L_x}, \quad -N_x/2 \leq l \leq N_x/2 \quad (2.3.25)$$

$$k_{ym} = \frac{2\pi m}{L_y}, \quad -N_y/2 \leq m \leq N_y/2 \quad (2.3.26)$$

Here l and m are Fourier modes in streamwise and spanwise directions, respectively. The two-dimensional backward transformation is done with a spanwise complex to complex transformation, followed by a streamwise complex to real transformation

$$\tilde{q}(k_{xl}, y_j) = \sum_{m=-N_y/2}^{N_y/2} \tilde{\tilde{q}}(k_{xl}, k_{ym}) e^{-i2\pi mj/N_y} \quad (2.3.27)$$

$$q(x_i, y_j) = \tilde{q}(0, y_j) + 2 \sum_{l=1}^{N_x/2} \tilde{q}(k_{xl}, y_j) e^{-i2\pi li/N_x} \quad (2.3.28)$$

Chebyshev transforms are used for the wall-normal direction:

$$q_m = \sum_{k=0}^{N_z-1} \tilde{q}_m(z_n) T_k(z_n) \quad (2.3.29)$$

$$\tilde{q}_m = \frac{2}{\pi c_k} \int_{-1}^1 q_m(z_n) T_k(z_n) w(z_n) dz \quad (2.3.30)$$

Here N_z is the number of wall-normal grid points, while Chebyshev polynomials of the first kind, Chebyshev-Gauss-Lobato coordinates z_n and weights are given as:

$$T_k(z_n) = \cos(k \arccos(z_n)) \quad (2.3.31)$$

$$z_n = \cos\left(\frac{\pi n}{N_z}\right) \quad (2.3.32)$$

$$w_n = \frac{\pi}{N_z}, \quad 1 \leq n \leq N_z - 1$$

$$w_n = \frac{\pi}{2N_z}, \quad n = 0, N \quad (2.3.33)$$

3.4 Implementation on Parallel Computers

The Sandham and Howard [6] code used in the present study is parallel. The domain decomposition technique is employed to divide the domain into blocks where each block is assigned to a certain processor. Hence different modes of Fourier and Chebyshev discretised velocity, modified pressure and vorticity are stored on different processors. In Fourier space, all the mathematical manipulations on these variables can be performed locally except evaluation of the nonlinear terms. In the pseudospectral approach the nonlinear terms are computed in physical space and for that forward and inverse transforms of the variables need to be performed. Hence information from all the processors is required which means devising an efficient strategy for data transfer between the processors.

The data storage approach is based on data decomposition analogous to slicing a loaf of bread, with each slice stored on one processor, see [6]. Figure 3.2 shows the decomposition of the domain. Fourier or Chebyshev transforms in two of the

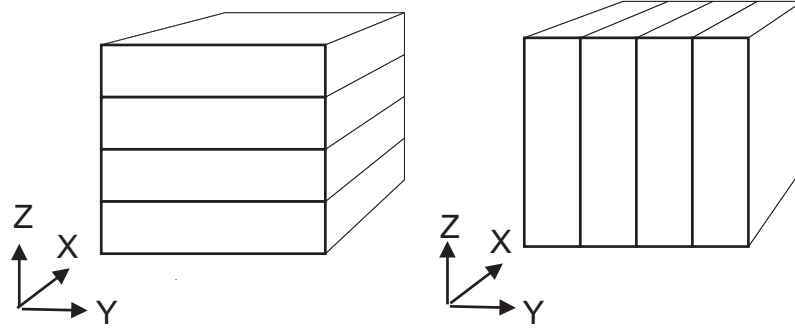


Figure 3.2: Decomposition of the domain.

three directions can be performed locally on each processor. However, to perform transformation in the third direction a global transpose needs to be performed. After the transpose, the data is “re-sliced” in a perpendicular direction allowing the transform in the remaining direction to be carried out and the nonlinear terms to be computed.

MPI Library has been used to transfer small chunks of data from each processor in order to perform a global transpose. The whole process entails labelling the address of each processor that requires the information, transferring the data, reading it by the receiving processor, and reconstructing the flow field. As the process involves data transfer from all the processors to each single processor, it can lead to choking of the buffer memory on the Myrinet bus especially on Linux clusters. The “choking” problem can be alleviated by allocating substantial buffer memory to each processor and this approach has been incorporated in the code. The dimension of the arrays used to store flow variables is $(N_x + 2) * N_y * (N_z + 2)$, but due to dealiasing larger arrays of the size $(3/2N_x + 2) * 3/2N_y * (3/2N_z + 2)$ have been used in the code. Efficient parallelisation [6] requires that $3/2N_z + 2$ is close to and less than an integer multiple of the number of processors.

The simulations described in this thesis have been performed on 32 and 64 processors of Beowulf Linux cluster “Iridis” of University of Southampton, on the computers at Computer Services for Academic Research (CSAR) at the University of Manchester and HPCx at the University of Edinburgh. All simulations used a

parallel code based on MPI protocol.

3.5 Test calculations

In conclusion on this chapter we describe calculations performed in order to verify that the particular version of the Sandham and Howard [6] code we use works correctly. Calculations with $Re_\tau = 360$ and $Re_\tau = 395$ were performed. The Reynolds number Re_τ is based on the dynamic velocity and the channel half-width. We will show comparisons between our results and results of Hu & Sandham [4] (referred to as HS hereafter) available at <http://www.dnsdata.afm.ses.soton.ac.uk/> for $Re_\tau = 360$.

Also we will compare our results with the statistics extracted from the simulation of Moser, Kim & Mansour [49] (referred to as MKM hereafter) available at <http://turbulence.ices.utexas.edu/data/MKM/chan395/>. These data include the mean velocities, the components of the Reynolds stress tensor, profiles of components of the vorticity, streamwise (x) one-dimensional spectra of velocity and the two-point correlations in the streamwise direction at $Re_\tau = 395$. The simulation parameters for the two cases are given in Table 3.1

Re_τ	L_x	L_y	$N_x \times N_y \times N_z$
360	12	6	$256 \times 256 \times 161$
395	6	3	$256 \times 256 \times 161$

Table 3.1: Simulation parameters for the two channel direct numerical simulations.

Figures 3.3 and 3.4 show the mean streamwise velocity profiles in global and wall coordinates. The comparison of velocities between present DNS and the results obtained by MKM and HS is very good. The mean velocity profiles normalized by wall coordinates and plotted against the law of the wall $u^+ = z^+$, which defines the viscous shear-layer, and $u^+ = 2.5 \log z^+ + 5.5$ for logarithmic region, is shown in

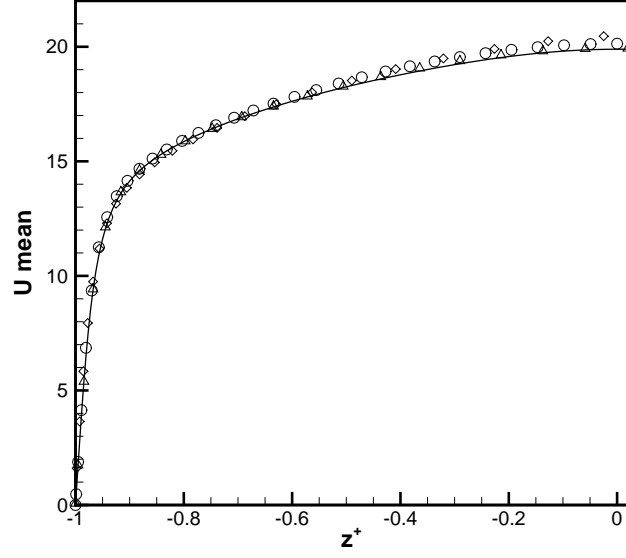


Figure 3.3: Mean velocity profile in global coordinates. Present (triangles), Hu & Sandham (solid line) for $Re_\tau = 360$ and present (circles), MKM (diamonds) for $Re_\tau = 395$

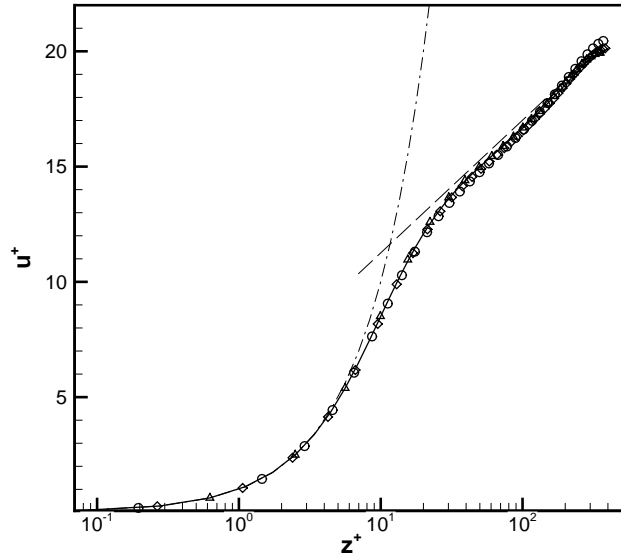


Figure 3.4: Mean velocity profile in wall coordinates. Present (triangles), Hu & Sandham (solid line) for $Re_\tau = 360$ and present (circles), KMM (diamonds) for $Re_\tau = 395$; $u^+ = 2.5 \log z^+ + 5.5$ (long dash); $u^+ = z^+$ (dash dot).

Figure 3.4. As can be seen, the present DNS and the results obtained by MKM and HS are in good agreement.

Two-point spatial correlations of velocities indicate the length scales of the turbulence structures within the channel. Since the channel flow is statistically stationary and homogenous in $x - y$ planes, the spatial correlations are only dependent upon the spatial separation between two points in that plane, and are shown only as functions of two variables: streamwise or spanwise separation.

The autocorrelations are defined as

$$R_{ij} = \frac{\overline{u_i(x_1, x_2, x_3)u_j(x_1 + r, x_2, x_3)}}{\sqrt{\overline{u_i^2}(x_1, x_2, x_3)} \sqrt{\overline{u_j^2}(x_1 + r, x_2, x_3)}} \quad (3.1)$$

Figures 3.5-3.6 show the streamwise and spanwise autocorrelations obtained from DNS at $z^+ = 10$. They show that u has the largest streamwise correlations, which is probably due to the alternating low- and high- speed streaks in the near-wall region. In order to use a periodic boundary condition, the computational domain must be large enough to include the largest turbulent structures. This can be checked by examination of the two-point correlation of velocity, as shown in Figure 3.5-3.6. The two-point correlations go to zero at maximum separation, demonstrating that the present computational domain is adequate.

Figures 3.7-3.8 show the terms in the budgets of turbulent kinetic energy from DNS compare very well with DNS values from HS and MKM. For the channel flow the equation for Reynolds-stresses reduces to

$$\frac{\partial \overline{u'_i u'_j}}{\partial t} = P_{ij} + T_{ij} + D_{ij} + \Pi_{ij} + \varepsilon_{ij} \quad (3.2)$$

$$P_{ij} = -\overline{u'_i v'} \frac{\partial \overline{u_j}}{\partial y} - \overline{u'_j v'} \frac{\partial \overline{u_i}}{\partial y} \quad (3.3)$$

$$T_{ij} = -\frac{\partial}{\partial y} \overline{v' u'_i u'_j} \quad (3.4)$$

$$D_{ij} = \frac{1}{Re} \frac{\partial^2}{\partial y^2} \overline{u'_i u'_j} \quad (3.5)$$

$$\Pi_{ij} = -\overline{(u'_i \frac{\partial p'}{\partial x_j} + u'_j \frac{\partial p'}{\partial x_i})} \quad (3.6)$$

and

$$\varepsilon_{ij} = -\frac{2}{Re} \overline{\frac{\partial u'_i}{\partial x_\ell} \frac{\partial u'_j}{\partial x_\ell}} \quad (3.7)$$

In the above equations, P_{ij} is the production due to mean velocity gradient, T_{ij} is the turbulence transport, D_{ij} is the viscous diffusion, Π_{ij} is the velocity-pressure-gradient term and ε_{ij} is the dissipation. After the flow has become statistically stable, the terms on the right hand side should sum to zero.

Figures 3.9-3.10 show the root mean square velocity fluctuations normalized by the wall shear velocity in wall coordinates for $Re_\tau = 360$ and $Re_\tau = 395$ from present DNS and also the figures show the *rms* from HS and MKM. Figure 3.11 shows the Reynolds stress distributions across the channel. As can be seen, the present DNS and the results obtained by MKM and HS are in good agreement.

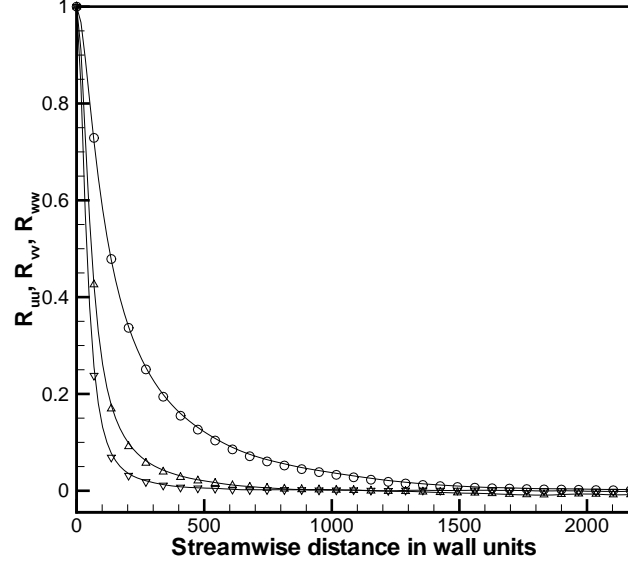
Figures 3.12-3.13 show energy spectra $E(u)$, $E(v)$, $E(w)$ in streamwise and span-wise direction integrated over the wall-normal. The integral is defined as:

$$E(k_x) = \int_0^H E(k_x, z) dz \quad (3.8)$$

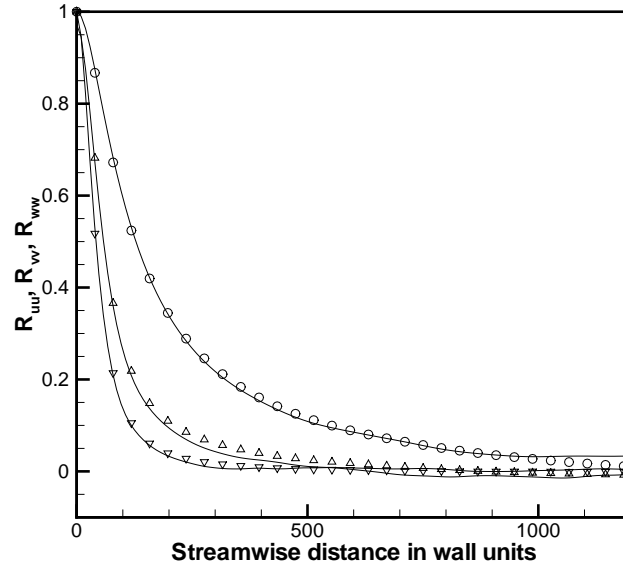
Velocity streaks in turbulent flow for $Re_\tau = 360$ at the top and bottom of the channel ($z^+ = 5.6$) can be seen at the Figure 3.15 and 3.16. The vorticity in the x -direction presented in Figure 3.14 is

$$\omega_x = \frac{\partial w}{\partial y} - \frac{\partial v}{\partial z}$$

These visualisations show the well-known features of turbulent flow. These comparisons and visualizations show that the solution corresponds to the fully developed turbulent channel flow and that the pseudo-spectral channel flow DNS code works correctly.

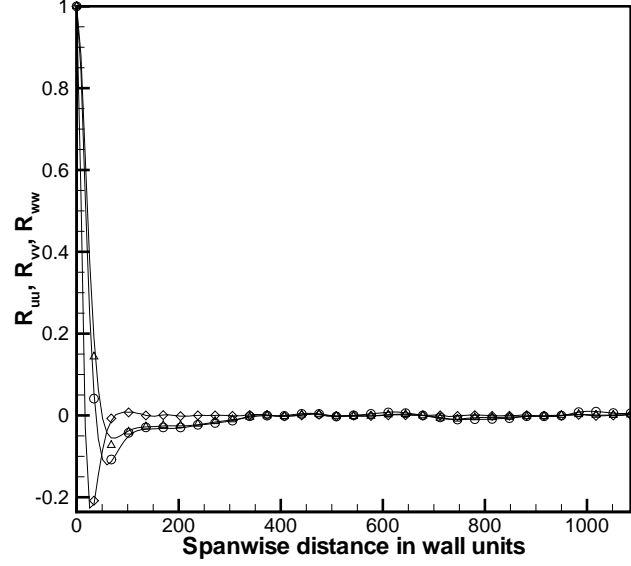


(a)

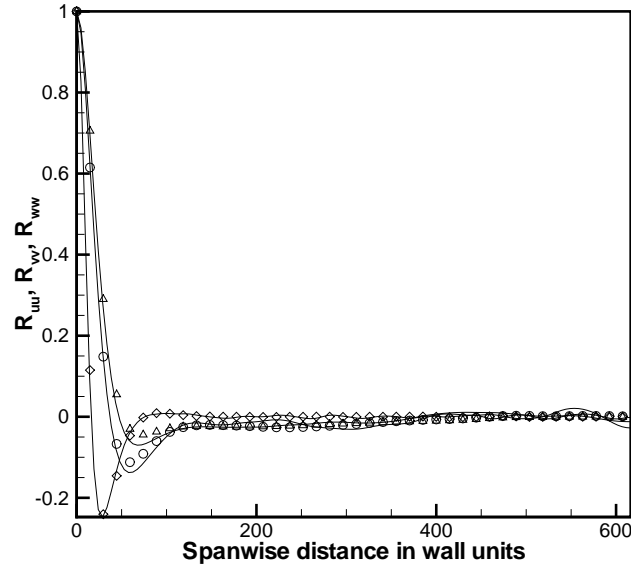


(b)

Figure 3.5: a) Two-point velocity correlation R_{uu} (circle), R_{vv} (triangles) and R_{ww} (gradient) at $z^+ = 10$, $Re_\tau = 360$. The solid lines represent the values of R_{uu} , R_{vv} , R_{ww} from HS; b) Two-point velocity correlation R_{uu} (circle), R_{vv} (triangles) and R_{ww} (gradient) at $z^+ = 10$, $Re_\tau = 395$. The solid lines represent the values of R_{uu} , R_{vv} , R_{ww} from MKM;



(a)



(b)

Figure 3.6: a) Two-point velocity correlation R_{uu} (circles), R_{vv} (triangles) and R_{ww} (gradients) at $z^+ = 10$, $Re_\tau = 360$. The solid lines represent the values of R_{uu} , R_{vv} , R_{ww} from HS; b) Two-point velocity correlation R_{uu} (circles), R_{vv} (triangles) and R_{ww} (gradients) at $z^+ = 10$, $Re_\tau = 395$. The solid lines represent the values of R_{uu} , R_{vv} , R_{ww} from MKM;

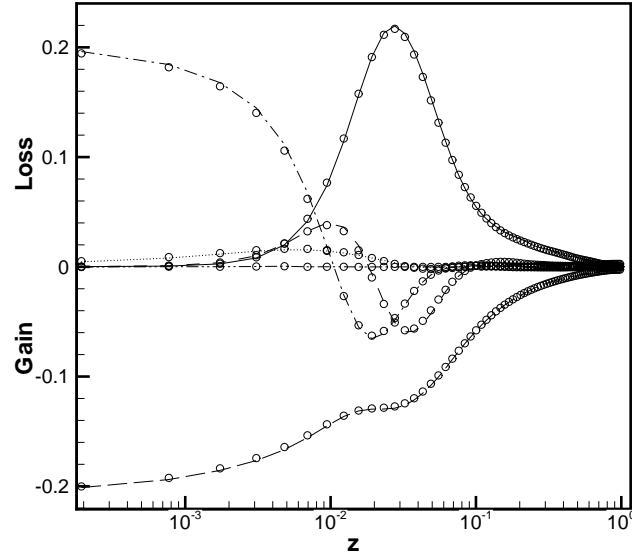


Figure 3.7: Terms in the budgets of turbulent kinetic energy, P (solid line), T (dashed line), D (dash-dotted line), Π (dotted line), ε (long dash-line), Σ (dash-dotted-dotted line). The line with a circles represent the values of the budgets of TKE from HS, $Re_\tau = 360$.

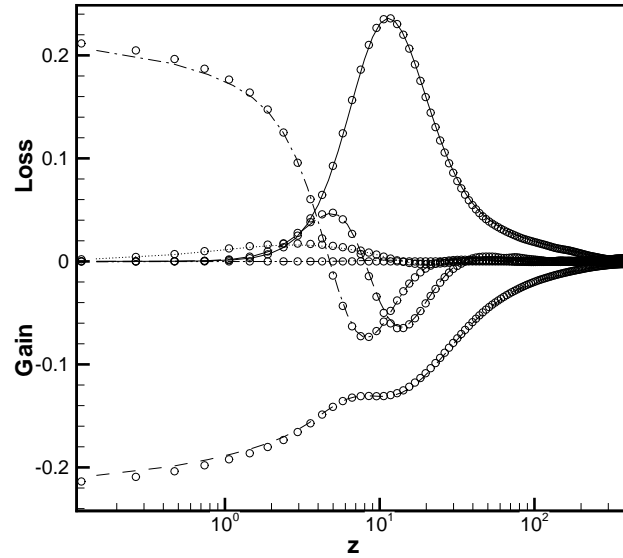


Figure 3.8: Terms in the budgets of turbulent kinetic energy, P (solid line), T (dashed line), D (dash-dotted line), Π (dotted line), ε (long dash-line), Σ (dash-dotted-dotted line). The line with a circles represent the values of the budgets of TKE from MKM, $Re_\tau = 395$.

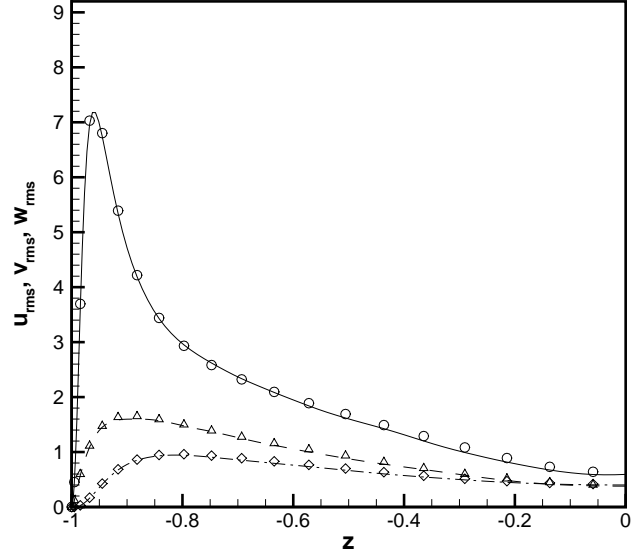


Figure 3.9: Turbulent intensity u_{rms} (solid line), v_{rms} (dashed line) and w_{rms} (dash-dotted line); $Re_\tau = 360$. The line with a circles, deltas and diamonds represent the values of u_{rms} , v_{rms} and w_{rms} from HS $Re_\tau = 360$.

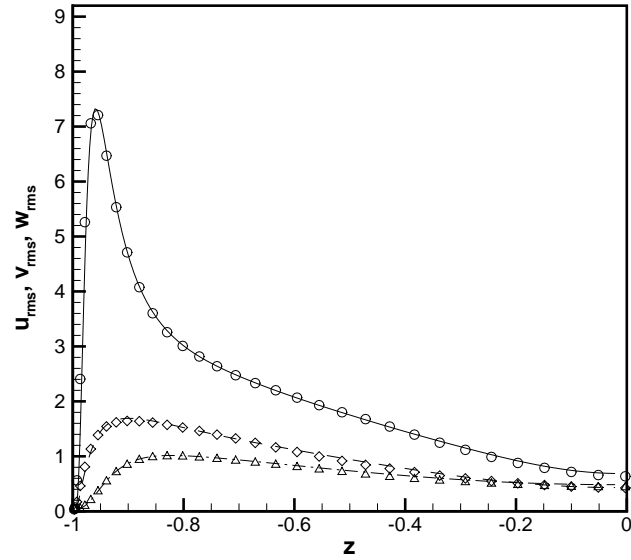


Figure 3.10: Turbulent intensity u_{rms} (solid line), v_{rms} (dashed line) and w_{rms} (dash-dotted line); $Re_\tau = 395$. The line with a circles, deltas and diamonds represent the values of u_{rms} , v_{rms} and w_{rms} from MKM $Re_\tau = 395$.

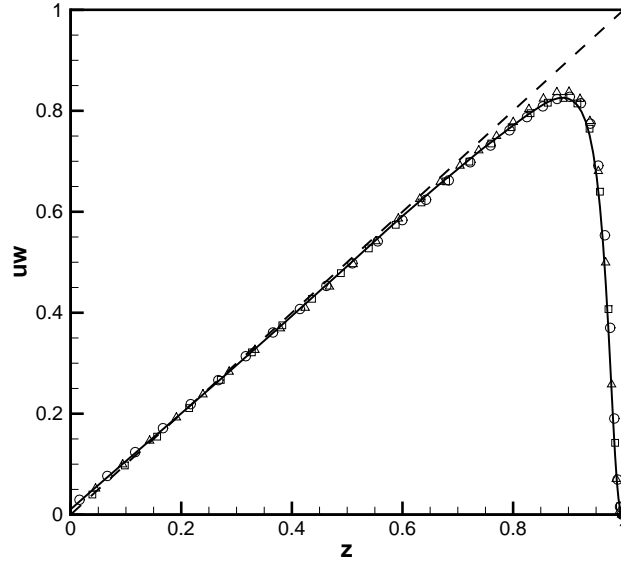


Figure 3.11: Reynolds stress distributions across the channel: Present (solid line), HS (delta) for $Re_\tau = 360$ and present (circle), MKM (diamond) for $Re_\tau = 395$

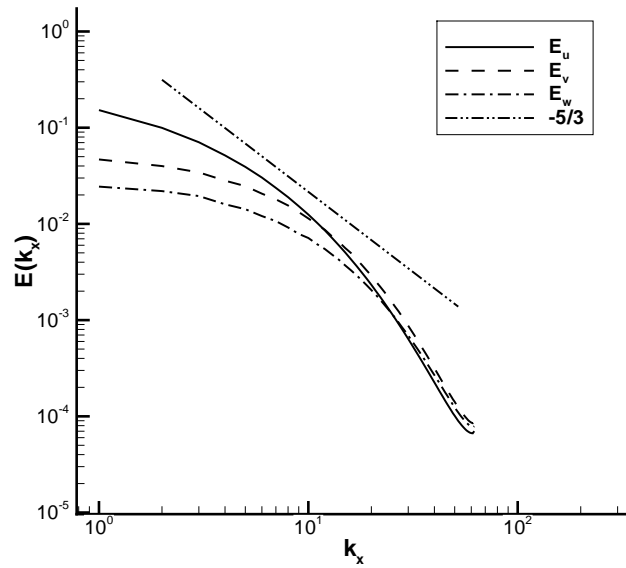


Figure 3.12: Energy spectra $E(k_x)$ integrated over wall-normal direction, $Re_\tau = 360$.

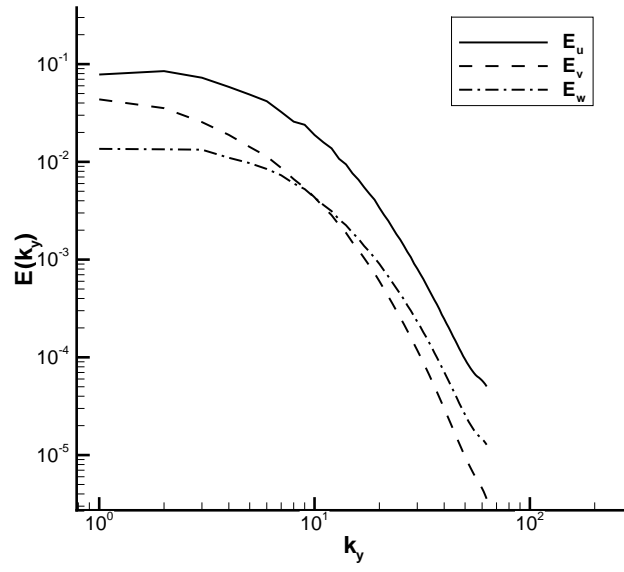


Figure 3.13: Energy spectra $E(k_y)$ integrated over wall-normal direction, $Re_\tau = 360$.

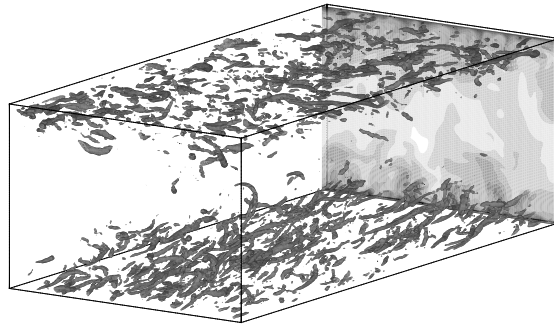


Figure 3.14: Contours of vorticity ω_x .

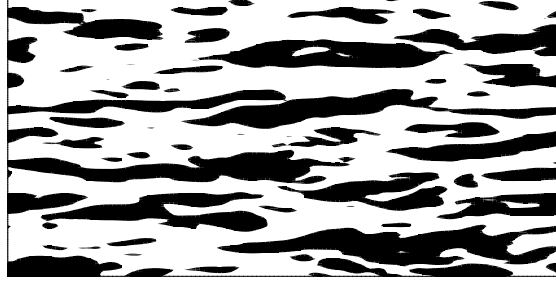


Figure 3.15: Contour of streamwise velocity in wall parallel plane for a wall distance of $z^+ = 5.6$ from the top of the channel. Low-speed streaks (black).

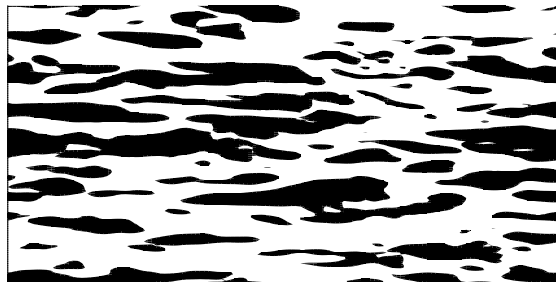


Figure 3.16: Contour of streamwise velocity in wall parallel plane for a wall distance of $z^+ = 5.6$ from the bottom of the channel. Low-speed streaks (black).

4 Calculation of the master modes

This chapter contains a definition of the master-mode set of a numerical solution, which is somewhat different from the master-modes of chapter 2. We will also describe the method used in this work to find the minimum size of master-mode set. The chapter concludes with verification of the master-slave code.

4.1 Master-mode set of a numerical solution

Definition.

In DNS the solution is obtained by marching in time with discrete time steps. At each step the solution can be represented as

$$\mathbf{u}_i(\mathbf{x}) = \sum_{n=1}^S \hat{\mathbf{u}}_{in} \boldsymbol{\phi}_n(\mathbf{x}),$$

where the subscript i corresponds to the solution at time t_i , and $\boldsymbol{\phi}_n(\mathbf{x})$ is a given set of functions. Depending on the particular method, this set of functions can be a part of a full basis, as is typical for Galerkin methods (as in the particular numerical method used in the present work) or just an element of some interpolation formula, as in finite-difference methods based on a control volume approach. Each term in this sum is a mode, and $\hat{\mathbf{u}}_{in}$ is the amplitude of the mode n at the step i . One time step can be described by the formula

$$\hat{\mathbf{u}}_{i+1,n} = D_n(\hat{\mathbf{u}}_{i,1}, \hat{\mathbf{u}}_{i,2}, \dots, \hat{\mathbf{u}}_{i,S}), \quad n = 1, \dots, S, \quad (4.1)$$

where the functions D_n depend on the particular numerical method. (Note that we consider the case when the boundary conditions and body forces are independent of time so that functions D_n are independent of i .) Let $\hat{\mathbf{u}}_{in}, i = 1, 2, \dots$ be a numerical solution, that satisfies (4.1). For a given selection $n = m_1, m_2, \dots, m_K$ of the mode

numbers consider a sequence $\{\mathbf{v}_i(\mathbf{x})\}$:

$$\mathbf{v}_i(\mathbf{x}) = \sum_{n=1}^S \hat{\mathbf{v}}_{i,n} \phi_n(\mathbf{x})$$

such that

$$\hat{\mathbf{v}}_{i+1,n} = \begin{cases} \hat{\mathbf{u}}_{i+1,m_j} & n = m_j, \quad j = 1, \dots, K, \\ D_n(\mathbf{v}_{i,1}, \mathbf{v}_{i,2}, \dots, \mathbf{v}_{i,K}), & n \neq m_j, \quad j = 1, \dots, K \end{cases}$$

In other words, values of $\hat{\mathbf{v}}_{i+1,n}$ are obtained with the time-marching formula (4.1) applied to $\hat{\mathbf{v}}_{i+1,n}$ if they do not belong to the set of modes in question and are taken to be equal to the corresponding modes of the numerical solution otherwise.

If for any $\mathbf{v}_1(\mathbf{x})$

$$\|\mathbf{v}_i(\mathbf{x}) - \mathbf{u}_i(\mathbf{x})\| \rightarrow 0 \quad \text{as} \quad i \rightarrow \infty \quad (4.2)$$

then we will call the set M of modes with $n = m_1, m_2, \dots, m_K$ the master-mode set of the numerical solution $\mathbf{u}_i(\mathbf{x})$. It should be noted that the sequence $\mathbf{v}_i(\mathbf{x})$ does not approximate a solution to the Navier-Stokes equations, in contrast to (2.5) where \mathbf{u}_A and \mathbf{u}_B are both solutions of the Navier-Stokes equations. It also should be noted that the selection $n = m_1, m_2, \dots, m_K$ giving a master-mode set for one solution does not necessarily give a master-mode set for all other possible solutions of the same problem but with different initial conditions.

There is always a trivial master-mode set including all the modes of the numerical calculation. In this case $K = S$. The natural goal, however, is to find master-mode sets with as small a K as possible. It well may be that the minimal master-mode set is not unique: the property (4.2) is the property of the mode selection and not of individual modes. For this reason we avoid using the term “master mode” in the rest of the thesis.

4.2 Master code and slave code

For any given set M of modes one can check whether it is a master-mode set. The method of checking consists in simultaneously running two DNS codes implementing the Galerkin method. One code, which can be called the master code, is just a standard DNS code. Another, the slave code, is an exact copy of the master code except that at each time step the amplitudes of a subset M of modes are replaced by their values calculated by the master code. If the initial conditions for both codes are identical, the entire master and slave solutions will be identical, too. If the initial conditions are different, then the slave solution will tend to the master solution only if the subset M of modes fed in from the master code is a master-mode set. Otherwise, the solutions will deviate. This approach was used by Olson & Titi [1] in the case of forced 2D double-periodic flow and proved to be highly efficient.

4.3 Code verification.

We have already described the validation of our basic DNS code in section 3.5. In this section we will describe the further verification of the modified code. To this end we first verify the basic code by introducing a body force, as described below and then use the basic code to generate verification solutions for the master-slave code.

4.3.1 Verification of the basic code.

In order to be able to check the basic DNS code we slightly modified the code so that it solves the Navier-Stokes equations with the body force,

$$\frac{\partial \mathbf{u}}{\partial t} = \mathbf{u} \times \boldsymbol{\omega} - \nabla q - \delta_{li} \frac{\partial \bar{P}}{\partial x} + \frac{1}{Re_\tau} \nabla^2 \mathbf{u} + \mathbf{F}. \quad (4.1.1)$$

We took the following velocity field:

$$u = \frac{40(1 - z^2)}{2}, \quad (4.1.2)$$

$$v = -12(1 - z^2) \sin\left(\frac{4\pi y}{3}\right) z^2 \sin(t) + 3(1 - z^2)^2 \sin\left(\frac{4\pi y}{3}\right) \sin(t), \quad (4.1.2)$$

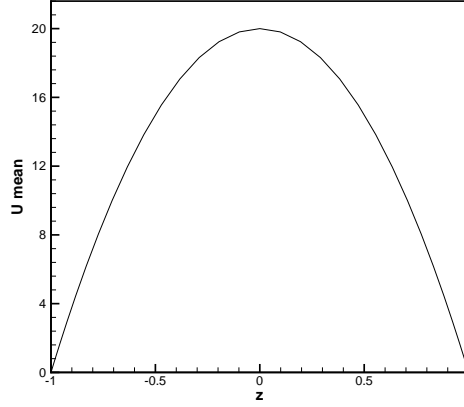
$$w = -4 \cos\left(\frac{4\pi y}{3}\right) \pi (z + z^5 - 2z^3) \sin(t). \quad (4.1.3)$$

and computed the corresponding body force terms (F_x, F_y, F_z) analytically with a condition that divergence of the body force should be equal to 0 (otherwise the DNS code computes incorrectly). All analytic calculations for finding the corresponding body force were done with the help of the commercial software MAPLE:

$$F_x = 4 \cos\left(\frac{4\pi y}{3}\right) \pi z^2 (1 + z^4 - 2z^2) \sin(t) Re_\tau$$

$$\begin{aligned} F_y = & \frac{-1}{98304} (17472 \sin\left(\frac{4\pi y}{3}\right) z^2 \cos(t) \pi^7 Re_\tau - 35344 \sin\left(\frac{4\pi y}{3}\right) \sin(t) \pi^7 - \\ & 14760 \sin\left(\frac{4\pi y}{3}\right) z^4 \cos(t) \pi^7 Re_\tau - 5288 \sin\left(\frac{4\pi y}{3}\right) \sin(t) \pi^9 - 29412 \sin\left(\frac{4\pi y}{3}\right) \cos(t) \pi^7 Re_\tau + \\ & 31428 \sin\left(\frac{4\pi y}{3}\right) \sin(t) \pi^9 z^2 - 26440 \sin\left(\frac{4\pi y}{3}\right) \sin(t) \pi^9 z^4 + 176920 \sin\left(\frac{4\pi y}{3}\right) \sin(t) \pi^7 z^2 + \\ & 932175 Re_\tau \cos\left(\frac{4\pi y}{3}\right) \sin\left(\frac{4\pi y}{3}\right) + 131072 Re_\tau \pi^8 e^{-8/3\pi z} + \\ & 1119744 Re_\tau \cos\left(\frac{4\pi y}{3}\right) \sin\left(\frac{4\pi y}{3}\right) \pi^4 + 46640 Re_\tau \sin\left(\frac{4\pi y}{3}\right) \cos\left(\frac{4\pi y}{3}\right) \pi^6 z^6) \end{aligned}$$

$$\begin{aligned} F_z = & \frac{-1}{73728} (-2280 Re_\tau \pi^4 z^3 - 794 z^5 \pi^6 Re_\tau + 292 \cos\left(\frac{4\pi y}{3}\right) \pi^7 z \cos(t) Re_\tau + \\ & 2912 \cos\left(\frac{4\pi y}{3}\right) \pi^7 z^5 \cos(t) Re_\tau - 58924 \cos\left(\frac{4\pi y}{3}\right) \pi^7 z^3 \cos(t) Re_\tau + \\ & 52288 \cos\left(\frac{4\pi y}{3}\right) \pi^9 \sin(t) z + 5288 \cos\left(\frac{4\pi y}{3}\right) \pi^9 \sin(t) z^5 - 1076 \cos\left(\frac{4\pi y}{3}\right) \pi^9 \sin(t) z^3 - \\ & 58940 \cos\left(\frac{4\pi y}{3}\right) \pi^7 \sin(t) z^3 + 354 \cos\left(\frac{4\pi y}{3}\right) \pi^7 \sin(t) z - 14756 \pi^6 Re_\tau + \\ & 19608 Re_\tau \pi^7 \sin\left(\frac{4\pi y}{3}\right) \cos\left(\frac{4\pi y}{3}\right) e^{8/3\pi z} \cos(t)^2 - 19608 Re_\tau \pi^7 \sin\left(\frac{4\pi y}{3}\right) \cos\left(\frac{4\pi y}{3}\right) e^{8/3\pi z} + \\ & 78080 Re_\tau \pi^4 z^5 \cos(t)^2 \cos\left(\frac{4\pi y}{3}\right)^2 - 37360 Re_\tau \pi^2 z \cos(t)^2 \cos\left(\frac{4\pi y}{3}\right)^2 + \\ & 55296 Re_\tau \pi^5 e^{-8/3\pi z} \cos(t)^2 \cos\left(\frac{4\pi y}{3}\right)^2 + 19608 Re_\tau \pi^7 \sin\left(\frac{4\pi y}{3}\right) \cos\left(\frac{4\pi y}{3}\right) e^{-8/3\pi z} - \\ & 19608 Re_\tau \pi^7 \sin\left(\frac{4\pi y}{3}\right) \cos\left(\frac{4\pi y}{3}\right) e^{-8/3\pi z} \cos(t)^2) \end{aligned}$$

Figure 4.1: The mean flow $U(z)$.

This body force was substituted into the code, calculations performed and the results compared with (4.1.2)-(4.1.4). For the verification we took the following computational conditions. The computational domain is a rectangular box of the dimension $L_x = 5.0, L_y = 5.0, L_z = 2.0$. The numbers of discretization points are, respectively, $N_x = 32, N_y = 32$ and $N_z = 32$ in the x, y and z directions. The fluid domain is periodic along the streamwise (x) and the spanwise (y) directions and (z) is the wall-normal direction, with the channel walls at $z = \pm 1$. The boundary conditions are impermeability and no-slip at the walls and hence are given as $u(z = \pm 1) = 0, v(z = \pm 1) = 0, w(z = \pm 1) = 0$. Note that the velocity field (4.1.1)-(4.1.3) satisfies these conditions. The comparison between analytical and numerical solutions of the Navier-Stokes equations is presented in Figures 4.2 as the L_2 norm error of u and w .

$$\epsilon = \|u_{\text{numerical}} - u_{\text{analytical}}\|_{L_2} \quad (6.1)$$

The difference between analytical and numerical solutions of the Navier-Stokes is small. To investigate the influence of the grid size on the accuracy of the numerical solution we compared the v velocity error on two different grids of the size $16 \times 16 \times 16$ and $32 \times 32 \times 32$. Grid refinement decreased the error by approximately 55%, figure 4.3. It can be concluded that DNS code works correctly.

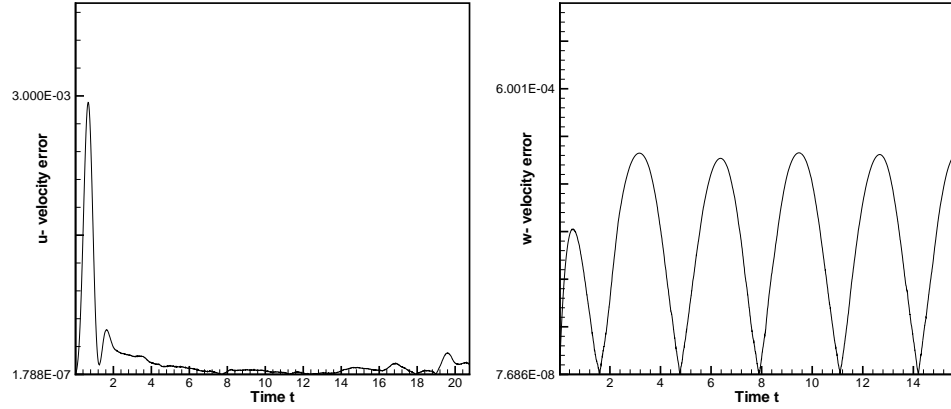


Figure 4.2: Comparison of u and w -velocity error between the analytical and numerical solutions

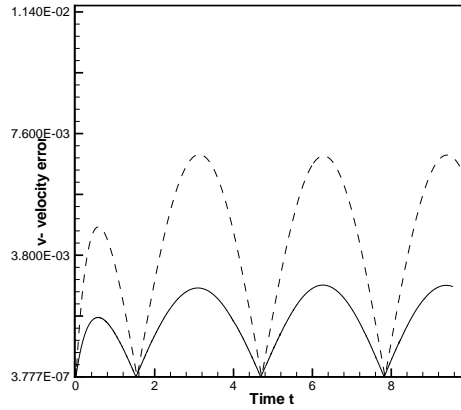


Figure 4.3: Comparison of v -velocity errors for grid size $16 \times 16 \times 16$ (dashed line) and $32 \times 32 \times 32$ (solid line).

4.3.2 Verification of the master-slave code

In order to estimate the number of master modes in a turbulent channel flow we use the DNS code which was checked as described above. The methodology of finding the minimal number of master modes involves two DNS codes: the master code and a slave code. At each time step the amplitudes of N trial modes of the slave code are replaced by their values calculated by the master code.

So as to check that the master-slave DNS code works correctly we shall calculate separately two problems with different initial conditions (A) and (B) on the original and already verified DNS code.

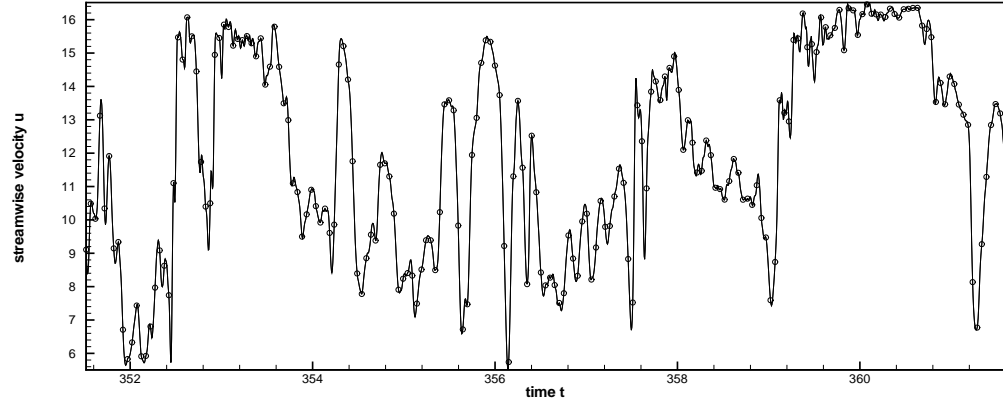


Figure 4.4: Streamwise velocity component u_A (solid line) and $u_{A-master}$ (circles) at a point on the central plane of the channel.

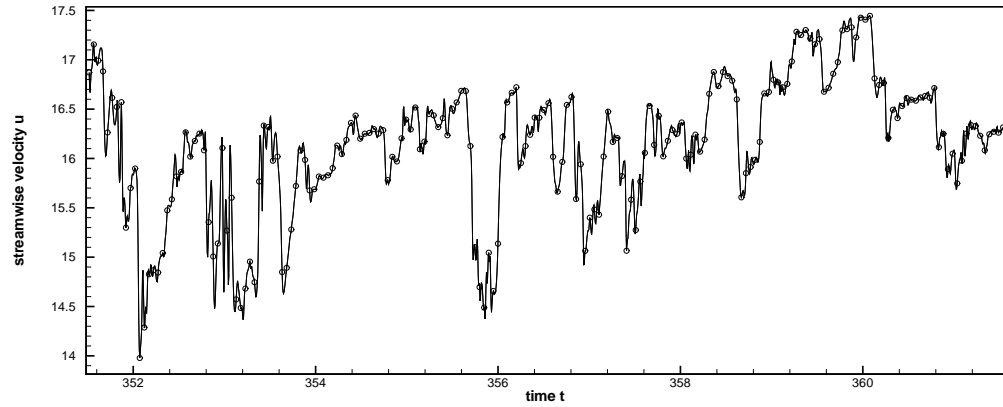


Figure 4.5: Streamwise velocity component u_B (solid line) and $u_{B-master}$ (circles) at a point on the central plane of the channel.

The calculated streamwise velocity component $u_A(x_0, y_0, z_0)$ (for the initial conditions (A)) and streamwise velocity component $u_B(x_0, y_0, z_0)$ (for the initial conditions (B)) at a point on the central plane of the channel are presented in Figure 4.4-4.5 as a function of time (solid line). Then we solve the same two problems (A, B) with the help of the master-slave code bearing in mind that in this calculation we do not do replace the amplitudes at all ($N = 0$). Then the master-slave code simply calculates two solutions of the Navier-Stokes equations simultaneously. The result of this is presented in Figure 4.4-4.5 (circles) as a function of time. The calculated streamwise velocity component $u_{A-master}(x_0, y_0, z_0)$ (for the initial conditions (A) which was obtained by master code) and streamwise velocity component

$u_{B-slave}(x_0, y_0, z_0)$ (for the initial conditions (B) which was obtained by slave code) at a point on the central plane of the channel are equal to u_A and u_B . As we got $u_A = u_{A-master}$ and $u_B = u_{B-slave}$ we come to a conclusion that two Navier-Stokes equations are solved by the master-slave code correctly. In this case we can stress that the master-slave code is solving two Navier-Stokes equations separately from each other. Also we checked the situation when at each time step the amplitudes of all modes of the slave code were replaced by their values calculated by the master code. The results was that the solution were identical. Checking the code with $N > 0$ is more difficult. We have to rely on the simplicity of the modification from $N = 0$ to $N > 0$, and on the qualitatively correct behavior of the solution with $N > 0$.

4.4 Mode ordering

The Sandham and Howard [6] code uses Fourier series expansion in the wall-parallel directions and Chebyshev series in the wall-normal direction, so that the solution is represented in the form

$$\mathbf{u}(x, t) = \sum_{k_x=-N_1/2}^{N_1/2} \sum_{k_y=-N_2/2}^{N_2/2} \sum_{k_z=0}^{N_3-1} \hat{\mathbf{u}}_{k_x, k_y, k_z}(t) e^{2\pi i(k_x x/L_x + k_y y/L_y)} T_{k_z}(z), \quad (4.3)$$

where $T_{k_z}(z)$ is a Chebyshev polynomial of k_z order and $\hat{\mathbf{u}}_{k_x, k_y, k_z}(t)$ are complex-valued amplitudes of the modes.

Finding the smallest master-mode set by trial-and-error is very inefficient. If modes are ordered, a far more efficient dichotomy algorithm (method of division in halves) can be used, or more simply a set of possible sizes of the master-mode set can be tried. Ordering the modes by the squared magnitude $k_x^2 + k_y^2 + k_z^2$ of their wavenumber is non-physical, since this method does not take into account the anisotropy of the flow and since k_z , being the order of the Chebyshev polynomial, should not actually be directly compared with k_x and k_y . However, since this method is very straightforward it was tried.

A more physical approach could be based on the averaged energy content of the modes. However, the modes (4.3) are not orthogonal with respect to the standard energy norm. Instead, we introduce a Chebyshev-weighted energy norm:

$$\|\mathbf{u}\|_C^2 = \iiint \frac{|\mathbf{u}|^2}{\sqrt{1-z^2}} dx dy dz.$$

This norm of the solution is equal to the sum of the norms of the modes, and hence the modes can be ordered by the time-averaged values of their amplitudes $\langle |\hat{\mathbf{u}}_{k_x, k_y, k_z}|^2 \rangle$. The calculations were run for a certain period of time and statistics for calculating these averages was collected. Much longer calculation would be required for obtaining accurate values of the averages, but for our purpose high accuracy is not required. The modes were then ordered by $\langle |\hat{\mathbf{u}}_{k_x, k_y, k_z}|^2 \rangle$ with the assumption that more energetic modes are more likely to belong to the master-mode

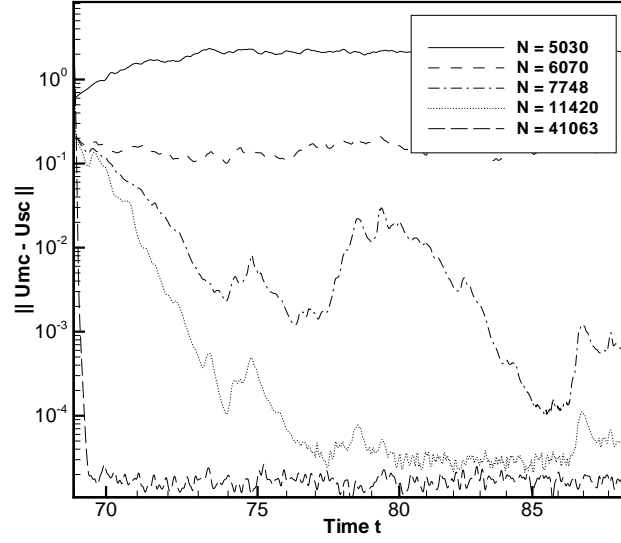


Figure 4.6: The evolution of $\|u_{mc} - u_{sc}\|_{L_2}$, the modes were ordered by the sum of their wave-numbers, $Re_\tau = 180$.

set.

Schmidtman, Feudel & Seehafer [50, 51] in their work on non-linear Galerkin methods suggested that ordering the modes by their enstrophy content may be more efficient, and ordering the modes by their weighted enstrophy was also attempted in the present study. Calculations were performed for $Re_\tau = 180$ in the box of the dimensions $L_x \times L_y \times L_z = 4 \times 3 \times 2$. Figures 4.6-4.8 illustrate the evolution of $\|u_{mc} - u_{sc}\|_{L_2}$ (where u_{mc} - velocity field of master code and u_{sc} is velocity field of slave code). These figures allow an estimate to be made of the minimal number K of master modes which guarantee that u_{sc} will converge to u_{mc} as $t \rightarrow \infty$.

One can see that the minimal size of the master-mode set K exceeds 7748 if the modes are ordered by the wavenumber (see Figure 4.6), that $3800 < K < 4169$ for enstrophy-based ordering (see Figure 4.8), and that $2800 < K < 2900$ for energy-based ordering (see Figure 4.7). The energy-based ordering was then used in all other calculations.

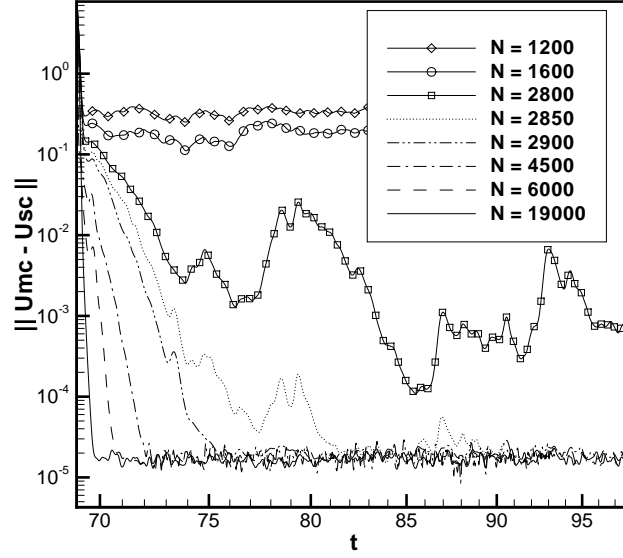


Figure 4.7: The evolution of $\|u_{mc} - u_{sc}\|_{L_2}$, the modes were ordered by the energy-based method, $Re_\tau = 180$.

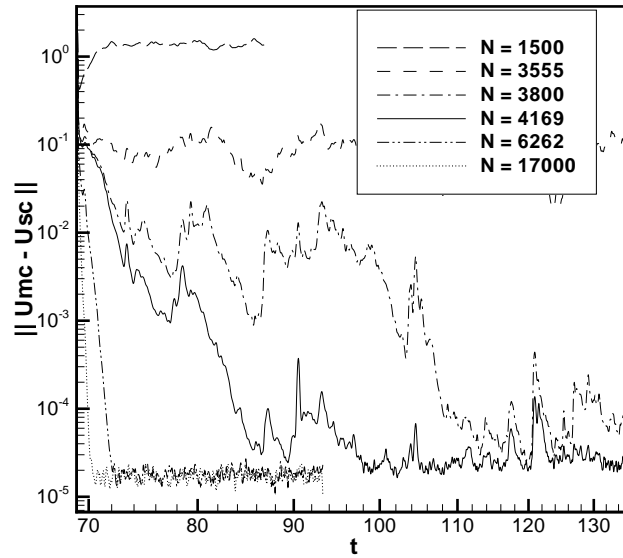


Figure 4.8: The evolution of $\|u_{mc} - u_{sc}\|_{L_2}$, the modes were ordered by the enstrophy-based method, $Re_\tau = 180$.

5 Properties of master-mode set

This chapter is divided into several sections: the first deals with estimating the number of master modes in a turbulent flow in a channel with Reynolds number $Re_\tau = 85$ and comparing it with the dimension of the Navier-Stokes attractor at $Re_\tau = 80$ (Keefe *et al.* [7]); the second deals with DNS simulation at $Re_\tau = 360$; third section explores the organized structures of developed turbulent flow calculated from the master-mode set only and from the slave modes. In particular, we are interested in what kind of organized structures appear in the flow calculated with the help of master modes only.

5.1 Master-mode set size

5.1.1 Size of the master-mode set for $Re_\tau = 85$ and the dimension of the attractor

While the minimal size of the master-mode set is not necessarily equal to the dimension of the attractor of the turbulent flow, it seems intuitively probable that they should be close. The only calculation of the dimension of the attractor for channel flow was performed by Keefe *et al.* [7]. They considered a channel flow in the box $1.6\pi \times 1.6\pi \times 2$ at $Re_\tau = 80$. The code used in the present study gives only transitional solutions at this Re_τ , hence $Re_\tau = 85$ was used, with the grid size $32 \times 32 \times 32$ which is the same as in Keefe *et al.* [7]. In this case a turbulent flow was observed, as is evidenced by figure 5.1, which compares the calculated velocity profile with the law of the wall $u^+ = z^+$ and the logarithmic law $u^+ = 2.5 \log y^+ + 5.5$.

The figure 5.2 shows the calculated turbulent intensities u_{rms} , v_{rms} , w_{rms} . Unfortunately, in this low-Reynolds number range there are no experimental data to compare with. One can, however, see, that the calculated flow is turbulent.

Figure 5.3 shows the evolution of $\|u_{mc} - u_{sc}\|_{L_2}$, where u_{mc} is the solution of master code and u_{sc} is accordingly the solution of slave code. One can see the number

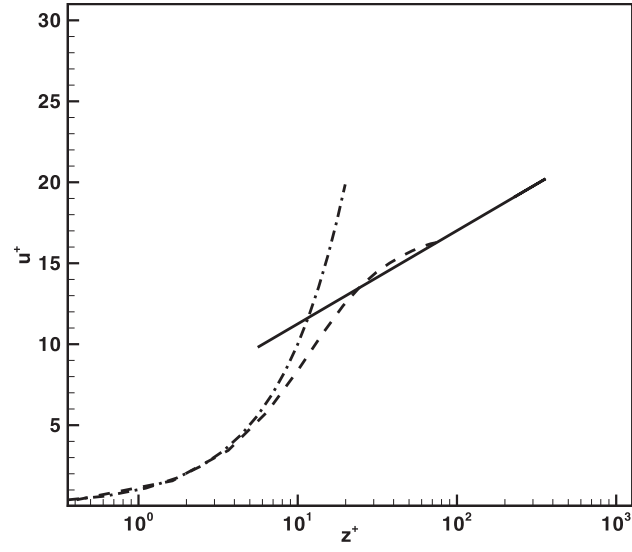


Figure 5.1: Mean velocity profile in wall coordinates $Re_\tau = 85$ (dashed line), $u^+ = z^+$ (dash-dotted line) and $u^+ = 2.5 \log y^+ + 5.5$ (solid line)

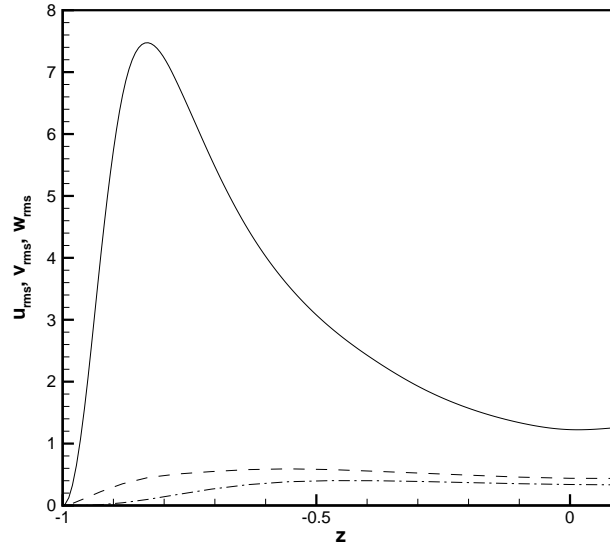
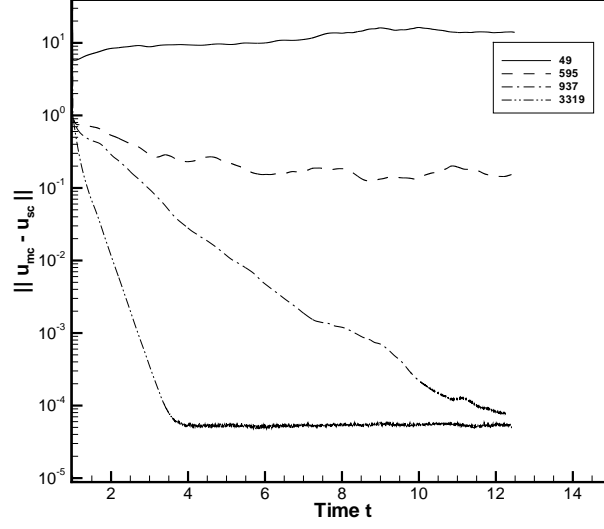


Figure 5.2: Turbulent intensity u_{rms} (solid line), v_{rms} (dashed line) and w_{rms} (dash-dotted line); $Re_\tau = 85$.

Figure 5.3: The evolution of $\|u_{mc} - u_{sc}\|_{L_2}$, $Re_\tau = 85$

of master modes for $Re_\tau=85$ on a spatial-domain with streamwise and spanwise periods of 1.6π is ($595 < N_{min} < 937$). This can be compared with Keefe *et. al* [7], who estimated the fractal dimension as $D_\lambda=780$ for $Re_\tau=80$. Therefore for this case the minimal size of the master-mode set and the dimension of the attractor are close.

5.1.2 Size of the master-mode set for $Re_\tau = 360$

In this section calculations with $Re_\tau = 360$ are described in detail. The computational box size was $L_x \times L_y \times L_z = 6 \times 3 \times 2$. The numbers of discretization points were, respectively, $N_x = 128$, $N_y = 128$ and $N_z = 160$ in the x , y and z directions.

The initial condition for velocity field of master code (u_{mc}) is the fully developed turbulent channel flow. We represent the velocity field from the master code u_{mc} as a sum of master modes and slave modes

$$u_{mc} = u_{(mc \text{ master-modes})} + u_{(mc \text{ slave-modes})}$$

and velocity field of the slave code u_{sc} as

$$u_{sc} = u_{(sc \text{ master-modes})} + u_{(sc \text{ slave-modes})}$$

The master velocity field $u_{(mc \text{ master-modes})}$ consists of those modes which were chosen by one of the methods described in the section 4.4. The initial condition for velocity field of the slave code was chosen as:

$$u_{sc} = u_{(mc \text{ master-modes})} + u_{(mc \text{ slave-modes})} \cdot \Delta\mathcal{E}$$

where $\Delta\mathcal{E} \neq 1$ ensures a difference in the velocity field between the master code and the slave code. Alternative ways of prescribing the initial conditions for the slave code were tried and gave similar results.

The evolution of the L_2 norm of the difference between the velocity field of master code (u_{mc}) and the velocity field of slave code (u_{sc}) obtained with the different number of master modes is presented in Figure 5.4. Selection of master modes was done by the time-averaged value of the mode amplitude; the method is described in the section 4.4. Our computational results consist of six sets of calculations. For our first set we took 18365 master modes, in the second set the number of master modes was 22879, for third set $N=29716$, then $N=34601$, in the fifth set number of master modes was 41069 and for the last one it was $N=63448$.

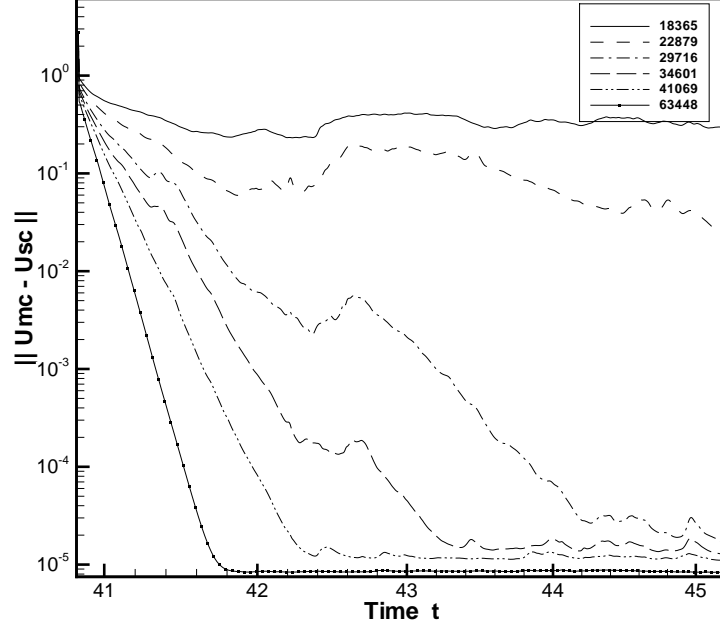


Figure 5.4: The evolution of $\|u_{mc} - u_{sc}\|_{L_2}$, energy-based method of ordering the modes, $Re_\tau = 360$.

The numerical simulations show that convergence of the master and slave solution actually occurs for a number of master modes between $22879 < N_{min} < 29716$. It can be seen in Figure 5.4 that for the number of master modes less than about 22879 the master and slave solutions diverge while for the number of master modes about 30000 they converge. For comparison, the total number of modes used in the calculation and needed for obtaining a resolved solution is $128 \times 128 \times 160 = 2621440$. Therefore, in this case the minimal size of the master-mode set is about 1% of the minimal number of modes needed to resolve the flow.

We also checked that increasing the number of modes used in the numerical calculations above the necessary minimum does not affect the size of the minimal master-mode set. Namely, calculations for $Re_\tau = 360$, $Lx = 6$, $Ly = 3$ were performed with an increased number of modes $256 \times 256 \times 160$. The minimal size of the master-mode set was found to be about 29000, which is the same as the minimal size of the master-mode set for the grid $128 \times 128 \times 160$.

Another simulation was performed for $Re_\tau = 360$ and for the computational box

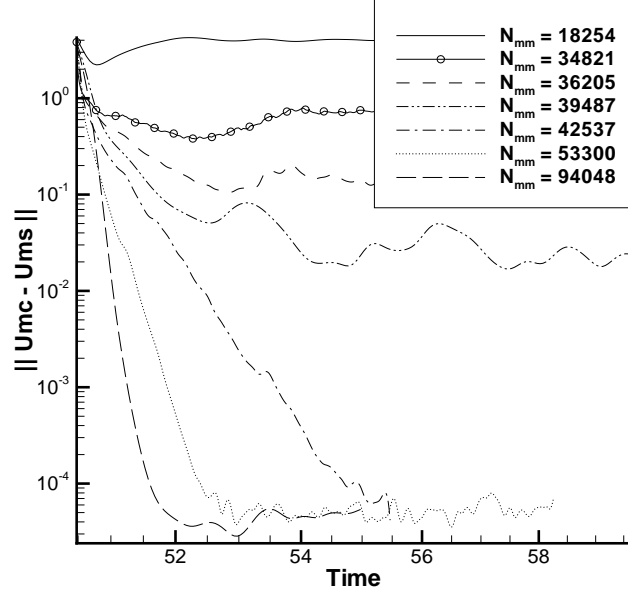


Figure 5.5: The evolution of $\|u_{mc} - u_{sc}\|_{L_2}$, enstrophy-based method of ordering the modes, $Re_\tau = 360$.

size $14 \times 2 \times 9$ (mean flow \times wall-normal \times lateral) with the energy-based method of ordering the modes. The numbers of discretization points were, respectively, $N_x = 512, N_y = 512$ and $N_z = 160$ in the x, y and z directions. The numerical simulation gave $161336 < N_{min} < 225900$.

Also we performed another simulation for $Re_\tau = 360$, $L_x \times L_y \times L_z = 6 \times 3 \times 2$ with the grid size, respectively, $N_x = 128, N_y = 128$ and $N_z = 160$ in the x, y and z directions, using an enstrophy-based method of ordering the modes, see figure 5.5.

5.2 Convergence rate

The rate at which the difference between the master solution and the slave solution tends to zero can be estimated in the following way. Let N_{mm} be the number of the modes whose amplitudes are being passed from the master to the slave code. When $N_{mm} > N_{min}$, the difference between the master and the slave solution converges exponentially, $\|\mathbf{u}_m - \mathbf{u}_s\| \sim e^{-\alpha t}$ (Olson & Titi [34]). The value of α depends

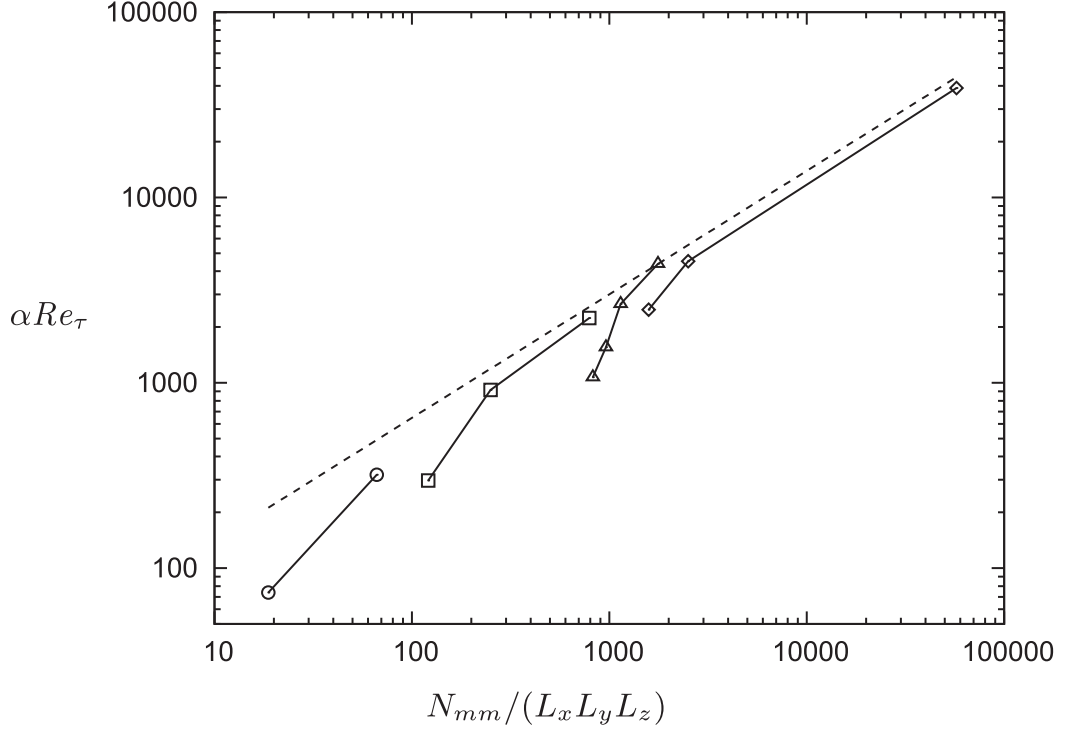


Figure 5.6: Convergence rate, $L_z = 2$: $Re_\tau = 85$, $L_x \times L_y = 5 \times 5$, \circ ; $Re_\tau = 180$, $L_x \times L_y = 4 \times 3$, \square ; $Re_\tau = 360$, $L_x \times L_y = 6 \times 3$, \triangle ; $Re_\tau = 360$, $L_x \times L_y = 14 \times 9$, \diamond .

on N_{mm} . Assuming that the decay is due to viscous effects gives an estimate $\alpha \sim L_m^{-2} Re_\tau^{-1}$, where L_m is the largest characteristic length scale of the slave mode set (non-dimensional quantities corresponding to (3.1) are used throughout). One can assume that L_m is proportional to the cubic root of the volume of the computational box divided by the number of modes: $L_m \approx \text{const}(L_x L_y L_z / N_{mm})^{1/3}$. This gives the formula

$$\alpha = \frac{C}{Re_\tau} \left(\frac{N_{mm}}{L_x L_y L_z} \right)^{2/3} \quad (5.1)$$

It is equivalent to $\alpha^* L_m^{*2} / \nu = \alpha^* (L_x^* L_y^* L_z^* / N_{mm})^{2/3} / \nu = \text{const}$, where $*$ denotes dimensional quantities and ν is the kinematic viscosity. Naturally, as N_{mm} approaches N_{min} , α should tend to zero. This is not reflected by (5.1), which, therefore, can be expected to describe an asymptote approached from below as $N_{mm} \rightarrow \infty$.

Figure 5.6 shows the values of αRe_τ plotted against $N_{mm} / (L_x L_y L_z)$ for all calculated cases together with the line given by (5.1) with $C = 30$. The values of α were

obtained by estimating the slope of the plot of the L_2 norm (that is the square root of the integral of $|\mathbf{u}_m - \mathbf{u}_s|^2$ over the calculation domain) versus time. It appears that (4.4) can indeed be used for rough estimates of the convergence rate at large N_{mm} .

Yoshida *et al.* [3] found that the convergence rate multiplied by the Kolmogorov time scale and plotted versus the cut-off wavenumber multiplied by the Kolmogorov length is independent of the Reynolds number. In a channel flow the energy dissipation rate depends on the distance to the wall. We can, however, introduce an average energy dissipation rate (per unit volume) as $\epsilon = U_{mean}$, where U_{mean} is the mean velocity (note that due to the scaling used in our work the pressure gradient is equal to -1 , and all the quantities are non-dimensional). We then introduce the Kolmogorov time and length scales as $\tau = (\epsilon Re_\tau)^{-1/2}$ and $\eta = (\epsilon Re_\tau^3)^{-1/4}$. In Yoshida *et al.* [3] the number of modes per unit volume corresponding to the cut-off wave number k_a was evaluated as $(4/3)\pi k_a^3 / (2\pi)^3$ while in our case it is $N_{mm} / (L_x L_y L_z)$. Accordingly, we define our cut-off wavenumber as

$$k_a = 2\pi \left(\frac{3N_{mm}}{4\pi L_x L_y L_z} \right)^{1/3} \quad (5.2)$$

Figure 5.7 shows the dependence of $\alpha = \alpha\tau$ on $k_a\eta$. The dash-dotted line is an approximation of the Yoshida *et al.* [3] results. Of course this comparison is only tentative since the channel flow is not isotropic and homogeneous. However, our results at least do not contradict the conclusion made in Yoshida *et al.* [3] that the Kolmogorov-scaled convergence rate is determined by the quantities for the energy dissipation scale rather than the energy containing scale. In large eddy simulation approach the full solution is also divided into large scale and small scale components. Then the large scale motion is simulated numerically with the effect of small scale on large scale described with a subgrid-scale model. If a similarity between the large scale motion in the large eddy simulation approach and master-modes is assumed then from the results for master modes it follows that subgrid scale models should have memory, for example in the form of relaxation relationships. The

above data on the convergence rate can be used to estimate the time constants of these relaxation relationships.

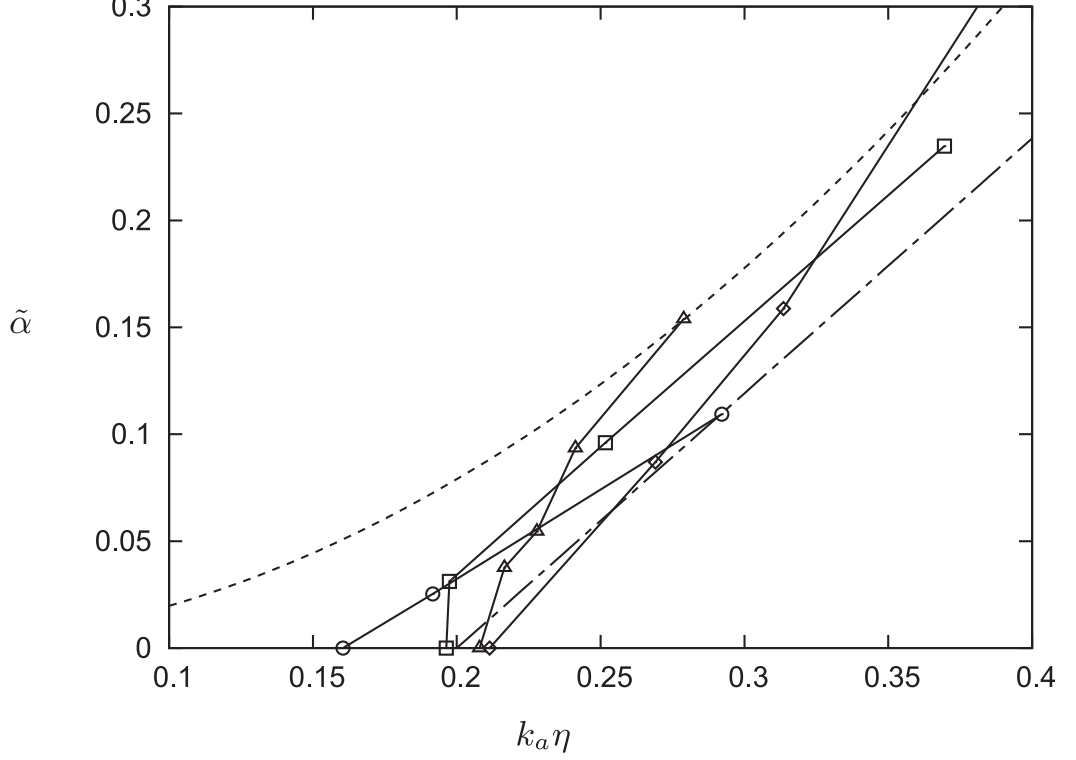


Figure 5.7: The dash-dotted line is an approximation of the Yoshida *et al.* [3] results. Other lines and symbols are the same as in figure 5.6

5.3 Other properties of the master-mode set for $Re_\tau = 360$

The purpose of this section is to explore in detail the properties of the master-mode set for $Re_\tau = 360$, comparing statistics from three different simulations. In the first simulation the flow field was calculated solely from a master-mode set. In this case the modes were ordered by the time-averaged values of their amplitudes $\langle |\hat{\mathbf{u}}_{k_x, k_y, k_z}|^2 \rangle$ (hereafter we refer to this method of ordering as $\langle |\hat{\mathbf{u}}| \rangle$). The flow field for the second simulation was calculated from a master-mode set in which the modes were ordered by their weighted enstrophy $\langle |\hat{\boldsymbol{\omega}}_{k_x, k_y, k_z}|^2 \rangle$ (referred to hereafter as $\langle |\hat{\boldsymbol{\omega}}| \rangle$). The last simulation is the full flow. We will also show statistics calculated from the slave modes of methods $\langle |\hat{\mathbf{u}}| \rangle$ and $\langle |\hat{\boldsymbol{\omega}}| \rangle$. The parameters of these simulations are $Re_\tau =$

360, $L_x \times L_y \times L_z = 6 \times 3 \times 2$ with the grid size, respectively, $N_x = 128$, $N_y = 128$ and $N_z = 160$ in the x , y and z directions.

5.3.1 Mean profiles

Figure 5.9 shows the mean streamwise velocity profile in global coordinates. As would be expected the comparison shows that the mean velocity profiles are accurately approximated by methods $\langle |\hat{\mathbf{u}}| \rangle$ and $\langle |\hat{\Omega}| \rangle$.

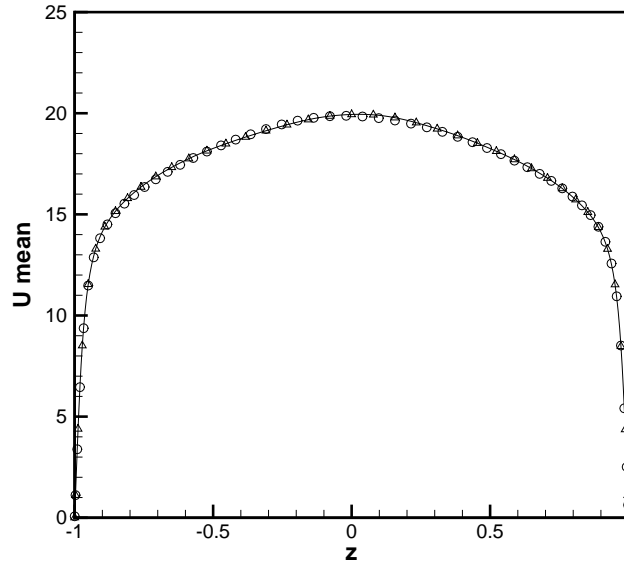
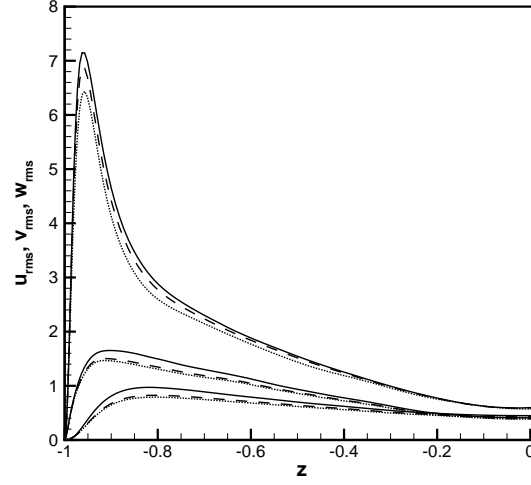


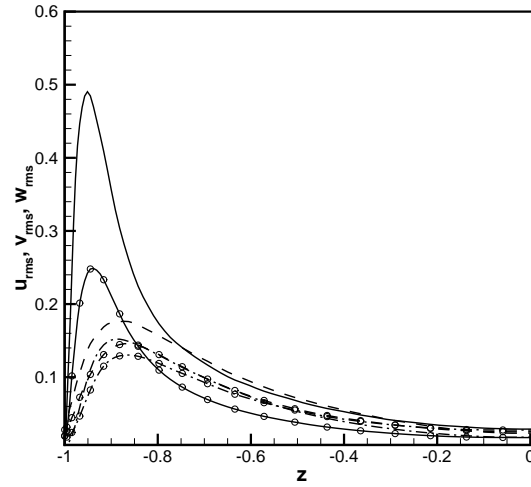
Figure 5.8: Mean velocity profile in wall coordinates, $Re_\tau = 360$, $L_x \times L_y \times L_z = 6 \times 3 \times 2$, $N_x = 128$, $N_y = 128$ and $N_z = 160$, full flow (solid curve); minimal master-mode set ($N_{mm}=29716$) ordered by $\langle |\hat{\mathbf{u}}| \rangle$ Δ ; a minimal master-mode set ($N_{mm}=42537$) ordered by $\langle |\hat{\Omega}| \rangle$ \circ .

Figure 5.9 (a) shows the comparison for the RMS velocity fluctuations for the full flow and for the flow calculated from master-mode set ordered by $\langle |\hat{\mathbf{u}}| \rangle$ and $\langle |\hat{\Omega}| \rangle$ methods, flow showing a very good agreement in the middle of the channel; however, close to the wall the amplitudes of the peaks are slightly different. The u_{rms} calculated from slave-mode set ordered by methods $\langle |\hat{\mathbf{u}}| \rangle$ and $\langle |\hat{\Omega}| \rangle$ are shown in figure 5.9 (b).

The mean turbulent kinetic energy profile vs z is shown in figure 5.10 (a),



(a)



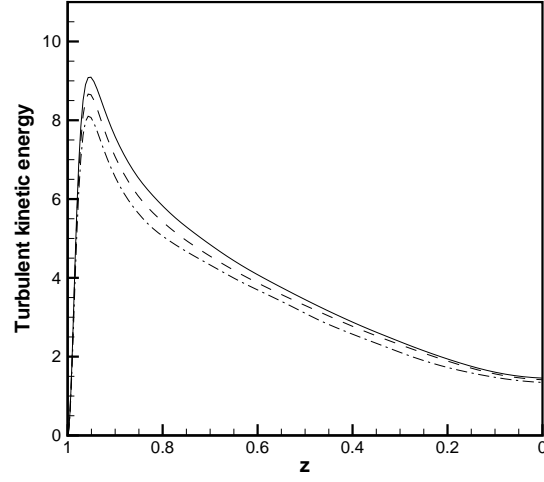
(b)

Figure 5.9: Mean square fluctuation velocity: a) Comparison of turbulent intensity between full flow and flow calculated from the master-mode set, full flow (solid curve), a minimal master-mode set ($N_{mm}=29716$) ordered by $\langle |\hat{\mathbf{u}}| \rangle$ (dotted line) and ($N_{mm}=42537$) $\langle |\hat{\Omega}| \rangle$ (dashed line); b) calculated from slave modes only ordered by $\langle |\hat{\mathbf{u}}| \rangle$ u_{rms} (solid line), v_{rms} (dashed line) and w_{rms} (dash-dotted line), by $\langle |\hat{\Omega}| \rangle$ u_{rms} (solid line with circles), v_{rms} (dashed line with circles) and w_{rms} (dash-dotted line with circles), computational box size is $6 \times 2 \times 3$, $Re_\tau = 360$.

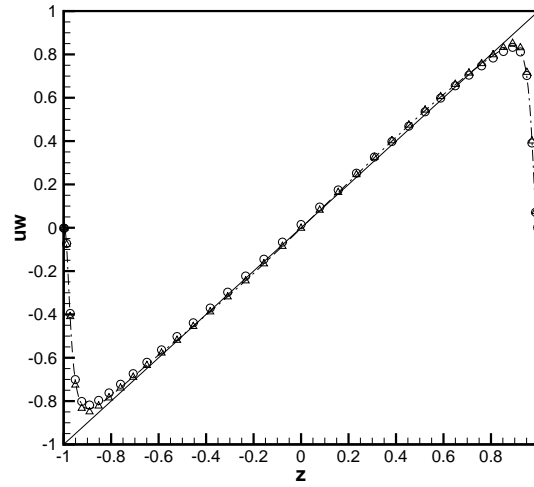
$$K(t) = \int (u'^2 + v'^2 + w'^2) dx dy dz. \quad (5.3)$$

As can be seen the mean turbulent kinetic energy profile of the full flow and flow calculated from master-mode sets ordered by $\langle |\hat{\mathbf{u}}| \rangle$ and $\langle |\hat{\Omega}| \rangle$ methods are close in the middle of the channel and they begin to diverge close to the wall. Meanwhile we can see that stress distributions across the channel of full flow has a very good agreement with the flow calculated from master-mode set ordered by methods $\langle |\hat{\mathbf{u}}| \rangle$ and $\langle |\hat{\Omega}| \rangle$.

Figure 5.11 (a) shows the derivatives of wall normal velocity calculated from master-mode set ordered by $\langle |\hat{\mathbf{u}}| \rangle$ $N_{mm} = 29716$ and $\langle |\hat{\Omega}| \rangle$ $N_{mm} = 42537$. The agreement between the derivatives of wall normal velocity for full flow and for master-mode set of both methods of ordering are remarkable. However if one examines the behaviour of the derivatives of wall normal velocity below $z^+ < 4$ it is possible to see smooth peaks at near the wall. The near-wall peaks of the derivatives of velocity are shown in figure 5.11 (b). We attribute this to an artefact of separating modes into two groups, master and slave.

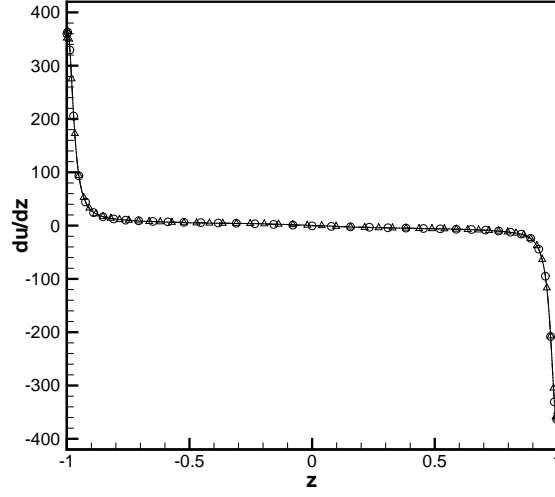


(a)

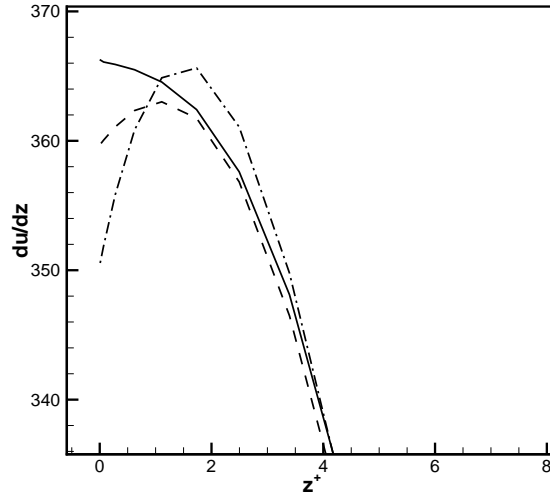


(b)

Figure 5.10: (a) turbulent kinetic energy: full flow (solid line), a minimal master-mode set ($N_{mm}=42537$) ordered by $\langle |\hat{\Omega}| \rangle$ (dashed line) and a minimal master-mode set ($N_{mm}=29716$) ordered by $\langle |\hat{\mathbf{u}}| \rangle$ (dash-dotted line). (b) Stress distributions across the channel, full flow (dash-dotted), $\langle |\hat{\Omega}| \rangle$ \triangle , $\langle |\hat{\mathbf{u}}| \rangle$ \circ , computational box size is $6 \times 2 \times 3$, $Re_\tau = 360$.



(a)



(b)

Figure 5.11: The derivatives of wall normal velocity: (a) full flow (solid line), $\langle |\hat{\mathbf{u}}| \rangle$ (circle) and $\langle |\hat{\mathbf{\Omega}}| \rangle$ (delta). (b) full flow (solid line), $\langle |\hat{\mathbf{u}}| \rangle$ (dash-dotted line) and $\langle |\hat{\mathbf{\Omega}}| \rangle$ (dashed line). Computational box size is $6 \times 2 \times 3$, $Re_\tau = 360$, $N_{mm} = 42537$ for $\langle |\hat{\mathbf{\Omega}}| \rangle$ and $N_{mm} = 29716$ for $\langle |\hat{\mathbf{u}}| \rangle$.

5.3.2 Two-point velocity correlations

Two-point correlations of velocities indicate the length scales of the turbulence structures within the channel. Since the channel flow is statistically stationary in $x - y$ planes, the spatial correlations are only dependent upon the spatial separation between two points in that plane, and are shown only as functions of two variables: a streamwise or spanwise separation. Three cases of autocorrelation coefficient in x direction were considered using equation (3.1): $R_{ij}(r)$, $R_{master-master\ ij}(r)$ and $R_{master-slave\ ij}(r)$. The calculations were performed at $Re_\tau = 360$ in a computational box of the size $L_x \times L_y \times L_z = 6 \times 3 \times 2$ using 64 complex Fourier modes in spanwise y and streamwise x directions and 160 Chebyshev modes in the wall-normal z direction.

Figure 5.14 shows the streamwise two-point correlations at $z^+ = 5.6$ for the full-flow and the master-mode set ordered by $\langle |\hat{\Omega}| \rangle$ and $\langle |\hat{\mathbf{u}}| \rangle$. One can see that u has the largest streamwise correlations, which is probably due to the alternating low- and high- speed streaks in the near-wall region. The u correlations approach zero as r increases thus indicating that the the longest streamwise structures are less than the box length ($L_x = 6$) and that the streamwise box-size is sufficient. The full-flow and the master-mode set curves for the methods $\langle |\hat{\Omega}| \rangle$ and $\langle |\hat{\mathbf{u}}| \rangle$ for the longitudinal velocity and the spanwise velocity correlations are in a reasonable agreement. However, the correlation for the master-mode set ordered by $\langle |\hat{\mathbf{u}}| \rangle$ wall-normal velocity exhibits oscillations around the respective full-flow correlation for Δx greater than about 75 (see figure 5.14 (c)) while we cannot observe it in the two point velocity correlation for the full flow. This can be caused by the sharp cut-off in the energy spectrum of the master-mode set field at approximately the same length scale. The cut-off scale is indicated by a vertical dot line in figure 5.12, which shows the corresponding energy spectrum. The relation between the length scale and the wave number, $x^+ = 360L_x/k_x$, follows from (4.3). The same oscillations one can see for the correlation of the master-mode set ordered by $\langle |\hat{\Omega}| \rangle$ (see figure 5.14).

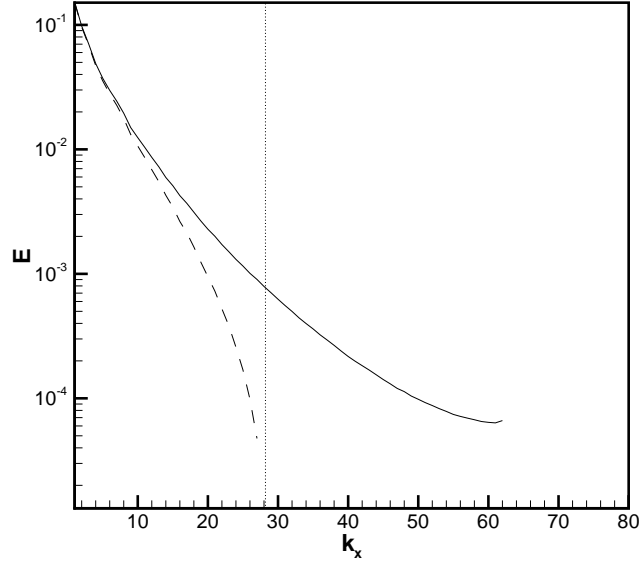


Figure 5.12: Streamwise energy spectrum. Full flow, the curve; master-mode-set, dashed line, for $Re_\tau = 360$, $z^+ = 5.6$, $L_x \times L_y = 6 \times 3$, and the minimal master-mode set ($N_{mm} = 29716$).

Two-point velocity correlations at $z^+ = 5.6$ with spanwise separations are shown in figure 5.14 (b) for the full flow and on 5.14 (d-f) for the flow calculated from the master-mode set for $\langle |\hat{\mathbf{u}}| \rangle$ and $\langle |\hat{\Omega}| \rangle$ respectively. As can be seen small oscillations of the two point wall normal spanwise velocity correlation for the flow calculated from the master-mode set exist in both cases. Overall, the streamwise and spanwise two-point correlations u and v of the master modes only give a fairly good representation of the streamwise two-point correlations of full flow. Naturally, increasing the number of modes in the master-mode set reduces the oscillations, see section 6. Figure 5.15 shows the two-point velocity correlations at $z^+ = 5.6$ between master-mode set and slave-mode set and between slave-mode set and slave-mode set one can see on figure 5.16

The two-point velocity correlations at $z^+ = 1.7$ between master-mode set and slave-mode set for $\langle |\hat{\mathbf{u}}| \rangle$ and $\langle |\hat{\Omega}| \rangle$ as shown in figure 5.13 have a markedly different amplitude from that at $z^+ = 5.6$.

It is important to note that near the wall at $z^+ = 1.7$ two-point velocity correlation for $\langle |\hat{\mathbf{u}}| \rangle$ and $\langle |\hat{\Omega}| \rangle$ $R_{u_{master}u_{slave}} \approx -1$, $R_{v_{master}v_{slave}} \approx -1$, $R_{w_{master}w_{slave}} \approx -1$ as well.

As mentioned before we represent the solution \mathbf{u} as a sum $\mathbf{u} = \mathbf{u}_m + \mathbf{u}_s$, where $\mathbf{u}_m = \mathbf{u}_m(x; t)$ corresponds to the master modes and $\mathbf{u}_s = \mathbf{u}_s(x; t)$ is the remaining part, slave modes. Since, $R_{u_{master}u_{slave}} \approx -1$ near the wall at $z^+ = 1.7$ this implies that master modes can be used to reconstruct the slave modes in the following way :

$$\mathbf{u} = \mathbf{u}_m + \mathbf{u}_s$$

and

$$\mathbf{u}_s = -k\mathbf{u}_m$$

where k is a constant to satisfy the two-point velocity correlation value near the wall.

The reason for such a behavior is obvious. Close to the wall (at $z^+ = 1.7$ in particular) the velocity profile is linear in z^+ . However, the Chebyshev polynomials oscillate strongly, with higher modes (slaves) simply compensating the oscillations of the lower modes (masters) to produce a non-oscillating linear profile.

Overall, these comparisons show that master-mode set alone gives a reasonable approximation for two-point velocity correlations, even though there are some oscillations. One can see that two-point velocity correlations calculated from master-modes set ordered by $\langle |\hat{\Omega}| \rangle$ ($N_{mm} = 42537$) did not reduce the oscillations even though the size of the set was bigger than it was for $\langle |\hat{\mathbf{u}}| \rangle$. But we can see that increasing the number of modes in the master-mode set ordered by $\langle |\hat{\mathbf{u}}| \rangle$ to ($N_{mm} = 41069$), which is still less than the number of modes for the case ordered by $\langle |\hat{\Omega}| \rangle$, reduces the oscillations, see figure 5.17

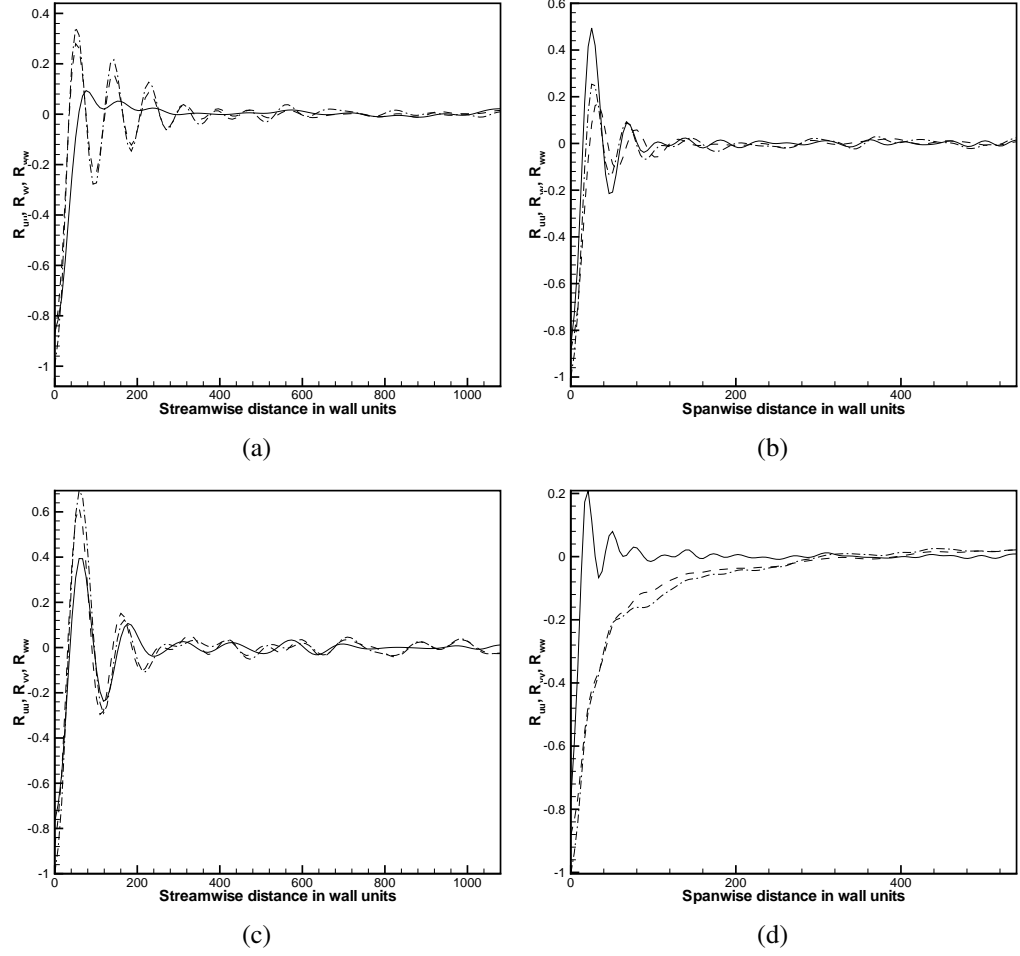


Figure 5.13: Two-point velocity cross-correlations between master-mode set and slave-mode set, R_{uu} (solid line), R_{vv} (dashed line) and R_{wv} (dash-dotted line), at $z^+ = 1.7$. a) streamwise direction $\langle |\hat{\mathbf{u}}| \rangle$, c) streamwise direction $\langle |\hat{\Omega}| \rangle$, b) spanwise direction $\langle |\hat{\mathbf{u}}| \rangle$ and d) spanwise direction $\langle |\hat{\Omega}| \rangle$. $N_{mm} = 42537$ for $\langle |\hat{\Omega}| \rangle$ and $N_{mm} = 29716$ for $\langle |\hat{\mathbf{u}}| \rangle$.

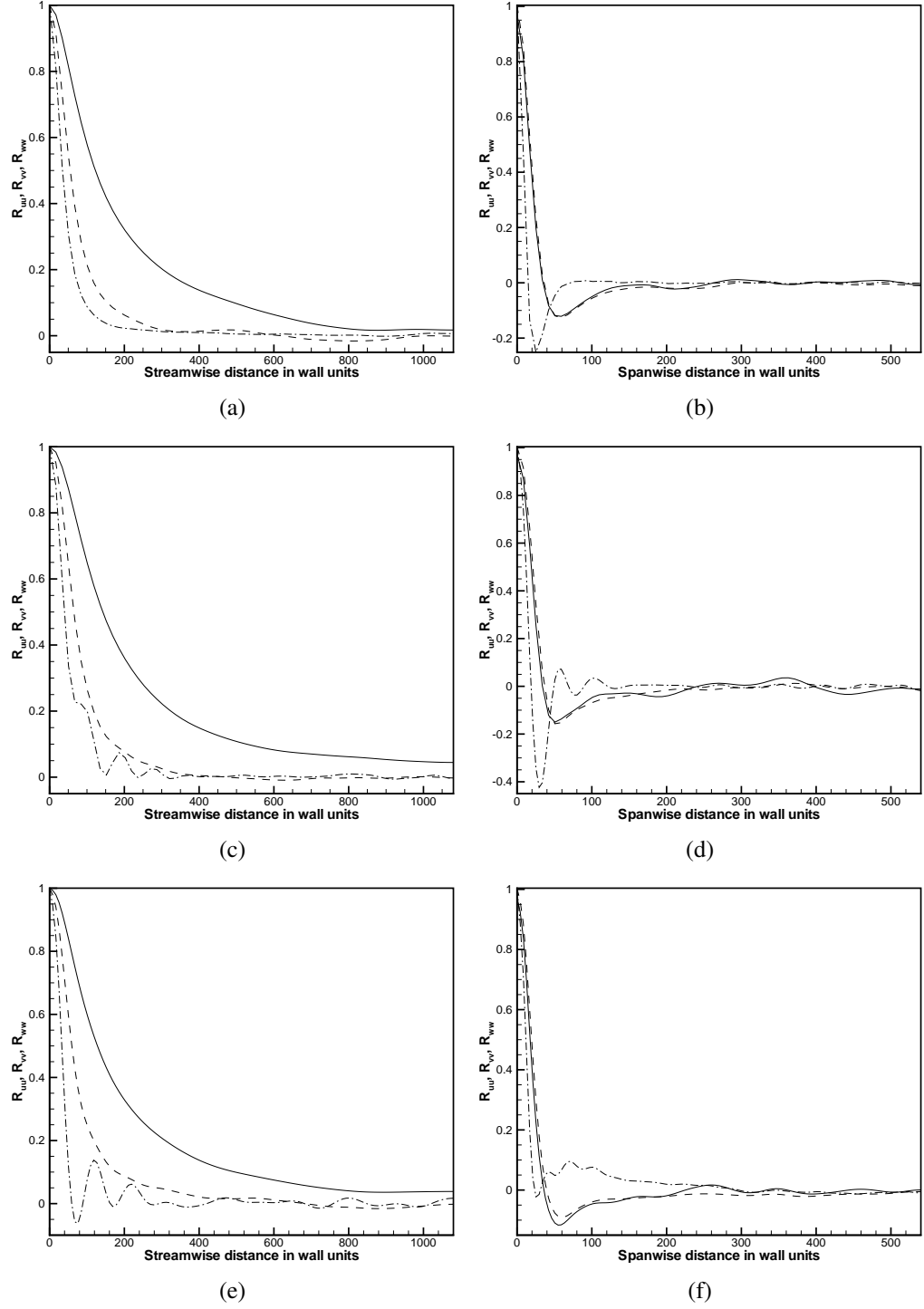


Figure 5.14: Two-point velocity correlations, R_{uu} (solid line), R_{vv} (dashed line) and R_{ww} (dash-dotted line), at $z^+ = 5.6$. Full flow (a) streamwise direction, (b) spanwise direction; Two-point velocity auto-correlations of the master-mode set (c) $\langle |\hat{\mathbf{u}}| \rangle$ streamwise direction, (d) $\langle |\hat{\mathbf{u}}| \rangle$ spanwise direction, (e) $\langle |\hat{\mathbf{Q}}| \rangle$ streamwise direction, (f) $\langle |\hat{\mathbf{Q}}| \rangle$ spanwise direction. $N_{mm} = 42537$ for $\langle |\hat{\mathbf{Q}}| \rangle$ and $N_{mm} = 29716$ for $\langle |\hat{\mathbf{u}}| \rangle$.

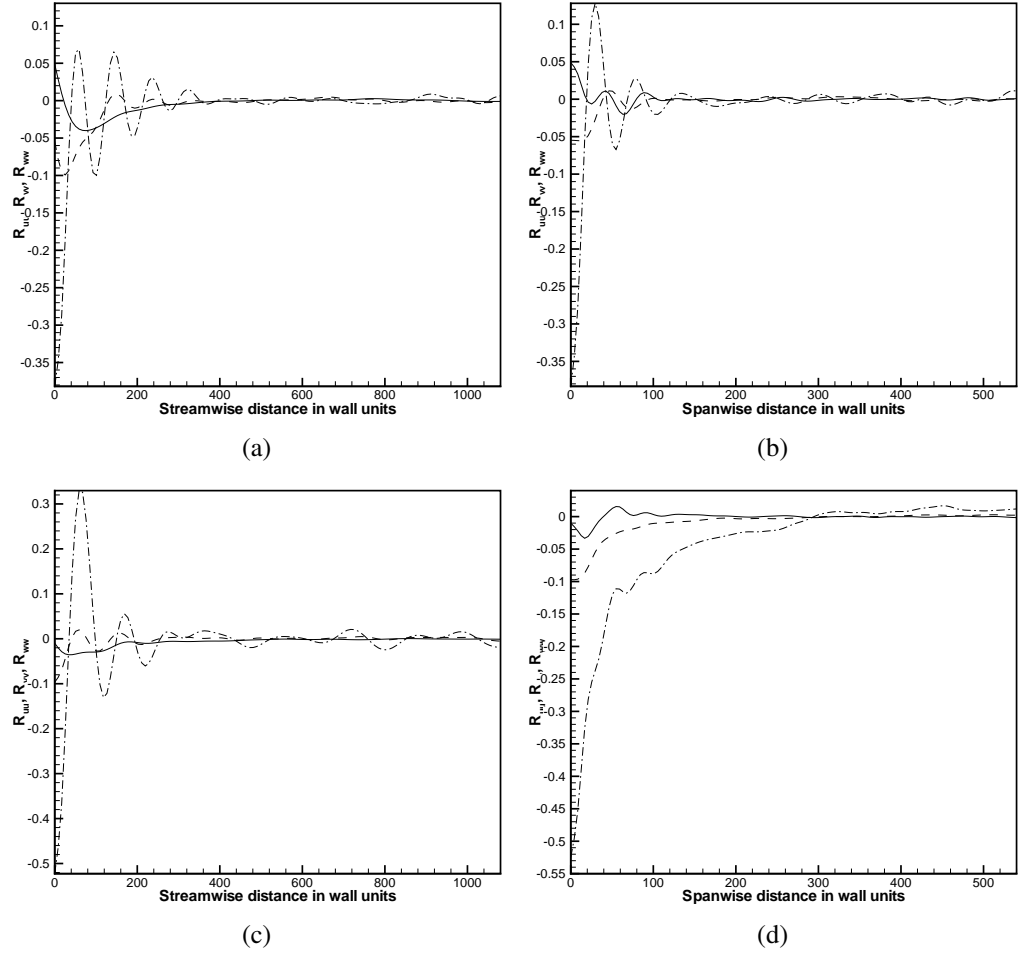


Figure 5.15: Two-point velocity cross-correlations between master-mode set and slave-mode set, R_{uu} (solid line), R_{vv} (dashed line) and R_{ww} (dash-dotted line), at $z^+ = 5.6$: (a) $\langle |\hat{\mathbf{u}}| \rangle$ streamwise direction, (b) $\langle |\hat{\mathbf{u}}| \rangle$ spanwise direction, (c) $\langle |\hat{\mathbf{Q}}| \rangle$ streamwise direction and (d) $\langle |\hat{\mathbf{Q}}| \rangle$ spanwise direction. $N_{mm} = 42537$ for $\langle |\hat{\mathbf{Q}}| \rangle$ and $N_{mm} = 29716$ for $\langle |\hat{\mathbf{u}}| \rangle$.

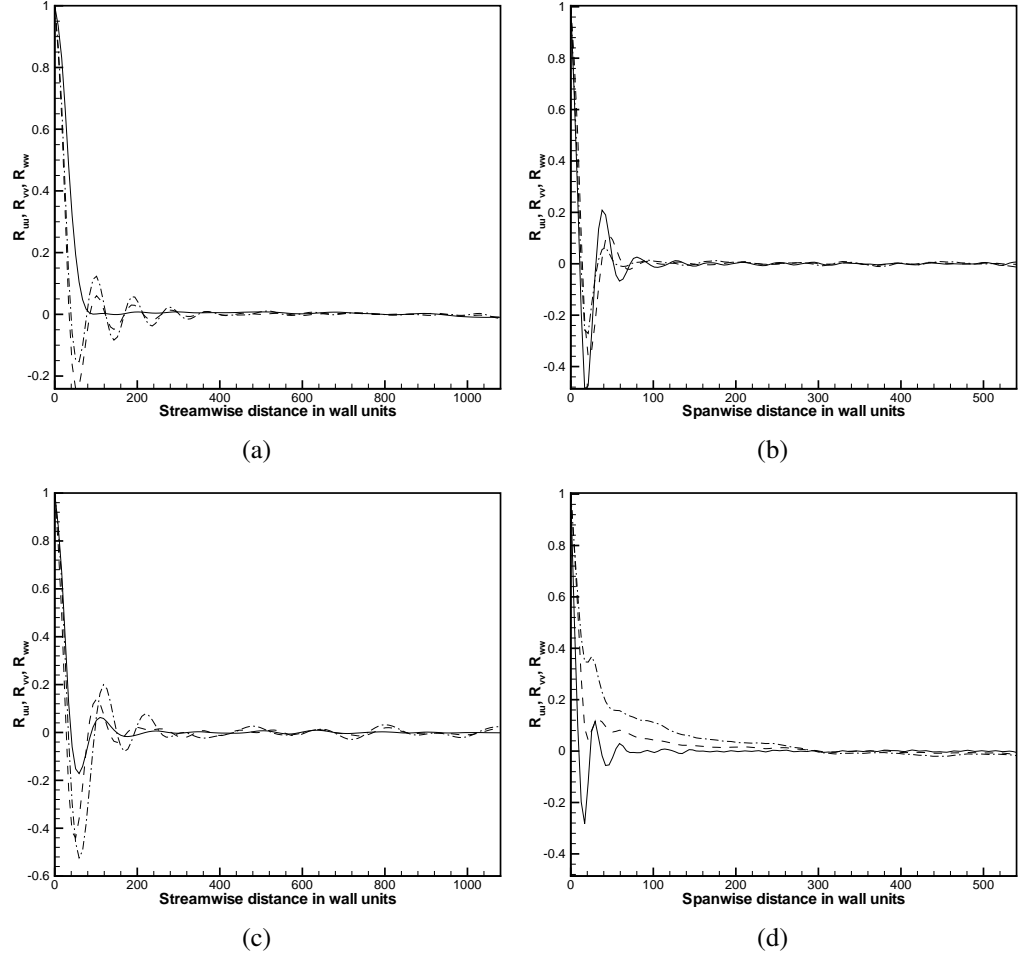


Figure 5.16: Two-point velocity auto-correlations of the slave-mode set, R_{uu} (solid line), R_{vv} (dashed line) and R_{ww} (dash-dotted line), at $z^+ = 5.6$: (a) $\langle |\hat{\mathbf{u}}| \rangle$ streamwise direction, (b) $\langle |\hat{\mathbf{u}}| \rangle$ spanwise direction, (c) $\langle |\hat{\mathbf{\Omega}}| \rangle$ streamwise direction and (d) $\langle |\hat{\mathbf{\Omega}}| \rangle$ spanwise direction. $N_{mm} = 42537$ for $\langle |\hat{\mathbf{\Omega}}| \rangle$ and $N_{mm} = 29716$ for $\langle |\hat{\mathbf{u}}| \rangle$.

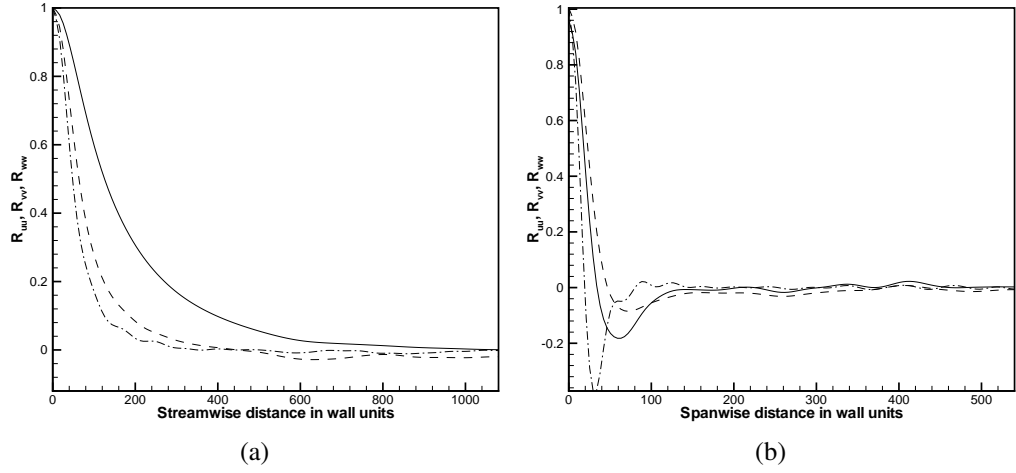
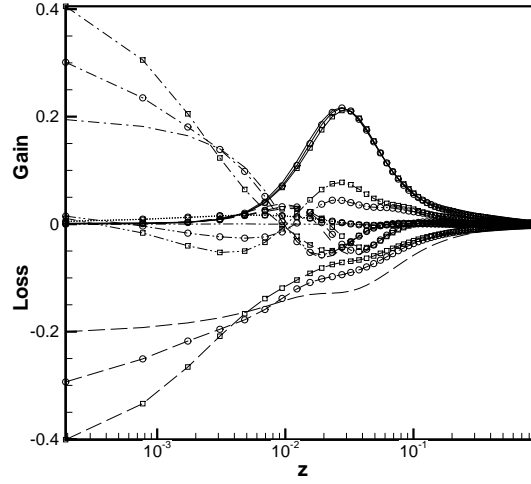


Figure 5.17: Two-point velocity auto-correlations of the master-mode sets ordered by $\langle |\hat{\mathbf{u}}| \rangle$ R_{uu} (solid line), R_{vv} (dashed line) and R_{ww} (dash-dotted line) at $z^+ = 5.6$, $N_{mm} = 41069$: (a) streamwise direction, (b) spanwise direction.

5.3.3 Reynolds-stress budgets.

Using the transport equation of the Reynolds stresses one can explore the difference between Reynolds-stress budgets calculated from full flow and the master-mode set ordered by methods $\langle |\hat{\mathbf{u}}| \rangle$, $\langle |\hat{\mathbf{\Omega}}| \rangle$, respectively $N_{mm} = 29716$ and $N_{mm} = 42537$. The calculations were performed at $Re_\tau = 360$, $L_x \times L_y \times L_z = 6 \times 3 \times 2$ with the grid size, respectively, $N_x = 128$, $N_y = 128$ and $N_z = 160$ in the x , y and z directions, using equations (3.2- 3.7).

Figures 5.19 (a-b) show the contributions of the individual terms to the budget for the turbulent kinetic energy for full flow (a) and for the master-mode set only (b-c) for methods $\langle |\hat{\mathbf{u}}| \rangle$ and $\langle |\hat{\mathbf{\Omega}}| \rangle$ respectively. Left-hand figures use linear coordinate axes and right hand figures employ logarithmic axes. It is important to recognize that the results near the wall related to dissipation rates are sensitive to the number of master modes. Away from the wall, the budget for the dissipation rate of the turbulence kinetic energy reveals that the turbulent production term and the dissipation rate are the dominant terms. The same domination of the production term and the dissipation rate appears in the budget of turbulent kinetic energy calculated from master-mode set for $\langle |\hat{\mathbf{u}}| \rangle$ and $\langle |\hat{\mathbf{\Omega}}| \rangle$. Close to the wall, dissipation rate and the vis-



(a)

Figure 5.18: Terms in the budget of the turbulence kinetic energy for full flow and master-mode set. Curves with square symbols represent the turbulence kinetic energy calculated from master-mode set only ordered by $\langle |\hat{\mathbf{u}}| \rangle$ and with circle symbols calculated from master-mode set only ordered by $\langle |\hat{\Omega}| \rangle$

cous diffusion from the master-mode set for $\langle |\hat{\mathbf{u}}| \rangle$ has a value two times greater than in the full flow but close to the center they are the same. Meanwhile dissipation rate and the viscous diffusion from the master-mode set for $\langle |\hat{\Omega}| \rangle$ has a value 0.3 which is more close to the full flow value 0.2.

For the rest of turbulent kinetic energy budget terms there is good agreement between the turbulent kinetic energy budget of full flow and the turbulent kinetic energy budget of master-mode set for $\langle |\hat{\mathbf{u}}| \rangle$ and $\langle |\hat{\Omega}| \rangle$. Reynolds-stress budgets $\overline{u'w'}$, $\overline{u'u'}$, $\overline{v'v'}$ for three cases (full flow, $\langle |\hat{\mathbf{u}}| \rangle$ and $\langle |\hat{\Omega}| \rangle$) can be seen in the figures 5.20-5.23. Also the terms of the budgets of turbulent kinetic energy for full flow and for the flow calculated from $\langle |\hat{\mathbf{u}}| \rangle$ and $\langle |\hat{\Omega}| \rangle$ was plotted in logarithmic region in figure 5.18; this gives an opportunity to compare these three terms. Overall, these comparisons show that master modes alone give a reasonable approximation for turbulent kinetic energy budget, even though there are some deviations very close to the wall.

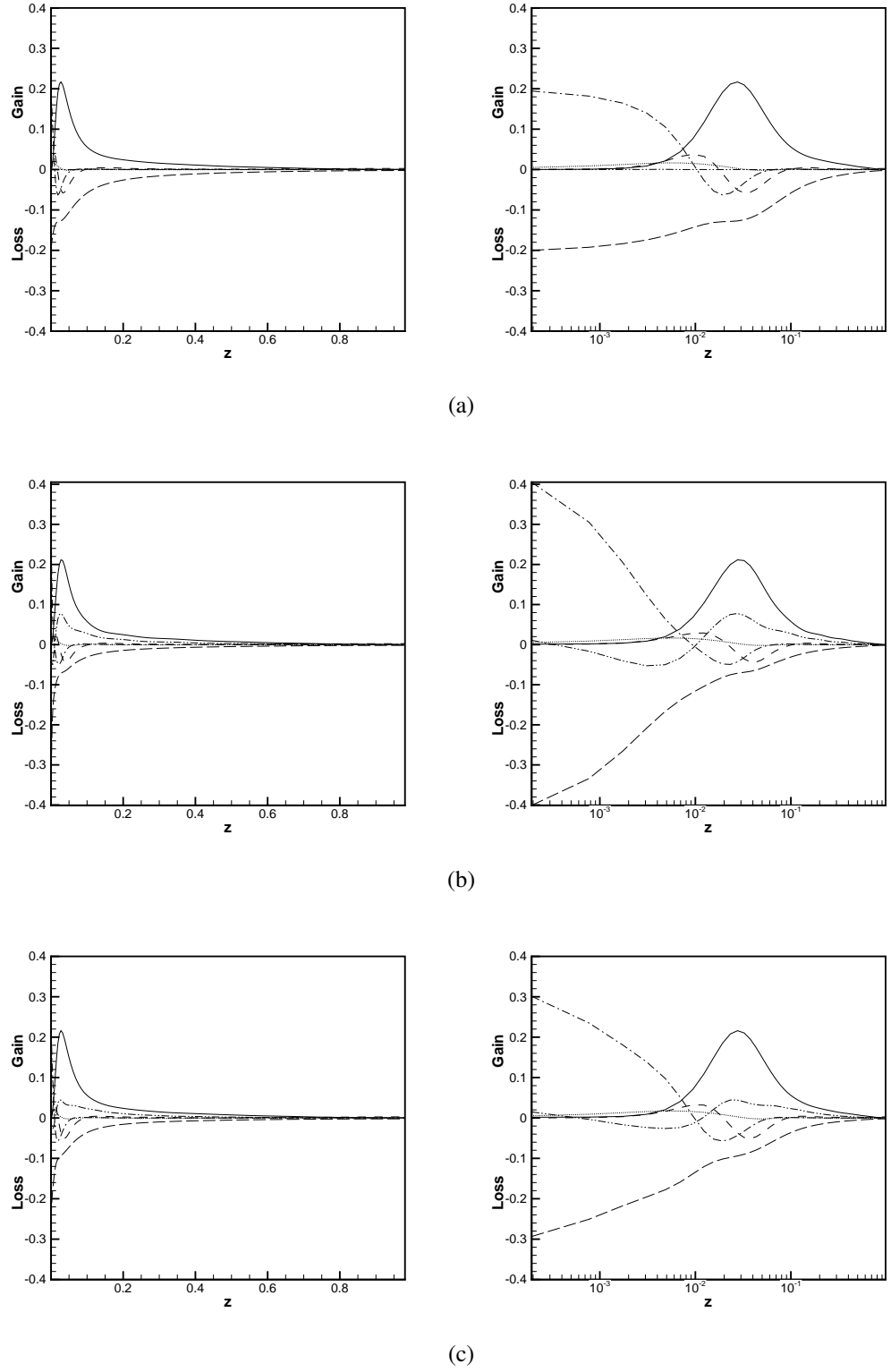


Figure 5.19: Terms in the budgets of turbulent kinetic energy: (a) full flow, (b) master-mode set only ordered by $\langle |\hat{\mathbf{u}}| \rangle$ and (c) master-mode set only ordered by $\langle |\hat{\Omega}| \rangle$. P (solid line), T (dashed line), D (dash-dotted line), Π (dotted line), ε (long dash-line), Σ (dash-dotted-dotted line). Right-hand figures show the same data with logarithmic region.

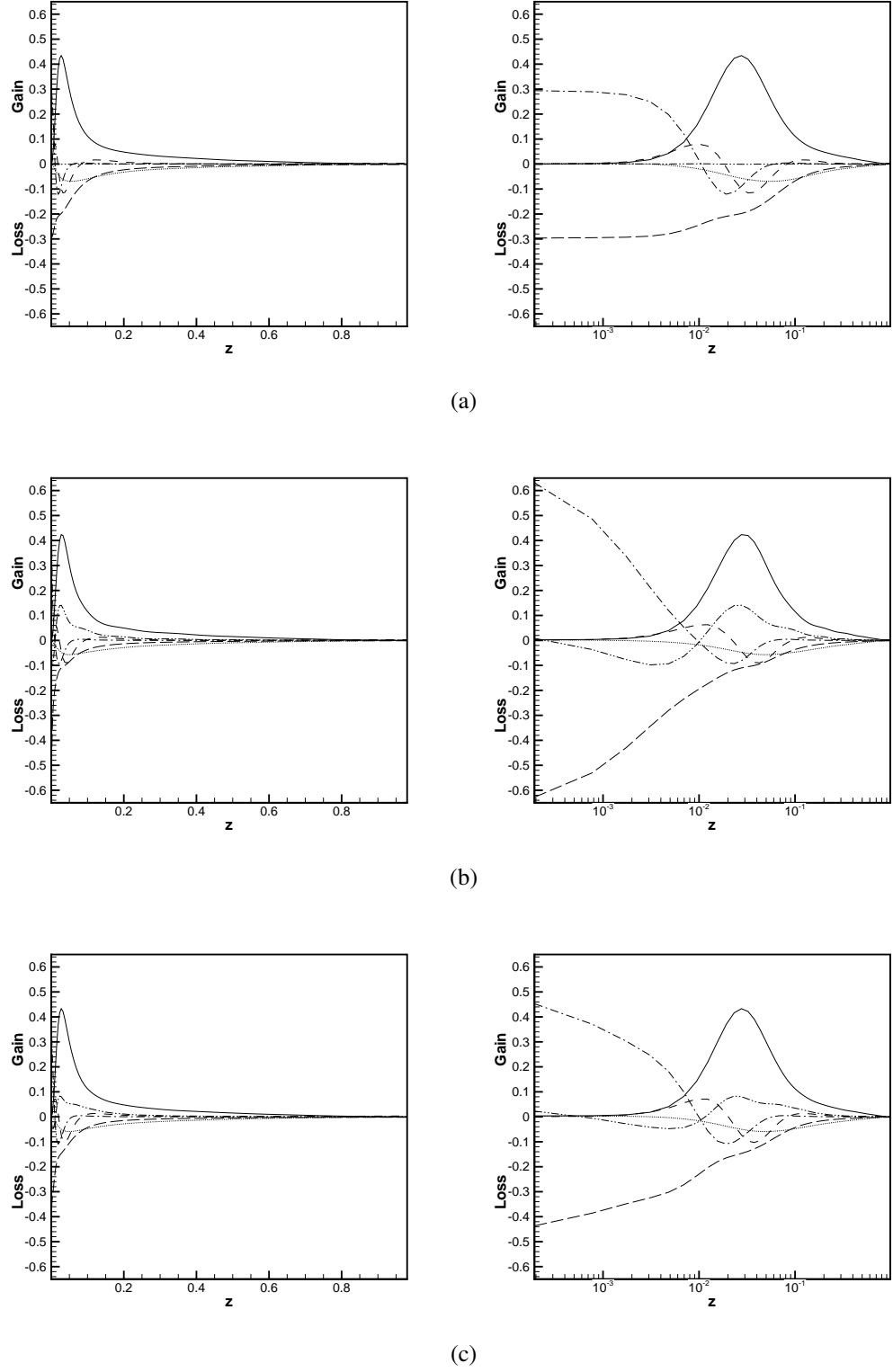


Figure 5.20: $\overline{u'u'}$: (a) full flow, (b) master-mode set only ordered by $\langle |\hat{\mathbf{u}}| \rangle$ and (c) master-mode set only ordered by $\langle |\hat{\Omega}| \rangle$. P (solid line), T (dashed line), D (dash-dotted line), Π (dotted line), ε (long dash-line), Σ (dash-dotted-dotted line). Right hand figures show the same data with logarithmic region.

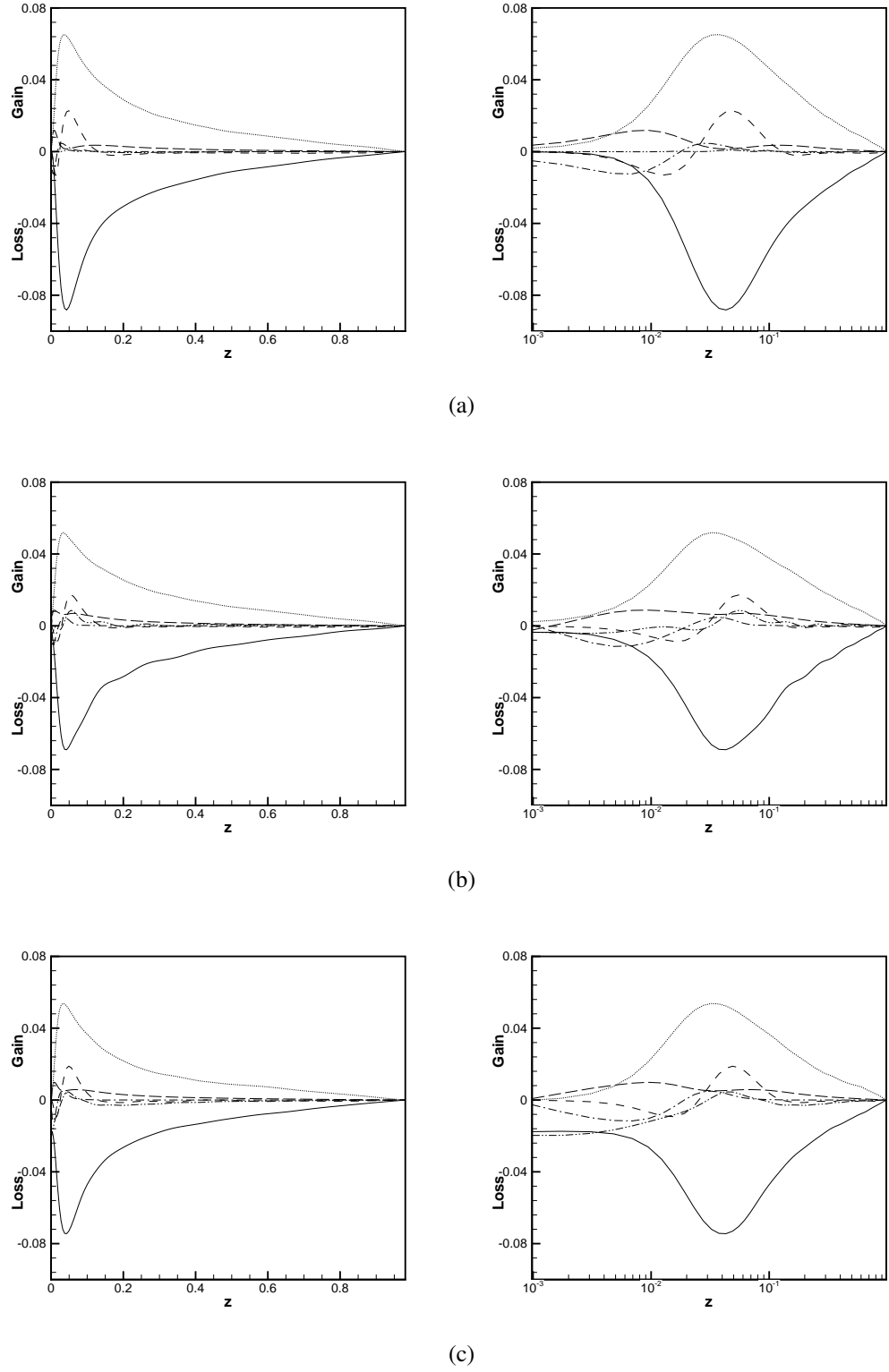


Figure 5.21: $\overline{u'w'}$: (a) full flow, (b) master-mode set only ordered by $\langle |\hat{\mathbf{u}}| \rangle$ and (c) master-mode set only ordered by $\langle |\hat{\Omega}| \rangle$. P (solid line), T (dashed line), D (dash-dotted line), Π (dotted line), ε (long dash-line), Σ (dash-dotted-dotted line). Right hand figures show the same data with logarithmic region.

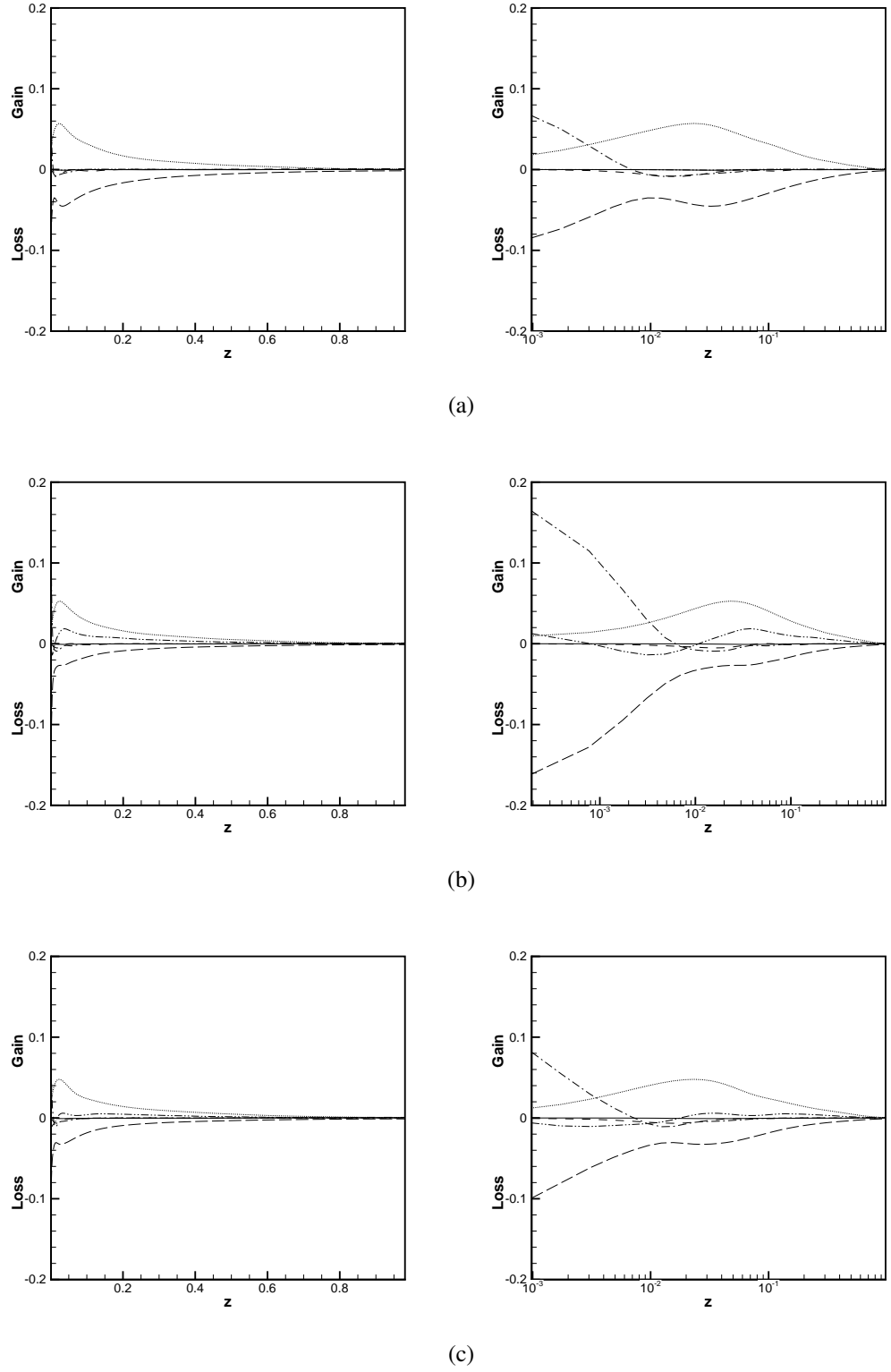


Figure 5.22: $\overline{v'v'}$: (a) full flow, (b) master-mode set only ordered by $\langle |\hat{\mathbf{u}}| \rangle$ and (c) master-mode set only ordered by $\langle |\hat{\Omega}| \rangle$. P (solid line), T (dashed line), D (dash-dotted line), Π (dotted line), ε (long dash-line), Σ (dash-dotted-dotted line). Right hand figures show the same data with logarithmic region.

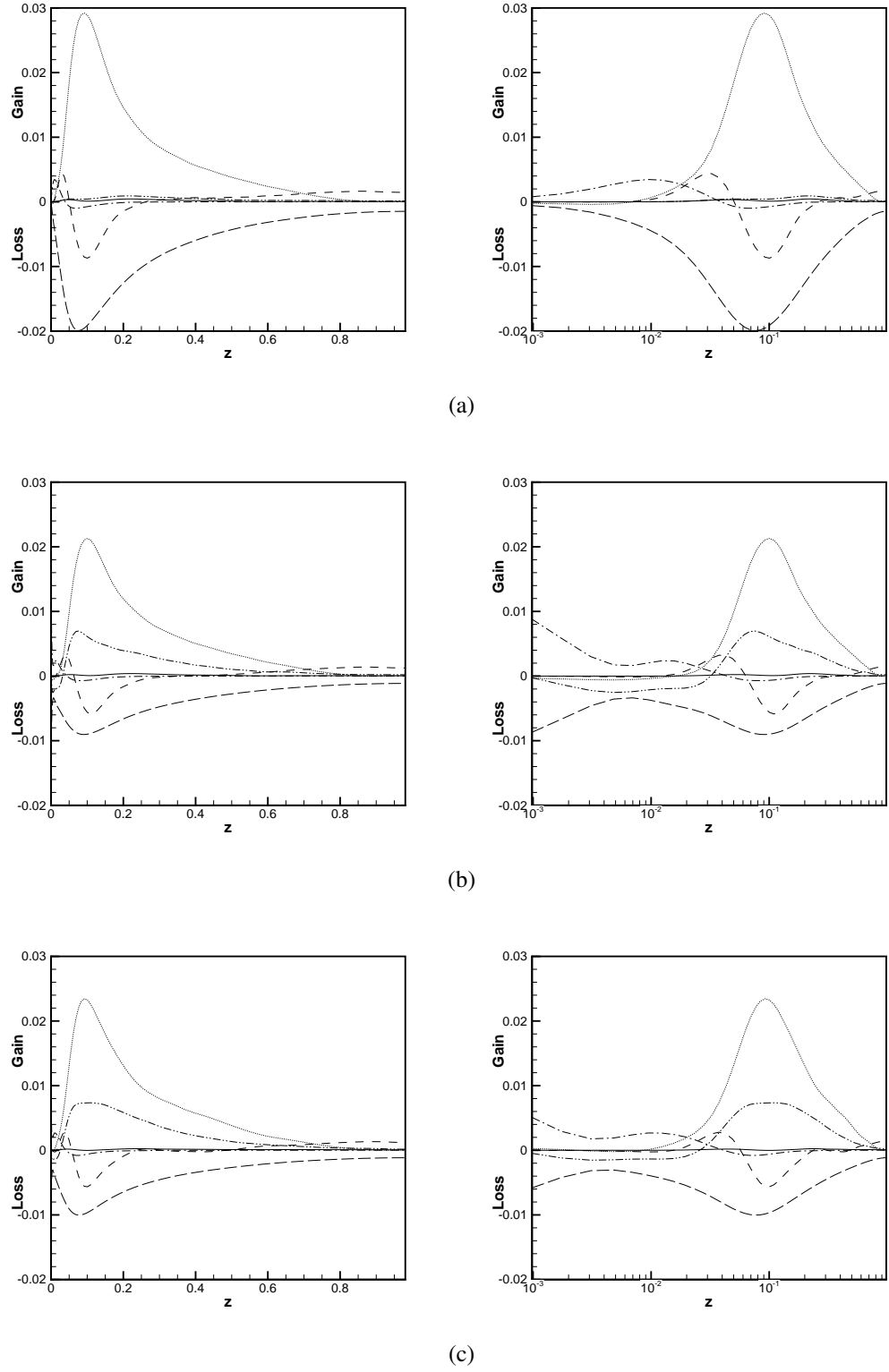


Figure 5.23: $\overline{w'w'}$: (a) full flow, (b) master-mode set only ordered by $\langle |\hat{\mathbf{u}}| \rangle$ and (c) master-mode set only ordered by $\langle |\hat{\Omega}| \rangle$. P (solid line), T (dashed line), D (dash-dotted line), Π (dotted line), ε (long dash-line), Σ (dash-dotted-dotted line). Right hand figures show the same data with logarithmic region.

5.3.4 Visualization of the flow

This section explores the organised structures of the developed turbulent flow. The numerical experiments have been performed in a computational box of size $L_x \times L_y \times L_z = 6 \times 3 \times 2$ on a grid $N_x = 128, N_y = 128$ and $N_z = 160$ in the x, y and z directions at $Re_\tau = 360$.

The near-wall structures (located below 70 wall units) include streamwise vortices, streaks, that is alternating high-speed and low-speed regions, and ejections and sweeps which are parts of a bursting phenomenon (Kline *et al.* [52]; Corino & Brodkey [53]; Kim *et al.* [54]). Many theories and conceptual models of organised structures have been proposed (Jang *et al.*, [55]; Sreenivasan [56]; Waleffe *et al.* [57]; Butler & Farrell [58]; Jimenez & Orlandi [59]). Studies of organised structures have already begun to bear practical fruit. A good example is the use of the understanding of streak formation for developing an optimal control of a turbulent boundary layer reported by Kim [60].

However, many questions in this field remain unanswered (Jimenez, 2000). One such question concerns the relative importance of various organised structures. Can they be classified, say, into primary and secondary? We attempt to look into this question by observing the structures in the master-mode sets and slave-mode sets. It seems natural to expect that the more important structures should belong to the master-mode set.

In section 4.4 we have shown that the best way of ordering the modes is by the energy-based method. Therefore in this chapter all visualizations are taken from the results obtained with this method. The flow field was calculated from the master-mode set only and from the entire solution and the structures was compared. The following results were obtained with the numbers of master modes $N_{mm} = 29716$.

The contours of streamwise velocity fluctuation in x - z plane (see Figure 5.24) at the middle of the channel exemplify that the flow calculated from the master-mode set alone (b) give a very good representation of the streamwise velocity fluctuation

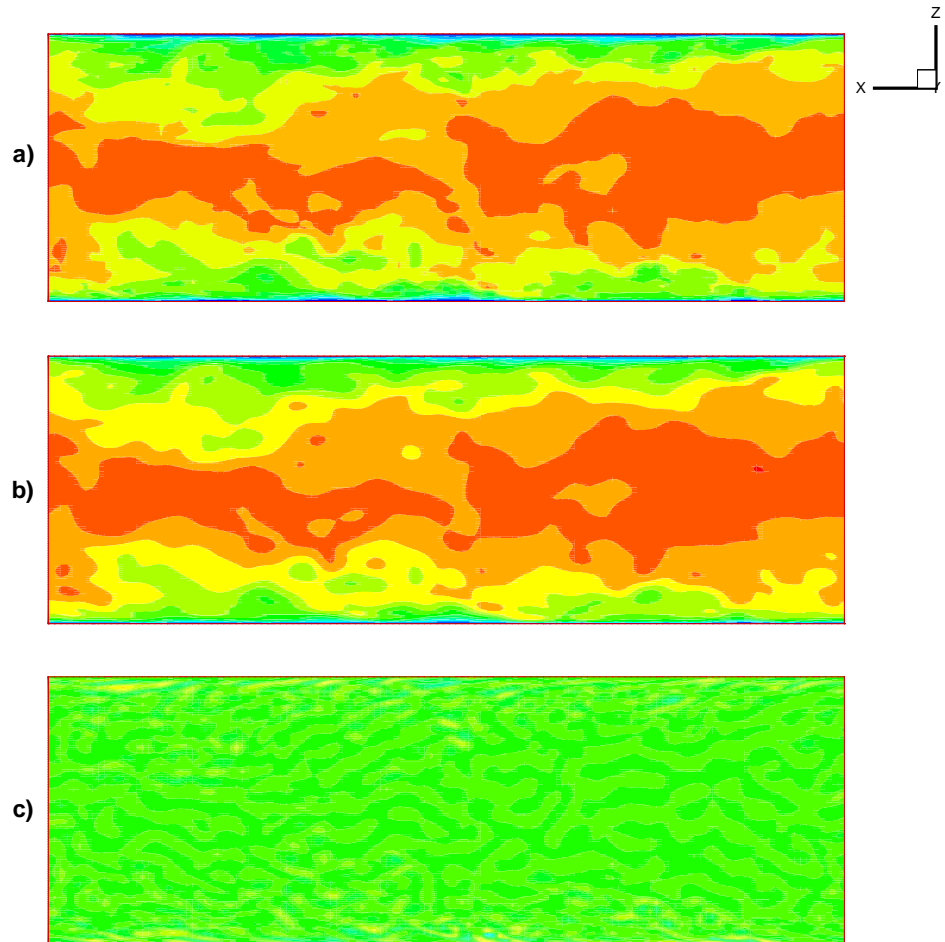


Figure 5.24: Contours of streamwise velocity fluctuation in $x-z$ plane. a) full flow; b) master modes $N_{mm} = 29716$ c) slave modes. $Re_\tau = 360$

of the full flow (a). Figure 5.25 shows the contours of streamwise vorticity in the $x - y$ plane. Figure 5.25 has three cases. Case (a) is the full flow, case (b) is the flow calculated from the master-mode set only and case (c) is the flow calculated from the slave-mode set only. As one can see the master-mode set still keep the same structure of streamwise vorticity as in the full flow. The contours of streamwise velocity in near-wall turbulence flow in $x - y$ plane (see Figure 5.26) at the $z^+ = 5.6$ show a comparison between contour of streaks for full flow (a), master modes (b) and slave modes (c). It's easy to see that master modes still keep all the streaks and the structure of the streaks is similar to that of fully developed turbulent flow while we can not observe this structure in the slave modes.

If we look at the vorticity component in figure 5.27 which shows iso-surface of vorticity in the x-direction we find out that neither the flow calculated from master-mode set nor the flow calculated from slave-mode set has the same structure as the full developed turbulent flow. The comparisons made so far show that the minimal master-mode set captures most of the structures. Figures 5.28-5.30 show how master-mode set reconstruct the full flow in time. Figure 5.28 shows the contours of streamwise vorticity in $x - y$ plane at $t = 0$ for full flow (a) and master modes (b). The master-mode set determine the basic structure of the flow and set up the dissipative structures (slave modes). Figure 5.29 shows the same contours at $t = 0.0025$. One can notice that the flow calculated from the master-mode set is recovering the slave modes. Finally at time $t = 0.01$ the master-mode set have recovered the full flow, see figure 5.30.

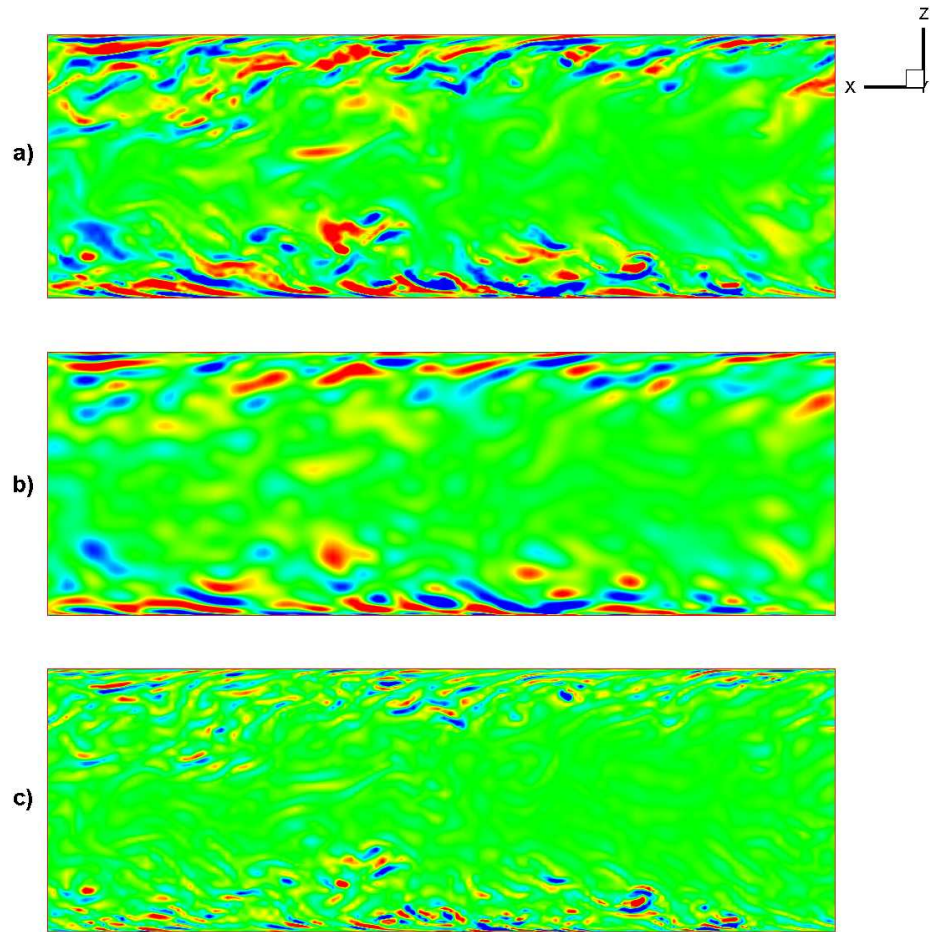


Figure 5.25: Contours of streamwise vorticity in $x-z$ plane: a) full flow; b) master-mode set, $N_{mm} = 29716$; c) slave-mode set. $Re_\tau = 360$

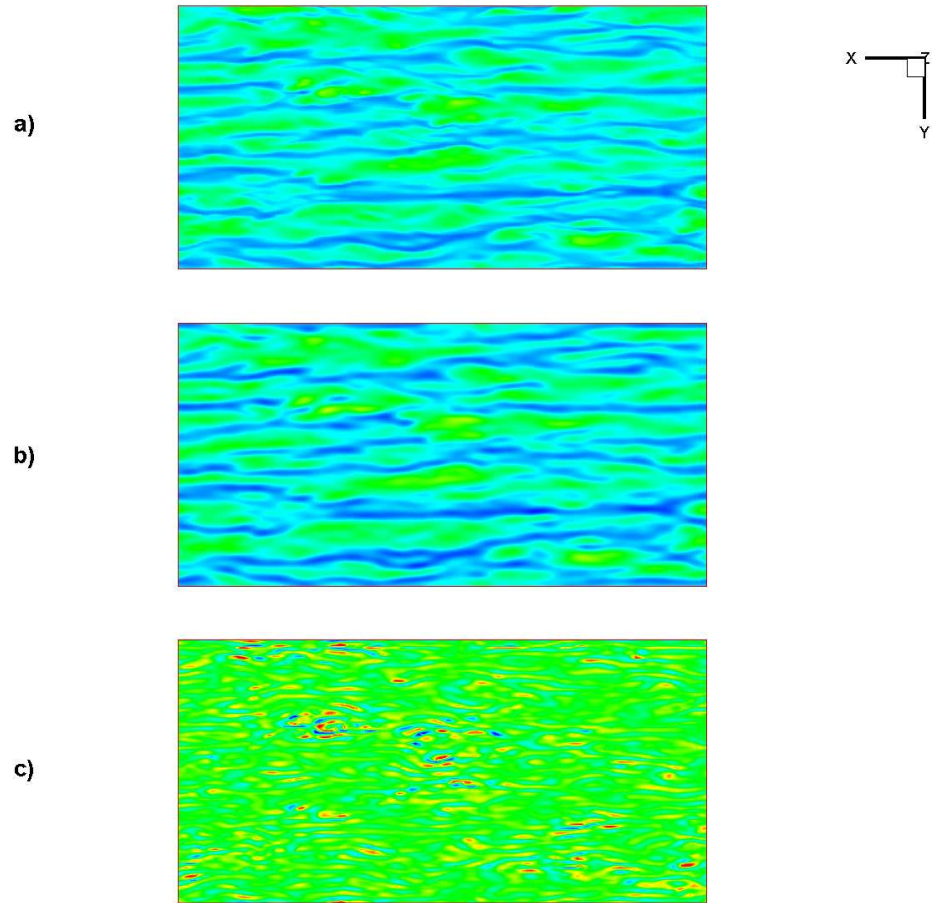


Figure 5.26: Contours of streaks in near-wall turbulence flow at $z^+ = 5.6$ in $x - y$ plane: a) full flow; b) master-mode set, $N_{mm} = 29716$; c) slave-mode set. $Re_\tau = 360$

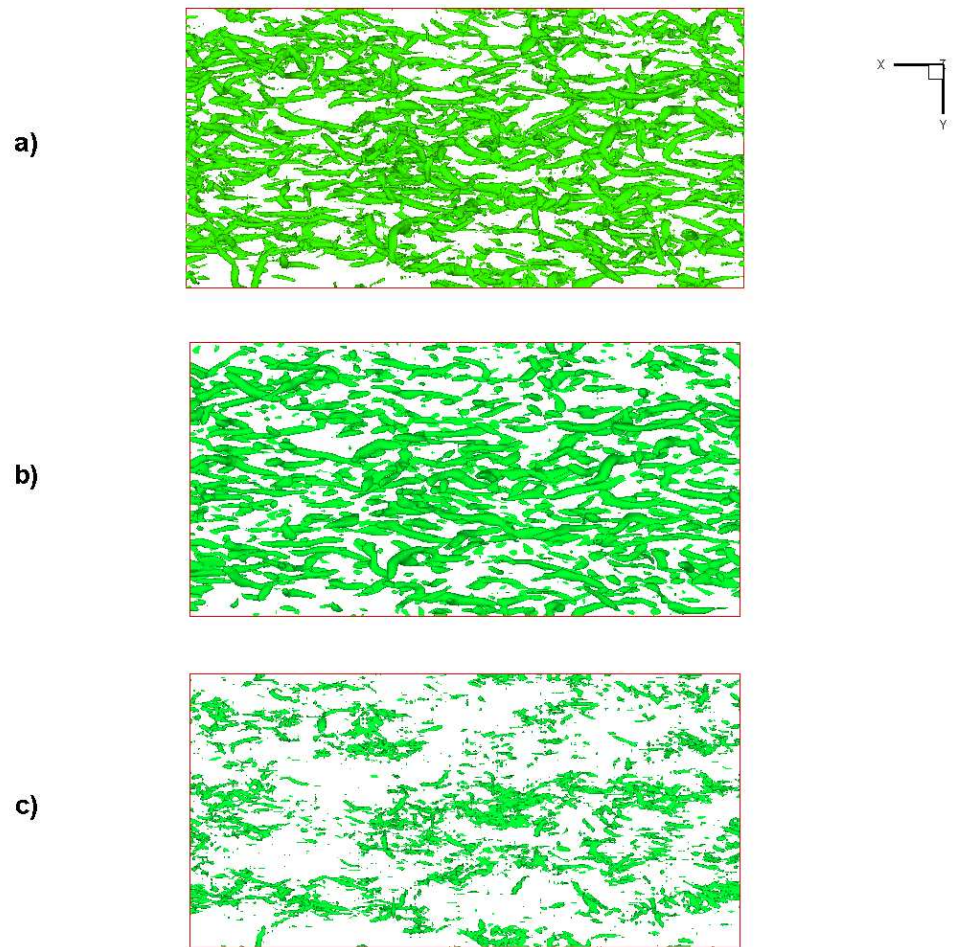


Figure 5.27: Iso-surface of vorticity in the x-direction: a) full flow; b) master-mode set, $N_{mm} = 29716$; c) slave-mode set, $Re_\tau = 360$.

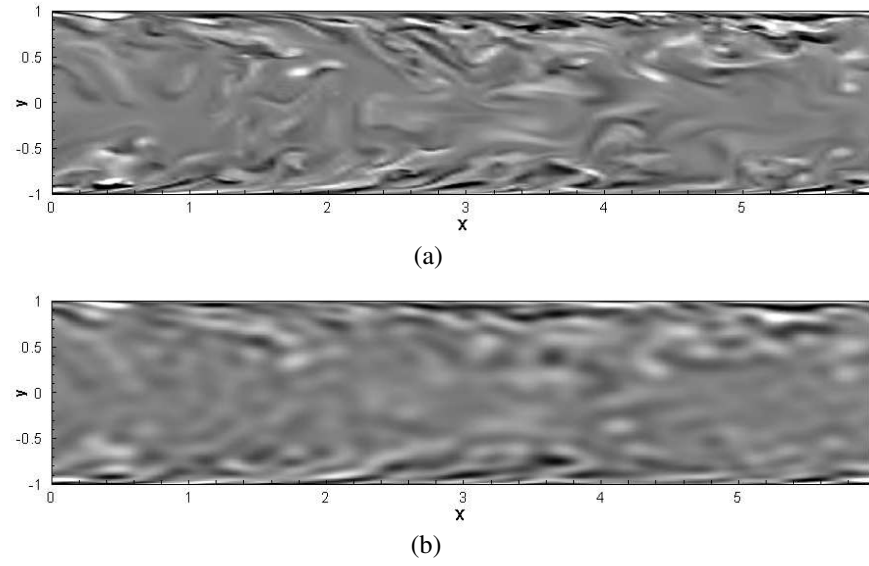


Figure 5.28: Contours of vorticity: a) for full flow; b) the flow calculated from master-mode set only, $N_{mm} = 29716$. $Re_\tau = 360$, $t = 0$.

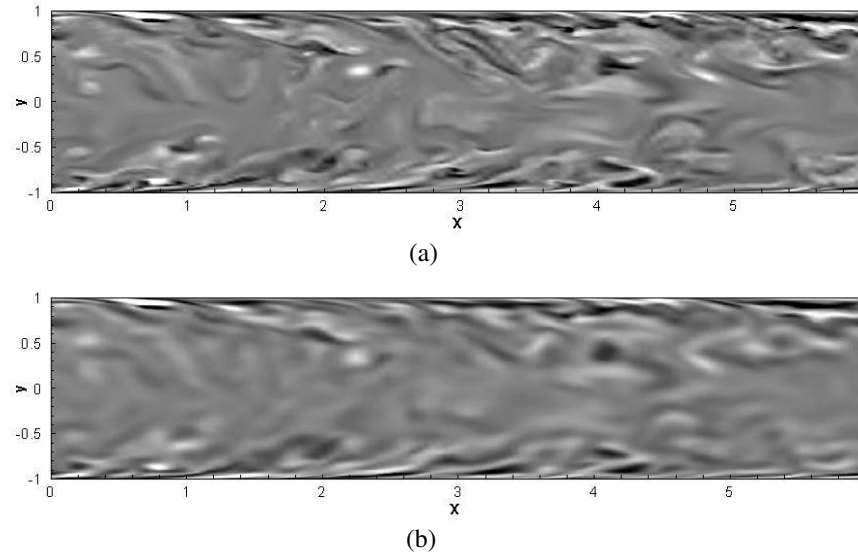


Figure 5.29: Contours of vorticity: a) for full flow; b) the flow calculated from master-mode set only, $N_{mm} = 29716$. $Re_\tau = 360$, $t = 0.0025$.

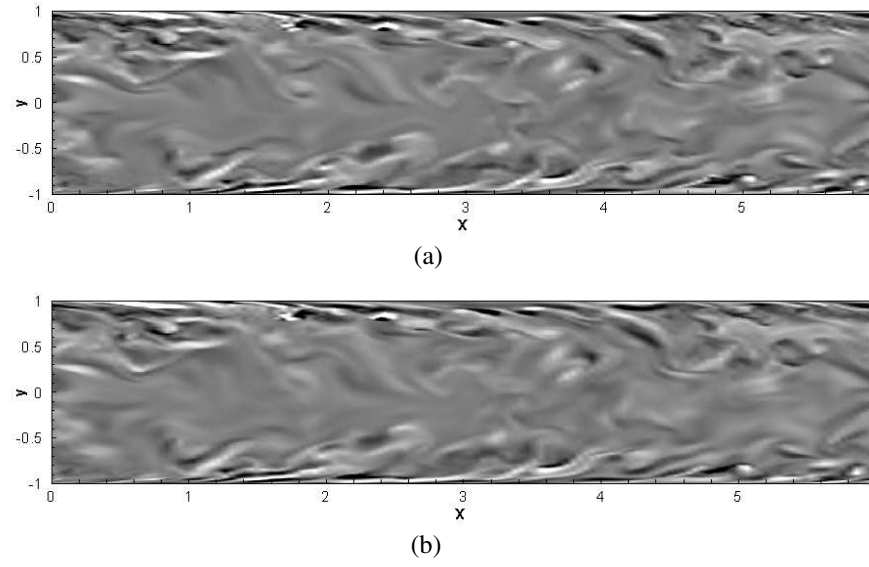


Figure 5.30: Contours of vorticity: a) for full flow; b) the flow calculated from master-mode set only, $N_{mm} = 29716$. $Re_\tau = 360$, $t = 0.01$

6 Master-mode database

The properties of the master-mode-set, namely, its relatively small size and the possibility of recovering all other modes if necessary, make the master-mode-set suitable for creating a time-history database of a turbulent flow. For such a database a compromise should be made between the number of modes recorded and the recovery rate α (see 5.1). Increasing the number of modes above the minimal master-mode set size also improves the accuracy with which the master-mode set approximates the flow. In the course of the present study two master-mode-set databases were created, both for the channel flow at $Re_\tau = 360$. The first database contains a time history of the master-mode-set with $N_m = 51508$ modes, which is about twice the size of the minimal master-mode set, for the box size $L_x \times L_y = 6 \times 3$ and the duration $T = 40$. The convergence rate given by (5.1) for this database is $\alpha \approx 10$. Therefore, achieving 1% accuracy of the recovered solution requires the slave mode calculation time $\Delta T = \alpha^{-1} \ln 0.001 \approx 0.4$. The total size of the database is 112.7Gb. A fully resolved database would require about 2.6Tb of storage, other things being equal. The second database is for the box size $L_x \times L_y = 14 \times 9$ with $N_m = 2170044$, which is about five times the size of the minimal master-mode-set, $T = 15$, and $\alpha \approx 160$, which gives $\Delta T \approx 0.03$. It uses 1.78Tb of disk storage. A fully resolved database would require about 15.2Tb of storage, other things being equal. As an alternative to recovering the slave modes one could simply store a set of instantaneous flow fields of the original calculations with the time interval ΔT , and recover the time history by running the full Navier-Stokes calculation using the nearest stored flow field as the initial condition. The calculations needed for recovering the slave modes are of a similar volume to full flow calculations, so, the CPU time required would be of the same order of magnitude in both approaches. For the second approach one would need to store $T/\Delta T$ snapshots, which would require

only about 3.2Gb storage for the first database and 270Gb storage for the second database. However, in order to reproduce exactly the same flow by running a full Navier-Stokes calculation starting from the stored snapshot one would need to use a computer of the same architecture as that on which the original calculation was performed, as otherwise rounding errors would lead to the deviation of the original and reproduced solution due to its instability. In contrast, recovery of the slave modes is a stable procedure. The master-mode database has the advantage of the possibility to use it as an approximate time history description of the flow without doing any recovery at all. The increase in size of the databases as compared to the minimal master-mode set size ensures a better approximation of the full velocity field. Figure 6.1 shows the comparison for the spanwise two-point correlations calculated by Hu *et al.* [4] and those obtained from the larger master-mode-set database. Other quantities give at least as good an agreement. Moreover, the increased number of modes in the larger database removed the near-wall discrepancy illustrated by figure 5.18. Overall, the larger database gives quite a reasonable approximation to the full flow.

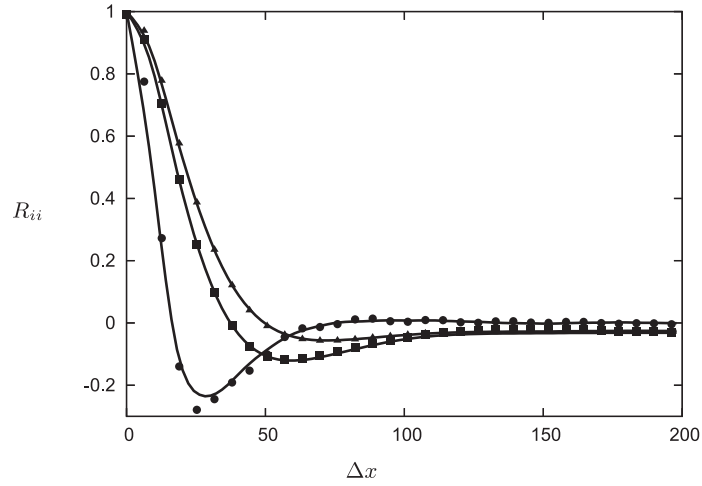


Figure 6.1: Spanwise ($\Delta x = 0$) two-point correlations: curves, full flow as calculated by Hu *et al.* [4], $L_x \times L_y = 12 \times 6$; symbols, master-mode-set database with $N_{mm} = 2170044$ and $L_x \times L_y = 14 \times 9$; longitudinal velocity correlation, R_{uu} , \blacksquare ; spanwise velocity correlation, R_{vv} , \blacktriangle ; wall-normal velocity correlation, R_{ww} , \bullet . For $Re_\tau = 360$ and $z^+ = 10$.

The relatively small size of the master-mode databases allows opening a free on-line access. The databases are currently at <http://www.dnsdata.afm.ses.soton.ac.uk/>. The system allows the user to upload a Fortran 90 code, compile and run it on the server with access to the data through a subroutine library. The user can then download the output of the code. This provides additional savings of the network traffic and appears to be more convenient than downloading the entire database to the remote computer.

6.1 Finding a traveling wave in a DNS solution.

Using a master-mode-set database is most advantageous when an analysis of the same data needs to be repeated many times, as when searching for rare events and repeatedly adjusting the search criterion. Looking for travelling waves in a developed turbulent flow gives an example of such a procedure. Travelling wave solutions attracted recently much attention. For plane channel flow they were found by Itano & Toh [5] and Waleffe [61], while the most recent attempt to find travelling waves in the velocity fields produced by direct numerical simulation was performed by Kerswell & Tutty [62]. Toh and Itano [5] isolated a travelling waves in DNS of channel flow by using a shooting method and showed that the instability of the travelling waves and the succeeding nonlinear evolution correspond to the bursting process. The results of their calculations are shown in figure 6.2. Note that as the Reynolds number and the size of the computational domain increase the likelihood of finding a travelling wave occupying the entire computational domain decreases. Therefore, one has to look for travelling waves in sub-volumes of the domain.

We define u to be a traveling wave solution if it has special form

$$\mathbf{u}(x, y, z, t) = \mathbf{U}(x - ct, y, z) \quad (6.1)$$

for some function \mathbf{U} . In this instance, the solution \mathbf{U} represents a ‘wave’ traveling

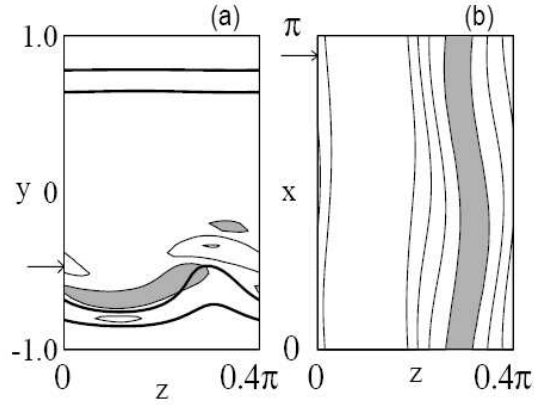


Figure 6.2: Snapshot of travelling waves at $t = 600$ obtained by Itano & Toh [5]. (a) longitudinal vorticity $\omega_x(y, z)$ at $z^+ = 398$; (b) $u_x(x, z)$ at $y^+ = 71$. Shade indicates $u_x < 0.65$ or $\omega_x < -0.05$. Arrows indicate the positions of the section. Thick solid lines are for $u_x = 0.4$ and 0.6 .

to the right with the wave speed c .

Consider the expression

$$f(c) = \sum_{i=1}^3 \left(\frac{\partial u_i}{\partial t} + c \frac{\partial u_i}{\partial x} \right)^2 \quad (6.2)$$

For a travelling wave solution $f(c) = 0$. Our first idea is to inspect various volumes V inside the flow domain and check if there is such a value of c that $f(c) \approx 0$ inside the volume. Then we would declare this volume as occupied by a traveling wave. Note that determining c reduces to minimizing a quadratic functional.

$$\int \int \int_V f(c) = \sum_{i=1}^3 \left(\frac{\partial u_i}{\partial t} + c \frac{\partial u_i}{\partial x} \right)^2 \longrightarrow \min \quad (6.3)$$

Then

$$\frac{df}{dc} = \int \int \int_V \sum_{i=1}^3 \left(\frac{\partial u_i}{\partial t} + c \frac{\partial u_i}{\partial x} \right) \frac{\partial u_i}{\partial x} = 0 \quad (6.4)$$

and therefore

$$c = \frac{- \int \int \int_V \sum_{i=1}^3 \left(\frac{\partial u_i}{\partial t} \frac{\partial u_i}{\partial x} \right)}{\int \int \int_V \sum_{i=1}^3 \left(\frac{\partial u_i}{\partial x} \frac{\partial u_i}{\partial x} \right)} \quad (6.5)$$

Note that unlike the Kerswell & Tutty approach our method does not require a prior knowledge of the travelling wave solution, and our method allows to identify the location of travelling waves occupying only a part of the flow domain, which is necessary for large domains. An attempt to implement this idea showed that $f(c)$ should be suitably normalised, and that a trial-and-error should be used to find the appropriate dimensions of the volumes.

6.2 Results

We performed a search for travelling waves within a master-modes. The database (see Appendix A for more details) contains the time history of the master-mode amplitudes from $t = 0$ to $T = 40$ for the developed turbulent flow at $Re_\tau = 360$ in the domain of the dimensions $L_x \times L_y \times L_z = 6 \times 2 \times 3$. The database contains a time history of the master-mode-set with $N_m = 51508$ modes. The time step size is $\Delta t = 0.0005$.

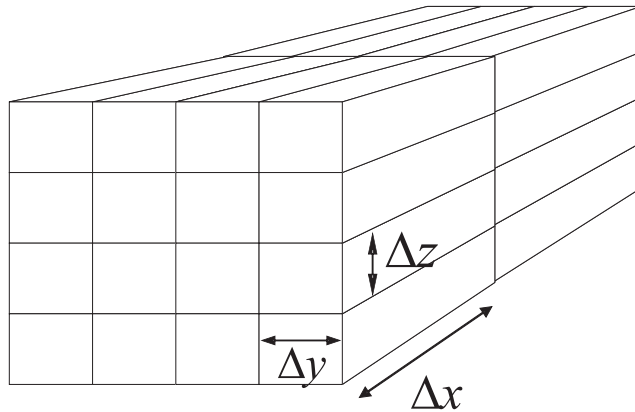


Figure 6.3: Decomposition of the domain.

Case	Δx	Δy	Δz	V	$f_V \text{ min}$	$C_V \text{ min}$	Time
A1	3	0.3	0.2	0.18	0.1154080	14.82364	13.825
A2	1.5	0.15	0.1	0.0225	0.0066326	14.75149	13.750
A3	1.5	0.75	0.5	0.5625	0.1209500	15.27468	10.256

Table 6.1: Run parametters.

We split the calculation domain into volumes as shown in Figure 6.3 and find the minimum f_V of f an each volume. We rewrite (6.5) as:

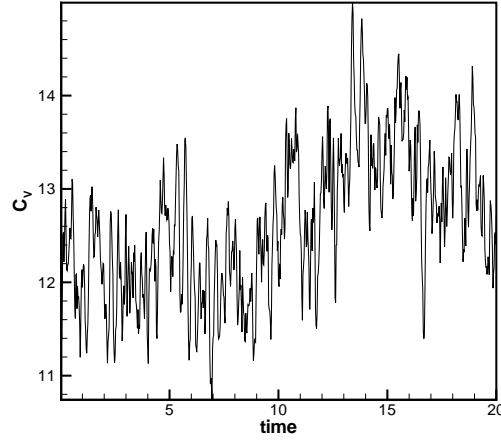
$$C_V(t) = \frac{- \int \int \int_V \sum_{i=1}^3 \left(\frac{\partial u_i}{\partial t} \frac{\partial u_i}{\partial x} \right)}{\int \int \int_V \sum_{i=1}^3 \left(\frac{\partial u_i}{\partial x} \frac{\partial u_i}{\partial x} \right)} \quad (6.6)$$

and a measure of the success as

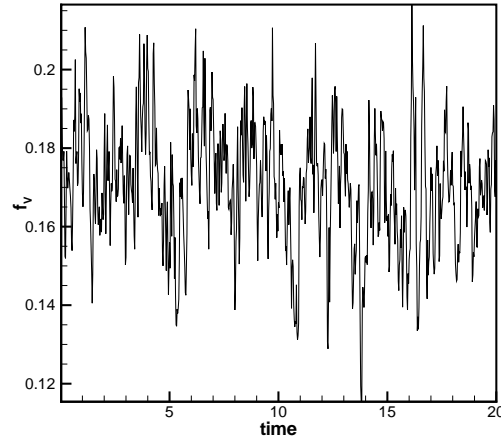
$$f_V(t) = \frac{\int \int \int_V \sum_{i=1}^3 \left(\frac{\partial u_i}{\partial t} + C_V \frac{\partial u_i}{\partial x} \right)^2 dx dy dz}{\frac{1}{V} \int \int \int_V \sum_{i=1}^3 \left(\frac{\partial u_i}{\partial t} \right)^2 dx dy dz} \quad (6.7)$$

The determining C_V reduces to minimizing a quadratic functional f_V . For each rectangular $\Delta x \times \Delta y \times \Delta z$ volumes V we determine the minimum of $f_V(t)$ over $0 \leq t \leq T$ and select the volume for which this minimum ($= f_{V \text{ min}}$) is the smallest. We then vary Δx , Δy and Δz and repeat the procedure, trying to find the largest Δx , Δy and Δz for which $f_{V \text{ min}}$ is small enough to consider the situation as close to a travelling wave. Table 6.1 shows the results for three such trials. Case A2 was then subject of a more close investigation of the flow field in that particular box ($0 \leq x \leq 1.5$; $2.4 \leq y \leq 2.55$; $0 \leq x \leq 0.1$) near that particular time ($t = 13.750$).

In fact in case A1 the minimum was attained at approximately the same time and the minimising volume of case A2 was located approximately in the same place as the minimising volume of case A1. Therefore search cases A1 and A2 gave the



(a)



(b)

Figure 6.4: Time-evolution of C_V (a) , f_V (b) for case A1.

same event. The time evolution of c_V and f_V for the volume V in case A1 is shown in figure 6.4. Figure 6.5 shows the visualisation of the longitudinal velocity at several consecutive times, with the area in question marked by a dashed rectangle. Note that the visual propagation speed in this figure is about 10, which is greater than the mean flow velocity at this distance to the wall (somewhat less than 7) but which is smaller than the velocity $c_v \approx 14.8$ at which the minimum of f was attained (the dashed rectangle moves at velocity c_v in figure 6.5).

Figure 6.6 (a) shows contours of streaks in near-wall turbulence flow at $z^+ = 5.6$

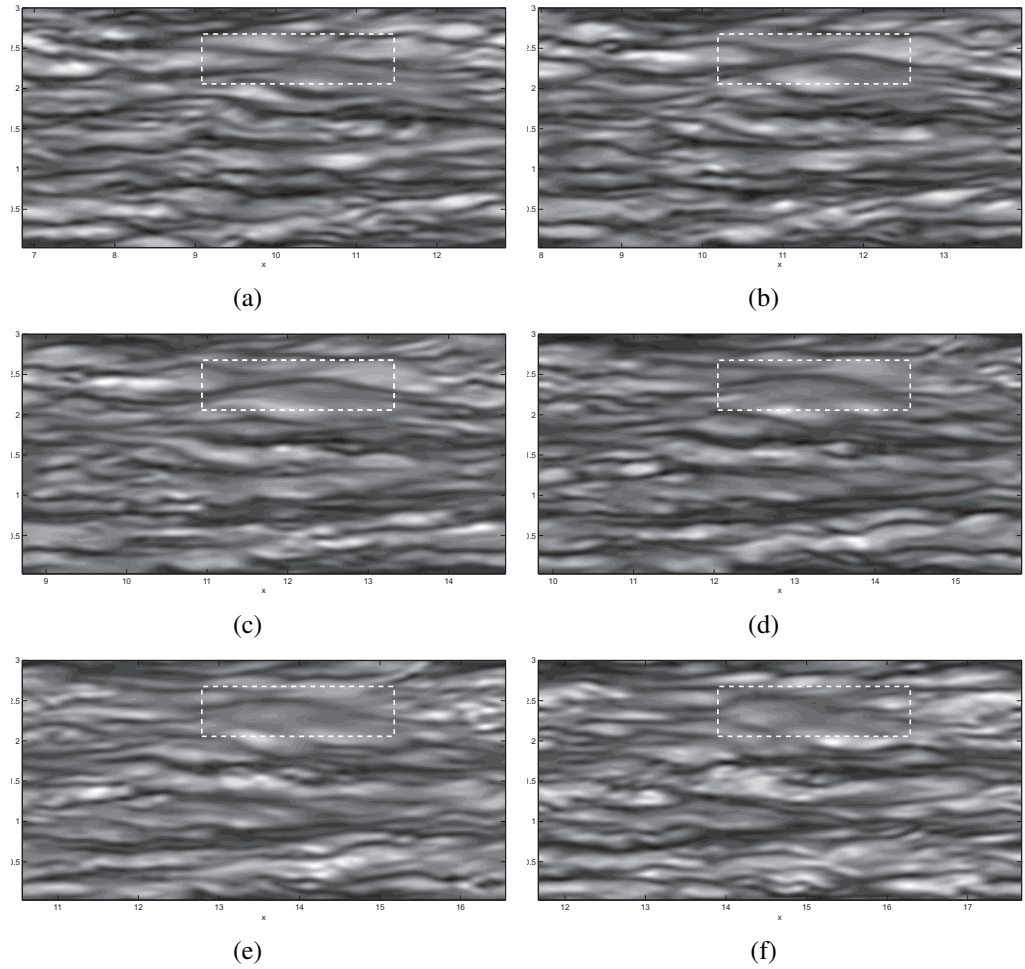


Figure 6.5: Snapshot of TW at a) $t=13.625$, b) $t=13.7$, c) $t=13.75$, d) $t=13.825$, e) $t=13.875$, f) $t=13.95$; Case A1, longitudinal velocity fluctuation in the plane $z^+ = 6.9$ is visualised.

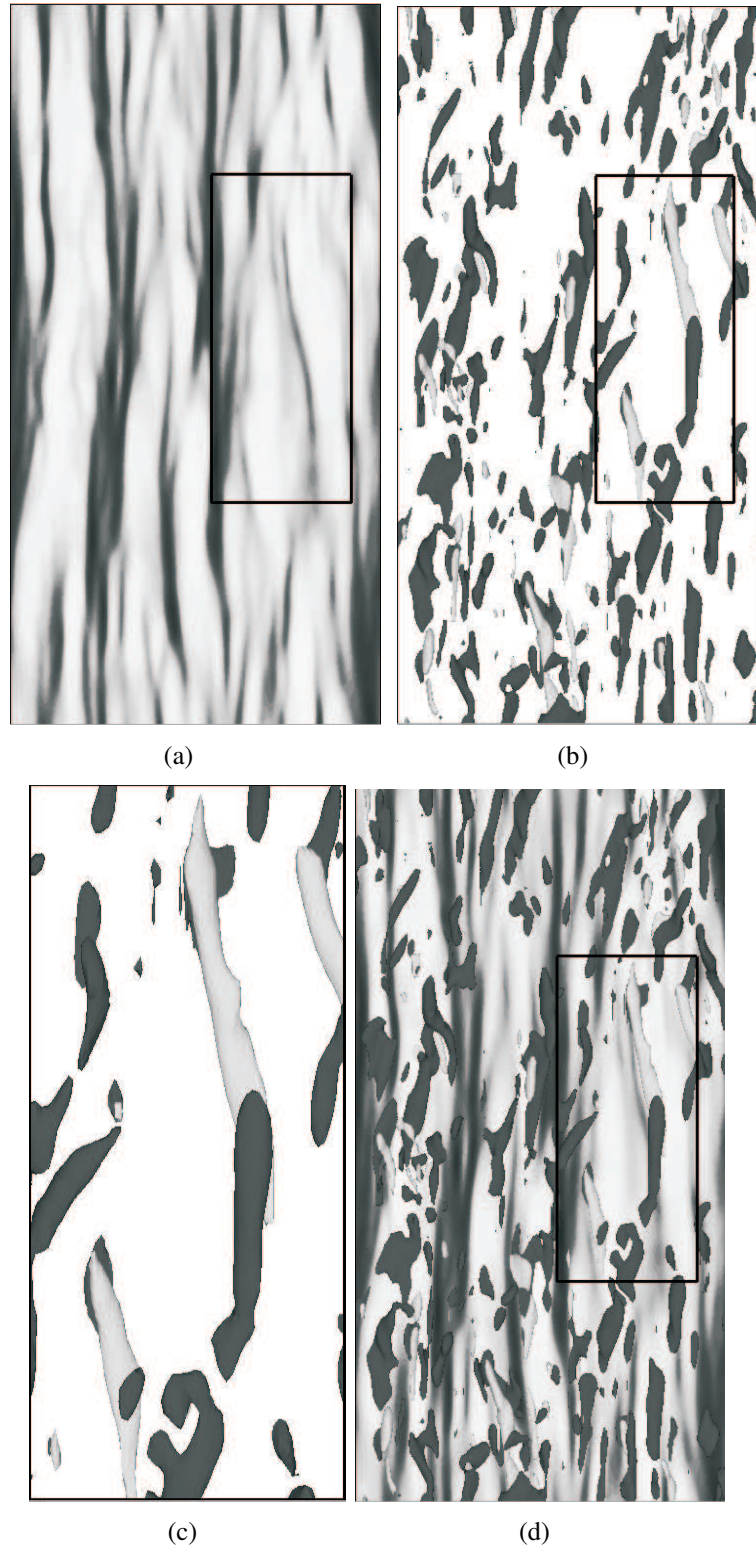


Figure 6.6: Snapshot of TWS and iso-surface of vorticity in the x-direction.

in $x - y$ plane; (b) Iso-surface of vorticity in the x -direction; (d) contours of streaks in near-wall and iso-surface of vorticity and (c) zoom of the place where TW was found)

6.3 Summary

This chapter has described an application of the database of master modes on the example of finding a traveling wave solutions in developed turbulence channel flow. During our numerical calculation we used the flow field from the database without performing new direct calculations. It was shown that a traveling wave-like region exists near the wall. Visual inspection of the vicinity of the minimising volume (see figure 6.5) shows that there indeed exists a structure which remains almost steady in a frame of reference moving with certain velocity, which differs, however, from c_v . It is interesting to note that these velocities expressed in wall units (about 10 and 15) are respectively close to the propagation speed of velocity and vorticity fluctuations and the propagation speed of pressure fluctuations as found by Kim & Hussain [63]. Determining whether the object identified here is in fact related to travelling waves or whether it is a certain combination of generic near-wall structures is outside the scope of the present work. The observations made here confirm the efficiency of the master-mode-set database as a tool for finding rare events in turbulent flow. The easy online access to the database gives an opportunity for any researcher to further investigate the object described in this section.

7 Conclusion.

This investigation was concerned with some longstanding questions about the fundamental structure associated with turbulent flows, particularly with respect to organised structures and finite dimensionality, which appear to be the two most important issues for turbulence control and reduction. Using Chebyshev-Fourier representation of Direct Numerical Simulation solution we determined the so-called master modes, that is those modes which contain all essential information about the flow. We studied the properties of the master-mode set and then used master-modes to explore several questions concerning organised structures.

Thanks to the relatively small size of a master-mode set we built a database containing the time history of the amplitude of master modes of a channel flow, and demonstrated the advantages of having such a database on a problem of searching for traveling waves in turbulent flow.

The major findings from this investigation are as follows:

1. It was shown by numerical experiment that a master mode sets exist in 3D turbulent flows.
2. For turbulent channel flow in a box $L_x \times L_y \times L_z = 6 \times 3 \times 2$ at $Re_\tau = 360$ the minimal size of the master-mode set is about 29716. For box size $L_x \times L_y \times L_z = 14 \times 9 \times 2$ at $Re_\tau = 360$ the size of the master-mode set is about 225900.
3. For channel flow the rate of convergence at which the L_2 norm of the difference between the master solution and the slave solution tends to zero can be estimated as $30(N/V)^{2/3}/Re_\tau$ for large N , where N is the master-mode set size (that is half of the number of independent real-valued parameters needed to identify all the mode amplitudes in the master-mode set), V is the volume of the computational domain, and Re_τ is the Reynolds number based on the friction velocity and the channel half-width.

4. The velocity field corresponding to the minimal master-mode set is a good approximation for mean velocity and some other mean characteristics. However, the minimal master-mode set based on Chebyshev polynomials in the wall-normal direction produces large deviations of turbulence kinetic energy budget components from their exact values in the close vicinity of the wall where Chebyshev polynomials over-resolve the flow. Also, there are significant deviations for some of the two-point correlations. Therefore, it is reasonable to store in a database a master-mode set of a somewhat greater size than minimal.
5. When the flow field is represented as a sum of a master-mode set and the rest of the modes, the near-wall streaks turn out to be contained in the master-mode part. The results for the distribution of the longitudinal vorticity are less certain, with some small-scale structures sometimes observed in the rest of the modes.
6. Two databases containing the time history of the amplitude of master modes of a channel flow, for $Re_\tau = 360$, box size $L_x \times L_y \times L_z = 6 \times 3 \times 2$, time length $T = 40$ and for $Re_\tau = 360$, box size $L_x \times L_y \times L_z = 14 \times 9 \times 2$, time length $T = 15$ were created. For the second case 2200000 master-modes were stored for faster convergence.
7. A database containing the time history of a master-mode set is found to be an efficient tool for investigating rare events. In particular, a travelling-wave-like object was identified on the basis of the analysis of the database.
8. Two master-mode-set databases of the time history of a turbulent channel flow are available online at <http://www.dnsdata.afm.ses.soton.ac.uk/>. The code uploaded by a user can be run on the server with an access to the data.

8 Suggestions for future work

A number of areas closely related to the current work could profitably be exploited:

1. Section 5.3.2 discusses two-point velocity correlations for master/slave-mode sets only and for the full flow. It was noted that near the wall (say at $z^+ = 1.7$) two-point velocity correlation $R_{u_{master}u_{slave}} \approx -1$, $R_{v_{master}v_{slave}} \approx -1$ and $R_{w_{master}w_{slave}} \approx -1$ as well. We represent the solution \mathbf{u} as a sum $\mathbf{u} = \mathbf{u}_m + \mathbf{u}_s$, where $\mathbf{u}_m = \mathbf{u}_m(x; t)$ corresponds to the master-mode set and $\mathbf{u}_s = \mathbf{u}_s(x; t)$ is the remaining part, slave-mode set. Since $R_{u_{master}u_{slave}} \approx -1$ near the wall at $z^+ = 1.7$ this implies that close to the wall master-mode set can be used to reconstruct the slave-mode set by the formula

$$\mathbf{u}_s = -k\mathbf{u}_m \quad (8.1)$$

where k is a constant whose value can be found by regression analysis. Future work should investigate how well the formula (8.1) reproduces the slave-mode set.

2. Another possible area which can be further investigated is to do more exploring of travelling waves in developed turbulence channel flow with the help of master-modes database. We showed in chapter 6 the advantage of the database of master modes on the example of finding travelling wave in developed turbulence channel flow. We showed that travelling wave-like structure exists in a certain region of the flow but studying this structure was outside the scope of the present work.
3. In the future it would be useful to consider some connection with more powerful computer resources (e.g. the Southampton Univeristy Iridis cluster). To

make this possible the current Database Web server would have to run on a Linux operating system, which has an SSH (Secure Shell) protocol.

Appendix A

The DNS Database Web Server and Master-Mode Database User Manual

A Database Web Server provides access to the master-mode and Direct Numerical Simulation (DNS) Database of the AFM Research Group. The web-based service built on this server allows users to manipulate the data with their own code. The user can upload FOTRAN90 code (.f90) to the server, compile and run it on the server with access to the data, and then download the code output.

- **Registration.**

In order to get access to the Database Web Server a user needs to register. There are a few fields which should be filled in (login name, password, email); the rest of the form can be left empty. The process is self-explanatory. The user can login immediately after registration (no authorization is required). See figure A.2.

- **Navigating the site.**

A registered user logged into the web server is presented with a web-page. The page provides access to several options (Home, Login, Profile, Cases, Applications, Web server, Help, Forum, Contact us, Log out). See figure A.3. Option “Cases” gives a direct access to various data files stored in the database, including the data on incompressible turbulent channel flows for different Reynolds numbers. Turbulence statistics and full three-dimensional flowfields are given. Time histories of wall quantity spectra are also provided, as well as master-mode data. With a help of option *Profile* a user can change

her/his information, including the password. Option *Web server* will lead the user to the DNS Database Web Server (see figure A.4). Other options are self-explanatory.

- **Using the web-server.**

After registering on the web server a folder is created for the user and only the user will have access to this folder. Files in a user folder can be downloaded, edited, or deleted. To edit or delete a file the user must first select the file using the tick list and then the *Edit* and *Delete* buttons will be enabled (see figure A.1). During registration some example FORTRAN scripts will be automatically created in the user's folder to demonstrate how to use the system (see also figure A.5).

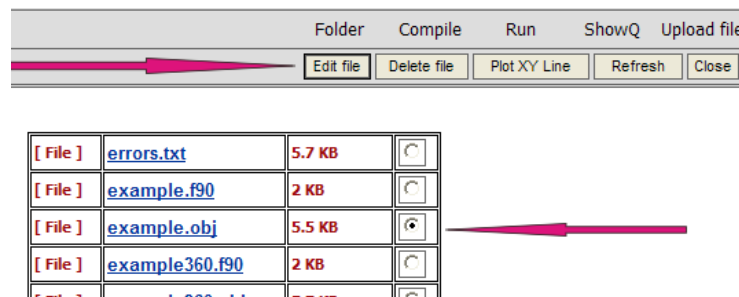


Figure A.1: DNS Database Web Server.

- **Compiling and Running a program.**

To compile the file one has to go to the page *Compile*. A list of compilable files contained in the user's folder will be generated. Choose one and press the button *Compile*. After the compilation the total number of errors will be displayed, also the file "errors.txt" in the user's folder will list the details of the errors. If the program was compiled without errors one can go to the *Run* page and execute the program. If the program runs successfully one will get a message confirming this. All output will go into the user's personal folder. The user code can call library subroutines providing access to the data from the database.

- **Accessing the data.**

By default the example/template fortran files created in the user directory during registration illustrate access to the master-modes data. More detailed description of this access is given in the following section.

The user can generate example/template files for accessing other data using the form at the bottom of the page. For more information about the other (not master-modes) data use the *Contact us* link.

- **Master-mode database.**

The parameters of the flow in a plane channel are non-dimensionalized with the channel half-width h^* and the friction velocity $u_\tau^* = \sqrt{\tau_w^*/\rho^*}$, where τ_w^* is the wall shear stress and ρ^* is the density. Here asterisks are used to denote dimensional quantities. The Reynolds number is $Re_\tau = u_\tau^* h^* / \nu^*$. The non-dimensional quantities are then defined as $\mathbf{u} = \mathbf{u}^* / u_\tau^*$, $\mathbf{x} = \mathbf{x}^* / h^*$, $p = p^* / \rho^* u_\tau^{*2}$, $t = t^* u_\tau^* / h^*$.

The normalised mean pressure gradient is $dP/dx = -1$. The database contains the master-mode set of the solution of the following problem

$$\nabla \cdot \mathbf{u} = 0,$$

$$\frac{\partial \mathbf{u}}{\partial t} + \mathbf{u} \cdot \nabla \mathbf{u} = -\nabla p - \mathbf{e}_x \frac{dP}{dx} + \frac{1}{Re_\tau} \nabla^2 \mathbf{u},$$

where \mathbf{e}_x is the unit vector of the x -axis. The coordinates are set as x in the streamwise direction, y in the spanwise direction and z in the wall-normal direction, with the channel walls at $z = \pm 1$. No-slip boundary condition is imposed on the walls. Periodicity conditions are used in the directions parallel to the walls: $\mathbf{u}(x + L_x, y, z, t) = \mathbf{u}(x, y, z, t)$, $p(x + L_x, y, z, t) = p(x, y, z, t)$, $\mathbf{u}(x, y + L_y, z, t) = \mathbf{u}(x, y, z, t)$, and $p(x, y, z, t) = p(x, y + L_y, z, t)$, where L_x and L_y are the periods equal to the dimensions of the computation domain.

In this database velocity is stored as a set of values $\hat{\mathbf{u}}_{k_x, k_y, k_z}(t_m)$ so that the velocity is given by the formula

$$\mathbf{u}_m(x, t) = \sum_{k_x, k_y, k_z \in M} \hat{\mathbf{u}}_{k_x, k_y, k_z}(t) e^{2\pi i(k_x x/L_x + k_y y/L_y)} T_{k_z}(z),$$

where $T_{k_z}(z)$ is a Chebyshev polynomial (see <http://mathworld.wolfram.com/>).

Set $M = \{(k_{x,j}, k_{y,j}, k_{z,j})\}_{j=1}^N$ is a master-mode set of a channel flow for $Re_\tau = 360$. A draft of a part of a paper describing master-modes in more detail is available at <http://www.dnsdata.afm.ses.soton.ac.uk/paper.pdf>. The computational box size is $L_x = 6$, $L_y = 3$, $L_z = 2$. The numbers of discretization points are, respectively $N_x = 128$, $N_y = 128$, $N_z = 160$ and the time duration $T = 40$. The database contains velocity fields u, v and w as a function of time $t = t_m$, coordinates $x = x_i$, $y = y_j$ and $z = z_k$ where

$$t_m = (m - 1) \cdot \Delta t = (m - 1) \cdot 0.0005,$$

$$x_i = \frac{L_x \cdot i}{N_x}, \quad y_j = \frac{L_y \cdot j}{N_y}, \quad z_k = \cos\left(\frac{\pi \cdot k}{N_z}\right)$$

where

$$m = 1, \dots, 80000, \quad i = 1, \dots, N_x, \quad j = 1, \dots, N_y, \quad k = 1, \dots, N_z$$

For the code to have access to the master-mode database it should include the line “use master_modes_dll” at the top of the script (figure A.6 line 30). The code can then call the subroutine **G_UVW(m,u,v,w)**. Here, m is an integer corresponding to the time step ($t_m = (m - 1) * \Delta t$). Parameters u,v,w have an array size of $N_x \times N_y \times N_z$. After calling the subroutine **G_UVW** the velocity fields u,v,w will be available as $u(i, j, k) = u(x_i, y_j, z_k)$.

By default an example file is created in your personal folder called ‘example.f90’ (figure A.6). The program calls **G_UVW** to find the velocity field and calculates the mean velocity profile of the channel flow data. After the calculation the mean velocity data will be in the file ‘stats.dat’ in the user personal folder. The data can be downloaded to your computer. One can also use the online ‘PlotXY Line’ facility for quick visual inspection of the results.

The image shows a screenshot of a web browser window titled "DNS - Windows Internet Explorer". The address bar displays the URL "http://www.dnsdata.afm.ses.soton.ac.uk/reg.php". The browser has two tabs: "DNS" and "Microsoft Outlook Web Access". The website header includes a navigation menu with links: Home, Login, Cases, Applications, Web server, Help, Contact us, and Log out. The main content area is titled "Registration" and contains a form with the following fields:

- *Login (with a note: "Username must be between 4-16 characters (letters and numbers)")
- *Password (with a note: "Password must be between 4-16 characters (letters and numbers)")
- *Re-enter password:
- *Email
- First name
- Surname
- University
- Country
- Address
- Fax
- Tel
- Site URL

Below the form fields, there is a section labeled "Mandatory fields" with a CAPTCHA image. The CAPTCHA text is "Type the characters you see in the picture below". The CAPTCHA image shows a grid of characters: 4, 3, 9, 0. At the bottom of the form are "Submit" and "Reset" buttons.

Figure A.2: Registration form.



Figure A.3: Navigating the site.

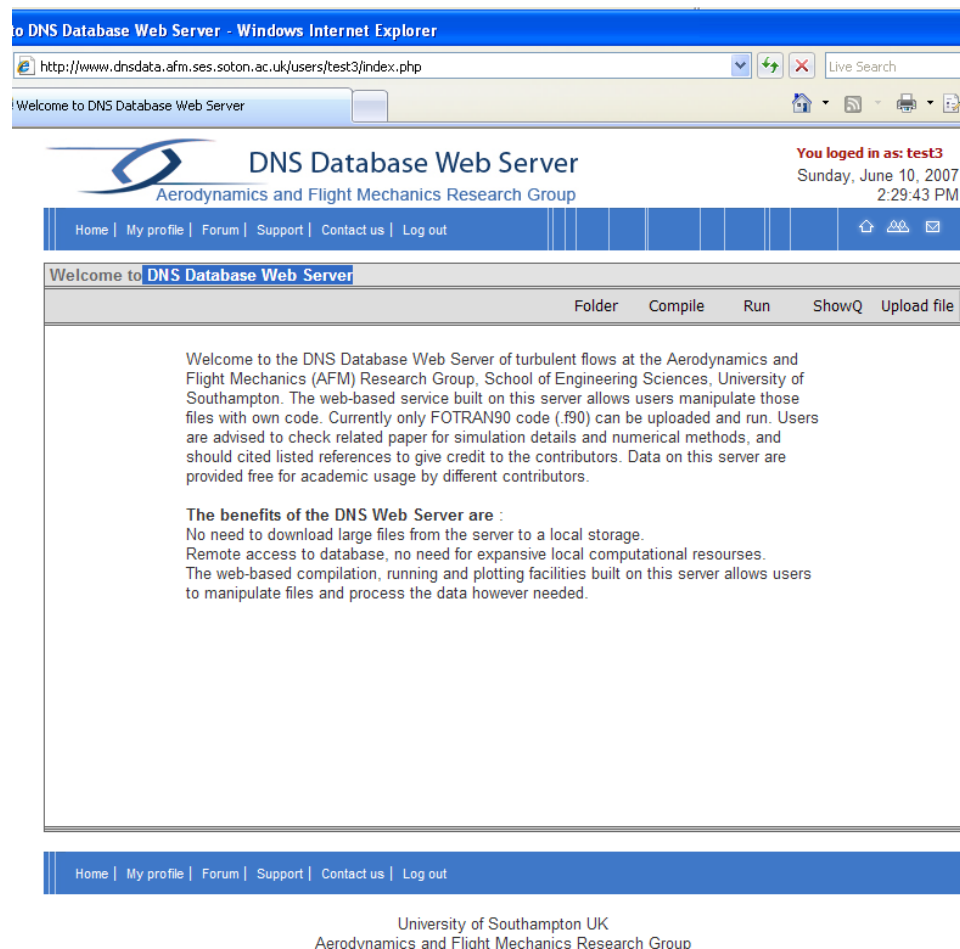



Figure A.4: DNS Database Web Server.


DNS Database Web Server
 Aerodynamics and Flight Mechanics Research Group












You logged in as: **test3**
 Sunday, June 10, 2007
 2:42:19 PM

[Home](#) | [My profile](#) | [Forum](#) | [Support](#) | [Contact us](#) | [Log out](#)

Folder

[Folder](#) [Compile](#) [Run](#) [ShowQ](#) [Upload file](#)

[Edit file](#) [Delete file](#) [Plot XY Line](#) [Refresh](#) [Close](#)

[File]	errors.txt	5.7 KB	
[File]	example.f90	2 KB	
[File]	example.obj	5.5 KB	
[File]	example360.f90	2 KB	
[File]	example360.obj	5.7 KB	
[File]	hello_world.f90	80 bytes	
[File]	output.txt	740 bytes	
[File]	pdf.bmp	879.8 KB	
[File]	pdf.dat	9.7 KB	
[File]	stats.bmp	879.8 KB	
[File]	stats.dat	9.7 KB	

[Home](#) | [My profile](#) | [Forum](#) | [Support](#) | [Contact us](#) | [Log out](#)

Figure A.5: DNS Database Web Server.

```

1 !*****
2 ! example.f90 - test program calculating the mean velocity profile
3 ! of the incompressible channel flow for Reynolds number 360.
4 !
5 ! The coordinates are set as x in the streamwise direction, y in
6 ! the spanwise direction and z in the wall-normal direction.
7 !
8 ! The domain is Lx=6,Ly=3,Lz=2. The number of discretization point
9 ! are Nx=128, Ny=128 and Nz=160.
10 !
11 ! Input parameters :
12 !
13 !     nx, ny ,nz : number of grid points in x,y and z directions (integer)
14 !     m           : number corresponds to the time step tm=(m-1)* dt (integer)
15 !
16 !     Subroutine G_UVW(m,u,v,w) allows user to have access to the
17 !     master-mode database.
18 !
19 ! Output parameters of G_UVW :
20 !
21 !     u(nx,ny,nz) : the streamwise velocity at T=Tm, X=Xi,Y=Yj,Z=Zk
22 !     v(nx,ny,nz) : the spanwise velocity at T=Tm, X=Xi,Y=Yj,Z=Zk
23 !     w(nx,ny,nz) : the wall-normal velocity at T=Tm, X=Xi,Y=Yj,Z=Zk
24 !
25 !*****
26 program example
27 use master_modes_dll
28 parameter(nx=128,ny=128,nz=160)
29 real, dimension(nx,ny,nz) :: u,v,w
30 real :: uu
31 real, dimension(nz,3) :: usum
32 real :: x(nx+2),y(ny),z(nz+2), pi
33 integer :: m
34
35
36 x1=6.
37 y1=3.
38 pi=2.*acos(0.)
39
40 !Coordinates of the grid points
41 do i=1, nx+1
42   x(i)=x1*real(i-1)/real(nx)
43 end do
44 do i=1, ny
45   y(i)=y1*real(i-1)/real(ny)
46 end do
47 do i=1, nz+1
48   z(i)=cos(pi*real(i-1)/real(nz))
49 end do
50
51 !Example of calculating u(x,y,z) at T=Tm=0.0005, x=4.5, y=1.5, z=0.7
52 m=2
53 call G_UVW(m,u,v,w) ! Getting velocity file for t=(m-1)*dt=(m-1)*0.0005
54
55 uu=u(97,65,41)
56
57 ! Calculating the mean velocity profile
58 do k=1,nz
59   do j=1,ny
60     do i=1, nx
61       usum(k,1)=usum(k,1)+u(i,j,k)/real(nx*ny)
62     end do
63   end do
64 end do
65
66
67 ! Writing the profile to a file
68 open(1,file='stats.dat',status='unknown', form='formatted')
69
70 do k=1,nz
71   write(1,*) z(k), usum(k,1)
72 end do
73 close(1)
74
75 end program example

```

Figure A.6: Example.

Bibliography

- [1] E. Olson and E.S. Titi. Determining modes for continuous data assimilation in 2D turbulence. *Journal of Statistical Physics*, 113:799–840, 2003.
- [2] W.D. Henshaw, H.O. Kreiss, and J. Ystroom. Numerical experiments on the interaction between the large and small-scale motions of the Navier-Stokes equations. *Society for Industrial and Applied Mathematics*, 1:119–149, 2003.
- [3] K. Yoshida, J. Yamaguchi, and Y. Kaneda. Regeneration of Small Eddies by Data Assimilation in Turbulence. *Phys. Rev. Lett.* 94 (1) 014501, 2005.
- [4] Z. W. Hu and N. D. Sandham. Dns database for turbulent couette and poiseuille flow. *Technical Report:AFM-01/04 Southampton University*, 2001.
- [5] T. Itano and S. Toh. The dynamics of bursting process in wall turbulence. *Journal of the Physical Society of Japan*, 70:703–716, 2001.
- [6] N.D. Sandham and R.J.A. Howard. Direct simulation of turbulence using massively parallel computers. In D.R. Emerson, A. Ecer, J. Periaux, N. Satofuka, and P. Fox, editors. *Parallel Computational Fluid Dynamics. North-Holland*, 1998.
- [7] L. Keefe, J. Kim, and P. Moin. The dimension of the attractors underlying periodic turbulent Poiseuille flow. *J. Fluid Mech.*, 242:1–29, 1992.
- [8] M.T. Landahl and E. Mollo-Christensen. *Turbulence and Random Process in Fluid Mechanics*. Cambridge University Press, second edition, 1992.
- [9] S. Hoyas and J. Jiménez. Scaling of the velocity fluctuations in turbulent channels up to $Re_\tau = 2003$. *Phys. of Fluids*. 18 (011702), 2006.

- [10] A.N. Kolmogorov. The local structure of turbulence in incompressible viscous fluid for very large reynolds numbers. *C.R. (Doklady) Acad. Sci. URSS*, 30:301–305, 1941.
- [11] C. Foias and G. Prodi. Sur le comportement global des solutions non-stationnaires des èquations de Navier-Stokes en dimension 2. *Re nd. Sem. Mat. Univ. Padova*, 39, 1967.
- [12] R. Rosa C. Foias, O. Manley and R. Temam. Navier-stokes equations and turbulence. *Cambridge University Press*, 2001.
- [13] C. Foias and R. Temam. Some analytic and geometric properties of the solutions of the evolution Navier-Stokes equations. *J. Math. Pures et Appl*, 58:334–268, 1979.
- [14] O. Manley P. Constantin, C. Foias and R. Temam. Attractors representing turbulent flows. *Memoirs of AMS*, 53:314, 1982.
- [15] R.H. Kraichnan. Inertial ranges in two-dimensional turbulence. *Phys. Fluids*, 10:1417–1423, 1967.
- [16] O. Ladyzhenskaya. On the dynamical system generated by the Navier-Stokes equations. *J. of Soviet Math*, 3:27–91, 1975.
- [17] P. Constantin and C. Foias. Global Lyapunov exponents, Kaplan-Yorke formulas and the dimension of the attractor for the 2D Navier-Stokes equations. *Comm. Pure Appl. Math*, page 27, 1985.
- [18] O. Manley P. Constantin, C. Foias and R. Temam. Determining modes and fractal dimension of turbulent flows. *J. Fluid Mech*, 440:150–427, 1985.
- [19] R. Temam. Infinite dimensional dynamical systems in mechanics and physics. *J. Applied Mathematical Sciences*, 68:517, 1988.

- [20] C. Foias and R. Temam. Determination of the solutions of the navier-stokes equations by a set of nodal values. *Math. Comput*, 43:117–113, 1984.
- [21] C. Foias, O. Manley, R. Temam, and Y. M. Treve. Asymptotic analysis of the Navier-Stokes equations. *J. Physics D*, 9:157–188, 1983.
- [22] C. Foias and E.S. Titi. Determining nodes, finite difference schemes and inertial manifolds, Nonlinearity. *J. Physics*, 4:135–153, 1991.
- [23] D.A. Jones and E.S. Titi. On the number of determining nodes for the 2D Navier-Stokes equations. *J. Physics D*, 60:72–88, 1992.
- [24] D.A. Jones and E.S. Titi. Upper bounds on the number of determining modes, nodes, and volume elements for the Navier-Stokes equations. *Indiana Univ. Math*, 42:1–12, 1993.
- [25] P. Collet, J.P. Eckmann, H. Epstein, and J. Stubbe. A global attracting set for the kuramotosivashinsky equation. *J. Math. Phys*, 152:203–214, 1993.
- [26] P.K. Friz and J. C. Robinson. Parametrising the attractor of the two-dimensional Navier-Stokes equations with a finite number of nodal values. *J. Physics D*, 148:201–220, 2001.
- [27] J. Charney, M. Halem, and R. Jastrow. Use of incomplete historical data to infer the present state of the atmosphere. *J. Atmos. Sci*, 26:1160–1163, 1969.
- [28] S. Yang and W. R. Cotton. A method of continuous Data Assimilation using shortrange 4D-Var Analysis. *Department of Atmospheric Science, Colorado State University, Technical Report - paper No. 653, Fort Collins (CO), USA*, 1998.
- [29] M. Ghil and P. Malanotte-Rizzoli. Data Assimilation in meteorolgy and oceanography. *Adv. Geophys*, 33:141–266, 1991.

- [30] P. Courtier, E. Andersson, W. Heckley, J. Pailleux, D. Vasiljevic, M. Hamrud, A. Hollingsworth, F. Rabier, and M. Fisher. The ECMWF implementation of three-dimensional variational assimilation (3d-var) i: Formulation. *Quarterly Journal of the Royal Meteorological Society*, 124:1783–1808, 1998.
- [31] A. Lorenc, S. Ballard, R. Bell, N. Ingleby, P. Andrews, D. Barker, J. Bray, A. Clayton, T. Dalby, D. Li, T. Payne, and F. Saunders. The Met Office Global 3-Dimensional Variational Data Assimilation. *Quarterly Journal of the Royal Meteorological Society*, 126:2991–3012, 2000.
- [32] T. Peacock, J. Hertzberg, Y.C. Lee, and E. Bradley. Forcing a planar jet flow using MEMS. *Experiments in Fluids*, 37:22–28, 2004.
- [33] G. Browning, W.D. Henshaw, and H.O. Kreiss. A numerical investigation of the interaction between the large and small scales of the two-dimensional incompressible Navier-Stokes equations. *Research report LA-UR-98-1712, Los Alamos National Laboratory, Los Alamos*, 1998.
- [34] E. Olson and E. S. Titi. Determining modes and Grashof number in 2D turbulence - A numerical case study. *Internal report, Department of Mathematics, University of Nevada*, 2006.
- [35] P. Constantin and C. Foias. Navier-Stokes equation. *University of Chicago Press*, 1988.
- [36] R. Grappin and J. L  orat. Lyapunov Exponents and the Dimension of Periodic Incompressible Navier-Stokes Flows. *J. Fluid Mech*, 222:61–94, 1991.
- [37] A. K. Kolmogorov. *Dokl. Akad. Nauk SSSR*, 30:301, 1941.
- [38] L. Landau and E. Lifschitz. *Fluid mechanics*. Pergamon Press, Oxford, UK, 1987.

- [39] R. Temam. Approximation of Attractors, Large Eddy Simulations and Multiscale Methods. *Mathematical and Physical Sciences*, 434, No. 1890:23–39, 1991.
- [40] O.A. Ladyzenskaya. The dynamical system that is generated by the navier-stokes equations. *Za p. Nauchn. Sem. Leningrad. Otdel. Mat. Inst. Steklov.*, 27:91–115, 1972.
- [41] C. Foias and R. Temam. *The connection between the Navier-Stokes equations, dynamical systems, and turbulence theory*, in Directions in Partial Differential Equations. Ed. Michael G. Crandall, Paul H. Rabinowitz, Robert E. L. Turner. Publication 54, Mathematical Research Center, University of Wisconsin - Madison. Boston, MA: Academic Press, 1987. 55-73.
- [42] G. Sell. Global attractors for the three-dimensional navier-stokes equation. *Journal of Dynamics and Differential Equations*, 8:1–33, 1996.
- [43] B. Cockburn, D.A. Jones, and E.S. Titi. Estimating the number of asymptotic degrees of freedom for nonlinear dissipative systems. *Mathematics of Computation*, 66:1073–1087, 1997.
- [44] H. Kreiss and J. Oliger. Comparison of accurate methods for the integration of hyperbolic equations. *Tellus*, XXIV:199–215, 1972.
- [45] S. A. Orszag. Comparison of pseudospectral and spectral approximations. *tud. Appl. Math.*, 51:253–259, 1972.
- [46] J. W. Cooley and J. W. Tukey. An algorithm for the machine calculation of complex fourier series. *Mathematics of Computation*, 19:297–301, 1965.
- [47] P. R. Spalart and A. Leonard. Direct numerical simulation of equilibrium turbulent boundary layers. *Springer Verlag*, In Turbulent Shear Flows 5:253–259, 1987.

- [48] P. R. Spalart and J. H. Watmuff. Experimental and numerical study of a turbulent boundary layer with pressure gradients. *J. Fluid Mech.*, 249:337–371, 1993.
- [49] R.D Moser, J. Kim, and N. N. Mansour. DNS of turbulent channel flow up to $Re_\tau = 590$. *Physics of Fluids*, 11:943–945, 1999.
- [50] O. Schmidtman, F. Feudel, and N. Seehafer. Nonlinear Galerkin methods for the 3D magnetohydrodynamic equations. *Int. J. Bif. and Chaos*, 7:1497–1507, 1997.
- [51] O. Schmidtman, F. Feudel, and N. Seehafer. Nonlinear Galerkin methods based on the concept of determining modes for the magnetohydrodynamic equations. *J. Phys. A*, 31:7141–7155, 1998.
- [52] S. J. Kline, W. C. Reynolds, F. A. Schraub, and P. W. Rundstadler. The structure of turbulent boundary layers. *J. Fluid. Mech*, 30:741, 1967.
- [53] E. R. Corino and R. S. Brodkey. A visual study of turbulent shear flow. *J. Fluid. Mech*, 61:513–540, 1973.
- [54] H. T. Kim, S. J. Kline, and W. C. Reynolds. The production of turbulence near a smooth wall in a turbulent boundary layer. *J. Fluid. Mech*, 50:133–160, 1971.
- [55] P. S. Jang, D. J. Benney, and R. L. Gran. On the origin of streamwise vortices in a turbulent boundary layer. *J. Fluid. Mech*, 169:109–123, 1986.
- [56] K. R. Sreenivasan. A unified view of the origin and morphology of the turbulent boundary layer structure. In *Proc. IUTAM Symp. on Turbulence Management and Relaminarisation* (ed. H. W. Liepmann and R. Narasimha), pages 37–67, 1988.

- [57] F. Waleffe, J. Kim, and J. Hamilton. On the origin of streaks in turbulent boundary layers. In *Turbulent Shear Flows 8*. ed. F. Durst, R. Friedrich, B. E. Launder, F. W. Schmidt, U. Schumann and J. Whitelaw, Springer-Verlag, Berlin, pages 37-49, 1993.
- [58] K. M. Butler and B. F. Farrell. Optimal perturbations and streak spacing in wall-bounded turbulent shear flows. *Phys. of Fluids*, A5:774–777, 1993.
- [59] J. Jimenez and P. Orlandi. The roll-up of a vortex layer near a wall. *J. Fluid Mech.*, 248:297, 1993.
- [60] Kim J. *Control of turbulent boundary layers*. Advances in Turbulence IX. Proceedings of the Ninth European Turbulence Conference, July 2-5, 2002, Southampton (ed. I. P. Castro, P. E. Hancock & T. G. Thomas), pp. 69-70. Barselona: CIMNE.
- [61] A. S. Philip and F. Waleffe. Polymer drag reduction in exact coherent structures of plane shear flow. *Physics of Fluids*, 16:3470–3482, 2004.
- [62] R. R. Kerswell and O.R. Tutty. Recurrence of travelling waves in transitional pipe flow. *J. Fluid Mech*, 584:69–102, 2007.
- [63] J. Kim and F. Hussain. Probagation velocity of perturbations in turbulent channel flow. *Phys. of Fluids.*, A 5 (3):695–706, 1993.